Label-free plasmonic biosensors for real-time live cell analysis

Thèse N° 9594

Xiaokang LI

2019

ÉCOLE POLYTECHNIQUE
FÉDÉRALE DE LAUSANNE

致爱我的家人和刹那韶华

Acknowledgements

and Daniel, are very easygoing and friendly. Whenever I had questions regarding basic plasmonics theories, they would always explain to me patiently and clearly. I joined the lab together with Cenk, who was then a master student. We have worked together closely for my first project, and he has always been supportive of the fabrication aspects for my experiments. I conducted most of my research with Maria, a sunny Spanish woman. She has given me lots of practical knowledge regarding biosensors and excellent opinions on my writing skills. We also attended many conferences together, in Switzerland, in and outside Europe, all of which unforgettable memories. Dordaneh has been a very close and loyal friend since we moved to the same office. We shared opinions (criticized) on each other's study, exchanged ideas on daily life, and explored new places in the city and beyond.

Later, new members joined the team and I'm grateful to them for keeping my adventure going. I will remember all the happy moments I had with Aleksandrs, Aurélian, Beini, Deepthy, Jihye, Kosmas, Li, Natsuki, Samuel, Yen-Cheng, and many more. I thank all the technical assistance from Alexander, Eduardo and Yasaman, as well as the helpful discussions with them. I also appreciate the wonderful explorations outside my professional life with my 'gang' in Lausanne: Allan, Bin, Donghe, Jing, Min, Ruofan, Ruojun, Wuzhou, Xiaoxue, Yixing, and many others.

My special thanks to Patrick for his valuable support and assistance in my study, for his priceless advice on my thesis, and especially all his kindness, patience and understanding.

Last but not least, my wholehearted appreciation to my parents and my grandma for their unconditional love and support. They have always encouraged me to pursue my passion for science and my curiosity of exploring the world. 爸爸妈妈和姥姥，谢谢你们！

Lausanne, 15 July 2019   Xiaokang Li / 李晓康

Abstract

For decades, the understanding of life has been focused on its most fundamental building blocks: molecules. Deciphering the dynamic activities of protein molecules in human cells is of vital significance for fundamental and clinical studies. The minuscule scale of protein molecules poses a great challenge for precise quantification. Labeling the molecules of interest with fluorescent and enzymatic tags has thus become an effective strategy to indicate their existence. However, the addition of extrinsic fluorescent tags has shown a number of evident side effects interfering with protein functions and cell biology. The extra steps caused by molecular labeling also increase the complexity of the entire assay and decrease the temporal resolution of the measurement from hours to days. These drawbacks of traditional strategies inevitably hinder the real-time monitoring of cellular activities with minimum interval or external interference.

This doctoral thesis focuses on the engineering and demonstration of novel label-free biosensing platforms for real-time cell studies: (1) the secretion of protein molecules from live cells, and (2) the characterization of cellular interactions.

For the first topic, a biosensor using plasmonic nanohole arrays as the core sensing elements has been designed. These nanohole arrays consist of a thin gold film perforated with periodic nanoholes. They enable extraordinary optical transmission (EOT), an optical phenomenon that has shown promising capabilities for biochemical detection. This thesis demonstrates, for the first time the application of these structures for real-time monitoring of protein secretions from live cells. On the one hand, the secretion of VEGF (a type of growth factor) from live cancer cells has been monitored in real-time at the temporal resolution of seconds without any additional sample treatment. On the other hand, the integration with the advanced microfluidic

system has enabled the biosensor to measure secretion events at the single-cell level by solving a number of technical issues (e.g., low analyte abundance, liquid evaporation). In particular, the real-time production of IL-2 (a cytokine) from single lymphoma cells were monitored for hours, which shows the exceptional versatility of this optofluidic nanobiosensor.

For the second topic, a multiparametric surface plasmon resonance (SPR) biosensor has been exploited to investigate interactions between T-cell receptors (TCR) and peptide-major histocompatibility complexes (pMHC). This type of interaction plays a central role in T cell-mediated immunity. Notably, intact human T cells – rather than purified recombinant TCR proteins – were directly used as analytes. A biomimicking lipid membrane was created on the sensor surface to present pMHC molecules, enabling the capture of T cells *in vitro*. Therefore, the affinity (e.g., binding kinetics) between different types of T cells and membrane-bound pMHC molecules can be readily measured in a label-free manner.

The results presented in this thesis rely on a wide range of engineering technologies (imaging, microfluidics, and micro-/nano-manufacturing) and knowledge of biology, chemistry, and optics. The proposed methods using label-free plasmonic biosensors represent a promising strategy to overcome the challenges related to current biochemical analyses. We anticipate that plasmonic biosensors will boost new biodetection methodologies for biomedical research.

Keywords: label-free biosensor, nanoplasmonics, nanohole arrays, surface plasmon resonance, live cell analysis, single-cell analysis, cell secretion, lipid membrane, TCR affinity analysis

Version abrégée

Durant des décennies, la compréhension de la vie s'est appuyée sur ses composants les plus élémentaires: les molécules. L'étude des activités dynamiques des protéines dans les cellules humaines est d'une importance capitale pour la recherche fondamentale et clinique. La taille minuscule des protéines présente un grand défi pour leur quantification. Une stratégie efficace pour visualiser leur existence est donc de marquer les molécules étudiées avec des sondes fluorescentes ou des enzymes. Cependant, l'ajout de marqueurs fluorescents a mis en évidence des effets secondaires interférant avec les fonctions des protéines et la biologie cellulaire. En outre, cette étape supplémentaire de marquage complique l'analyse et fait passer la résolution temporelle d'heures en jours. Ces inconvénients des techniques traditionnelles empêchent ainsi le suivi en temps réel des activités cellulaires qui minimise à la fois l'échelle de temps et les interférences externes.

Ce travail de doctorat s'intéresse à la conception et à la démonstration de nouvelles plateformes de biodétection pour des études des cellules en temps réel : (1) la sécrétion des protéines par des cellules vivantes, et (2) la caractérisation d'interactions cellulaires.

Pour le premier sujet, nous avons conçu un biocapteur utilisant comme élément central de détection des réseaux plasmoniques de nanotrous. Ces réseaux sont composés d'un mince film en or percé régulièrement de nanotrous. Ils permettent la transmission optique extraordinaire (EOT), un phénomène optique qui a montré un potentiel prometteur pour la détection biochimique. Cette thèse démontre pour la première fois l'application de ses structures pour le suivi en temps réel de la sécrétion de protéines par des cellules vivantes. D'une part, la sécrétion de VEGF (un type de facteur de croissance) par des cellules cancéreuses vivantes été suivie en temps réel avec une résolution temporelle de l'ordre de la seconde, ceci sans traitement

supplémentaire de l'échantillon. D'autre part, l'introduction d'un système microfluidique avancé a permis au biocapteur de mesurer la sécrétion à l'échelle de la cellule individuelle en résolvant certaines difficultés techniques (par exemple la faible concentration d'analytes et l'évaporation). En particulier, la production en temps réel d'IL-2 (une cytokine) de cellules individuelles de lymphome a été mesurée durant plusieurs heures, démontrant l'excellente polyvalence de ce nanobiocapteur.

Pour le second sujet, un biocapteur multiparamétrique à résonance plasmon de surface (SPR) a été utilisé pour examiner les interactions entre les récepteurs des cellules T (TCR) et les complexes majeurs d'histocompatibilité peptide (pMHC). Ce type d'interaction joue un rôle clé dans l'immunité par les cellules T. Remarquablement, nous avons utilisé comme analytes des cellules T humaines intactes plutôt que des protéines TCR purifiées recombinantes. Une membrane lipide biomimétique a été créée sur la surface du capteur pour présenter les molécules pMHC, permettant de capturer les cellules T in vitro. Il devient ainsi aisé de mesurer sans marquage l'affinité (par exemple, cinétique de liaison) entre différents types de cellules T et des molécules pMHC liées à la membrane.

Les résultats présentés dans cette thèse se basent sur une large gamme de technologies de l'ingénieur (imagerie, microfluidique et micro-/nanofabrication) et sur la connaissance de la biologie, de la chimie et de l'optique. Les méthodes proposées, utilisant des biocapteurs plasmoniques sans marquage, constituent une stratégie prometteuse pour surmonter les difficultés rencontrées dans les analyses biochimiques actuelles. Nous prévoyons que les biocapteurs plasmoniques vont encourager de nouvelles méthodologies de biodétection pour la recherche biomédicale.

Mots clés: biocapteur sans marquage, nanoplasmonique, réseaux de nanotrous, résonance plasmons de surface, analyse de cellules vivantes, analyse de cellules individuelles, sécrétion cellulaire, membrane lipide, analyse d'affinité de TCR

Table of Contents

Introduction

Motivation of this thesis

Successful medical practices and novel therapies advance with the progression of fundamental life sciences. The development of efficient strategies to tackle diseases relies on the understanding of how human cells function. For example, cancer cells constantly communicate with the neighboring cells (e.g., immunocytes, blood vessel cells, and stromal cells) to allow their survival and subsequent migration (namely metastasis). Therefore, the interrogation of these "cell talks" is critical to understand the biology of cancer cells and to design anti-cancer therapies.

Moreover, different "personalities" among phenotypically identical cancer cells have recently been revealed. Upon the treatment of a particular drug agent, the same cells within a tumor mass can exhibit remarkably distinct responses. Successful therapy should be able to eradicate those robust cells. This phenomenon, namely the single-cell heterogeneity, has thus been deemed essential for efficient drug discovery and precision medicine.

Innovative analysis methods are required to obtain in-depth insights into cellular activities, with the analysis ranging from cell populations to individual cells. However, the dynamic nature of such activities poses a major challenge for the current methods. Indeed, the current gold-standard assays to detect secretory molecules involve extra molecular labels on the analyte, such as fluorescent dyes and enzymes. Due to the tedious labeling steps, this requirement inevitably results in 'snapshot' endpoint readouts and dramatically compromises the temporal resolution of the analysis. The addition of extrinsic probes also alters the nature of the molecules of interest, which potentially generates distorted readouts. Furthermore, the

1

relatively large sample volume limits their application for single-cell measurement. Therefore, unravelling the dynamic profiles of cellular activities, including those at the single-cell level, calls for advanced analysis methods for real-time monitoring of the entire process.

In recent decades, label-free biosensor technologies have emerged as a promising solution. In particular, plasmonic biosensors have demonstrated excellent detection capabilities and miniaturization potential for point-of-care applications. However, real-time monitoring of cellular activities has only been reported in a few studies with these biosensors, all of which involved either cumbersome optical configurations or delicate sensor fabrication. Studies addressing label-free single-cell analysis are extremely rare due to the need for intricate system design for ultrasensitive and stable measurements. Therefore, this thesis is dedicated to the development of novel plasmonic biosensors, which can overcome the above challenges at different cellular resolutions in relatively simple optical set-ups. In particular, plasmonic biosensors based on gold nanohole arrays were employed. These arrays can be fabricated by a scalable procedure and support a unique optical phenomenon, the so-called extraordinary optical transmission (EOT). The spectral sensitivity of EOT to minute changes of refractive indices makes the biosensor suitable for biomolecular detection. The detection volume can be significantly reduced by incorporating state-of-the-art microfluidic systems, enabling the biosensor to measure secreted molecules from single cells.

Thesis outline

The background information is summarized in Chapters 1 and 2, with Chapter 1 focusing on the biological aspects of cell secretion, especially secretory protein molecules, and Chapter 2 dedicated to the detection principles of plasmonics and especially metallic nanohole arrays.

Chapter 3 is devoted to describing the experimental set-ups employed in the following chapters.

The study presented in Chapter 4 demonstrates for the first time the potential of the nanohole array-based biosensor as an exceptional analytical tool for secretion investigation. Secretion of vascular endothelial growth factor (VEGF) from microfluidic-cultured cancer cells was monitored in real time for over 10 hours in a label-free format.

Introduction

Chapter 5 introduces an innovative biosensor system for real-time secretion analysis at the single-cell level. To achieve this goal, a novel multi-functional microfluidic system was designed to minimize the detection volume and thus elevate the measurable concentration of target molecules. The monitoring interleukin-2 (IL-2) secretion from single lymphoma cells was achieved.

Beyond the enhancement of the biosensor's detection capability mentioned above, Chapter 6 reports on the sensor surface optimization for cell analysis. An artificial lipid bilayer membrane was generated on the sensor surface as a biomimicking interface for cell-cell interaction. A proof-of-concept study was performed on a surface plasmon resonance (SPR) setup, which can be readily transferred to other nanoplasmonic formats. This paves a new avenue for biosensor surface functionalization to enable biomimicking cell analysis in a label-free manner.

Finally, Chapter 7 summarizes the advancements of plasmonic biosensors for cell-based analysis. Some perspectives for future studies are also discussed.

Chapter 1

Cell secretion and analysis

As the fundamental functioning unit of life, the cell, a complex cocktail of biomaterials encapsulated within membrane structures, has been drawing enormous scientific attention for centuries. Mammalian cells, including human cells, undergo non-stop biological processes to communicate with the external environment and maintain essential functions. Among the diverse processes, the synthesis and functioning of proteins have been attracting considerable attention in biomedical research domains [1].

1.1 Proteins as the main secretion components

1.1.1 Molecular composition and conformation

Proteins, originating from Ancient Greek πρωτεῖος (prōteîos) or πρῶτος (prôtos) which means "primary" or "first," are a vast category of macromolecules consisting of one or multiple chains of amino acid residues (usually > 30). Although there are only 21 proteinogenic amino acids[*] found in eukaryotes (Table 1.1), researchers have estimated the number of protein species to be between 10,000 [2] and several billion [3] due to the sequences of amino acids as well as the four distinct levels of structural arrangements (Figure 1.1a) [4]. The huge variations of a

---

[*] Proteinogenic: "protein building".

protein enable a vast array of biological functions, virtually spanning over all processes within and around cells.

Table 1.1. The 21 proteinogenic amino acids in eukaryotes.

Amino Acid	Short	Abbrev.	Amino Acid	Short	Abbrev.	Amino Acid	Short	Abbrev.
Alanine	A	Ala	Glutamic acid	E	Glu	Histidine	H	His
Cysteine	C	Cys	Phenylalanine	F	Phe	Isoleucine	I	Ile
Aspartic acid	D	Asp	Glycine	G	Gly	Lysine	K	Lys
Leucine	L	Leu	Proline	P	Pro	Serine	S	Ser
Methionine	M	Met	Glutamine	Q	Gln	Threonine	T	Thr
Asparagine	N	Asn	Arginine	R	Arg	Selenocysteine	U	Sec
Valine	V	Val	Tryptophan	W	Trp	Tyrosine	Y	Tyr

Protein molecules are involved in every aspect of life activity, such as gene expressions, transportation of molecules within cells, enzymatic metabolisms, and immunological activities [1]. Nonetheless, one mistake in the peptide sequence can also result in misfolding of the protein structure, and can eventually generate the opposite biological functions (Figure 1.1b). A multitude of human disorders (such as Alzheimer's disease, Parkinson's disease, and Huntington's disease) are prone to result from irregular conformational changes of proteins [5]. Therefore, a growing panel of proteins has been established as indispensable biomarkers for disease progressions and pharmaceutical investigations [6], [7].

1.1.2 Protein secretion from mammalian cells

The secretory proteins, i.e. those that are produced and transported outside the cells, play a critical role in regulating basic life activities and consist of a large family of disease biomarkers [8], [9]. A large fraction of blood-derived protein biomarkers used in the clinic are directly related to secreted proteins, emphasizing the importance of this class of proteins [2]. Secretory proteins can be categorized according to their biological functions, such as enzymes, cytokines, and antibodies. Mammalian cells have a highly evolved process of protein secretion. These proteins are produced like any other proteins in mammalian cells, including the gene transcription and translation as described by the central dogma [10]. Following the synthesis and modification, the final protein products are packaged in secretion vesicles which are then fused with the cellular membrane to
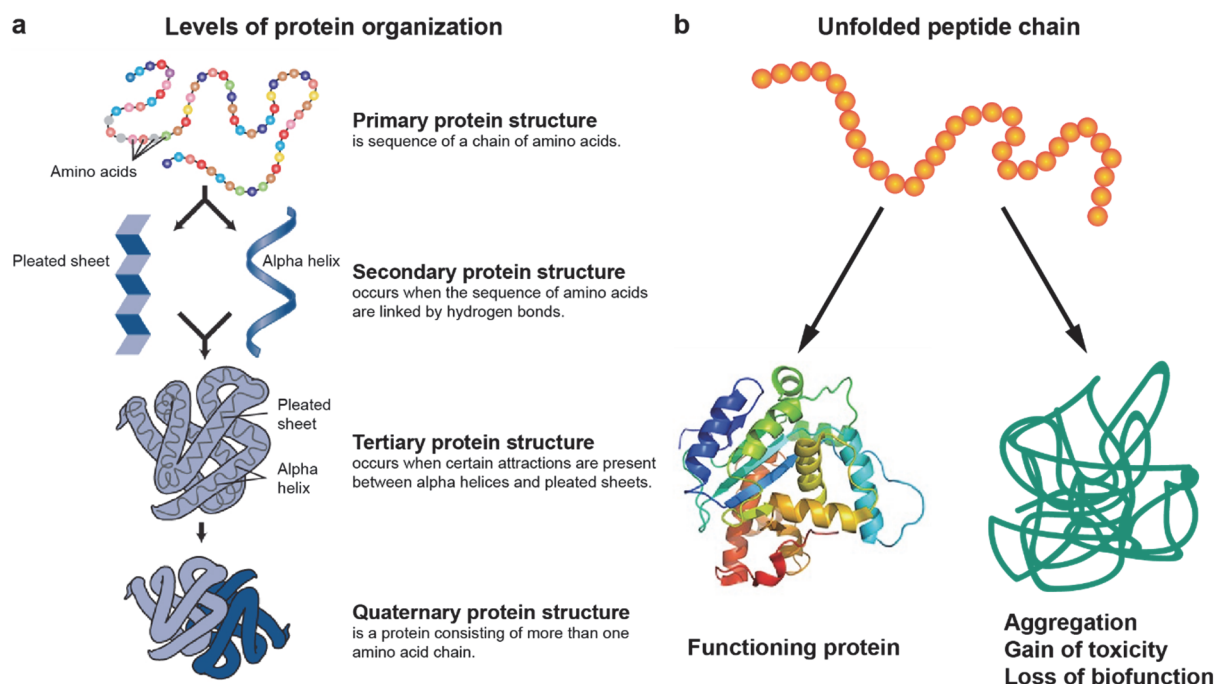
Figure 1.1. Conformation of protein molecules and protein misfolding. (a) Orders of protein structure. Image reprinted from [4]. (b) Structural misfolding alters the biological functions of the protein molecule.

release the contents out of the cell (Figure 1.2) [11]. The whole secretion cascade is thus extremely dynamic and responsive to both internal and external factors. Understanding the regulations of this process will bring invaluable insights to fundamental biology and drug development.

In general, the detection and quantification of protein secretion can be fulfilled by various analytical biochemistry assays based on different mechanisms. Determination of the total protein concentration in liquid samples can be achieved by relatively simple assays, such as protein-dye binding chemistry (Coomassie/Bradford) or protein–copper chelation chemistry (biuret/BCA) [12]. However, distinguishing certain species of proteins requires more advanced detection principles. For example, the immunochemistry mechanism is widely applied to guarantee a selective detection, which is essential for studying secretory proteins in disease diagnosis.
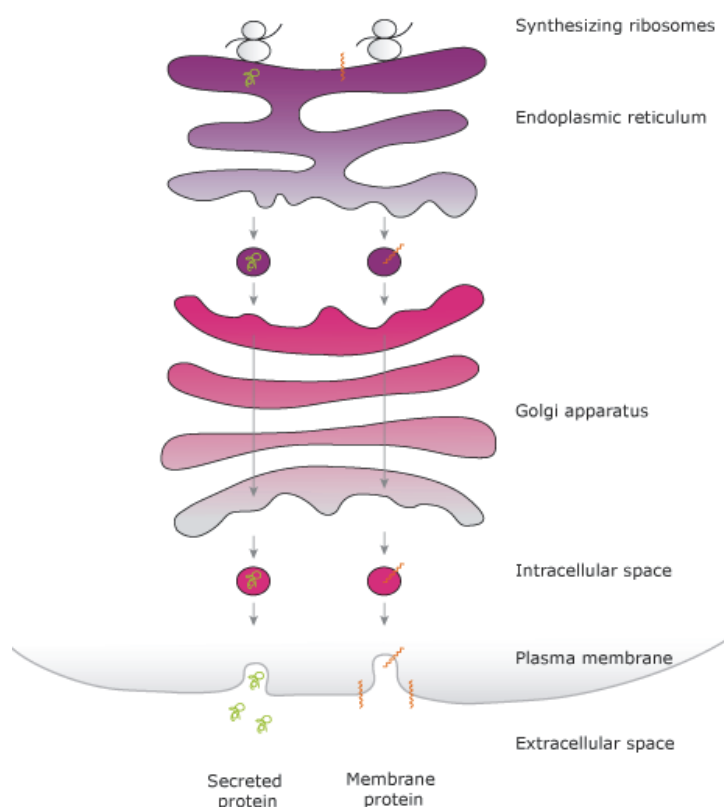
Figure 1.2. An illustrative overview of the protein secretory pathway. Image reproduced from [11].

1.2 Analysis of secretory proteins

1.2.1 The significance of analyzing secretory proteins

Secretory proteins are responsible for numerous biological functions, such as cell proliferation, differentiation, cancer progression, and immune responses [8], [13]. For instance, protein growth factors expressed within the tumor microenvironment regulate tumor development and progression in different stages [8]. In clinical practices, the diagnosis of multiple diseases relies substantially on the detection of protein biomarkers [14], [15]. In particular, analyzing the time course of secretion activity provides vital insights: variations in the levels of protein biomarkers indeed reveal distinct disease stages [16], [17]. On the other hand, tracking the temporal changes in cancer cell secretions has led to the discovery of new cancer biomarkers [18], [19].

1.2. Analysis of secretory proteins

In addition, conducting the analysis at the single-cell level provides invaluable information. Like human beings, each cell individual has a distinct "personality" despite sharing the same phenotype and genomes (Figure 1.3). Many studies have shown that single-cell heterogeneity can be uncovered in copious aspects of cellular functionalities [20]–[23]. Although many bioanalytical methods study the ensemble cellular behavior, biomedical researchers have started to realize that investigating and screening individual cells will revolutionize the biological knowledge and drug discovery.

Therefore, single-cell analysis is nowadays one of the most formidable technological approaches for understanding fundamental biology and developing effectual therapeutics for serious diseases [20]. The recent development of novel detection methodologies has advanced our understanding of single-cell heterogeneity in genome, epigenome, and transcriptome [21]. Meanwhile, secretions of different biomolecules are indispensable to decode the underlying mechanisms of cell-cell communications. The signaling and formation of cellular networks are highly dynamic, being mediated by the production and exchange of small proteins (e.g., cytokines) and other molecules, which define the particular cell behaviors and functionalities [24], [25]. Yet, the heterogeneous secretome is still challenging to investigate. Conventional techniques including enzyme-linked immunosorbent assay (ELISA) or immunofluorescence staining require large amount of sample and thus lack sufficient sensitivity to detect single-cell
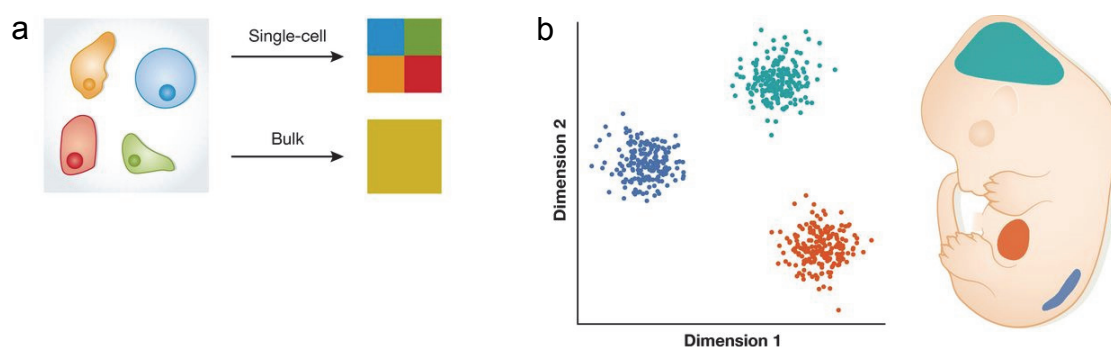
Figure 1.3. New technology reveals single-cell heterogeneity. (a) Gene expression assays with bulky cell population only provide an average read-out over many cells, whereas single-cell RNA-seq technique distinguishes different gene expression in individual cells. (b) Single-cell analysis techniques enable studies involving complex systems such as animal embryos, where cells with drastically distinct genetic profiles can be analyzed without cross-contamination from neighboring tissues. Image reproduced from [23].

secretions [26]. Therefore, besides reviewing the current standard analysis technologies, various biosensor techniques, specifically novel label-free methodologies will be introduced for real-time bioanalytical detection.

1.2.2   Classical analysis techniques

The quantification of secretory proteins is an integral part of protein studies. Due to the incomparable physical sizes, we cannot quantify the number of protein molecules under a microscope as the way we do with mammalian cells. It is necessary to correlate the concentration of the substance of interest with measurable physical value. According to Beer-Lambert law [†] if the solute in the sample absorbs light at a specific wavelength, the attenuation/absorbance is directly proportional to the concentration of the solute. Therefore, it has become a standard mechanism applied in analytical proteomic assays by spectrophotometry, such as enzyme-linked immunosorbent assay, the so-called ELISA. A decade after the invention of ELISA, a derivative technique, ELISpot, emerged to further enumerate the protein-secreting cells. Light absorption can also activate fluorescence emission, which enables another powerful format for protein analysis.

ELISA

ELISA has become a gold-standard assay format to quantify soluble molecules of interest in biochemical assays and diagnostic laboratories. First conceptualized by Peter Perlmann and Eva Engvall in 1971 [27], ELISA demonstrated its remarkable performance on the quantitative measurement of rabbit antibody. As a solid-phase immunoassay (Figure 1.4), the analytes are first immobilized on the microtiter plate non-covalently (e.g., direct ELISA) or via an additional layer of antibodies (e.g., the capture antibodies in sandwiched ELISA). The detection antibodies labeled with enzymes, such as alkaline phosphatase, are subsequently applied over the surface-bound targets. By adding the substrate materials of the labeled enzymes, a detection signal is generated, most commonly a color change of the liquid solution.

[†] $A = \varepsilon \cdot L \cdot c$, where A is the measured absorbance, ε is the wavelength-dependent molar absorptivity coefficient, L is the path length, and c is the analyte concentration.
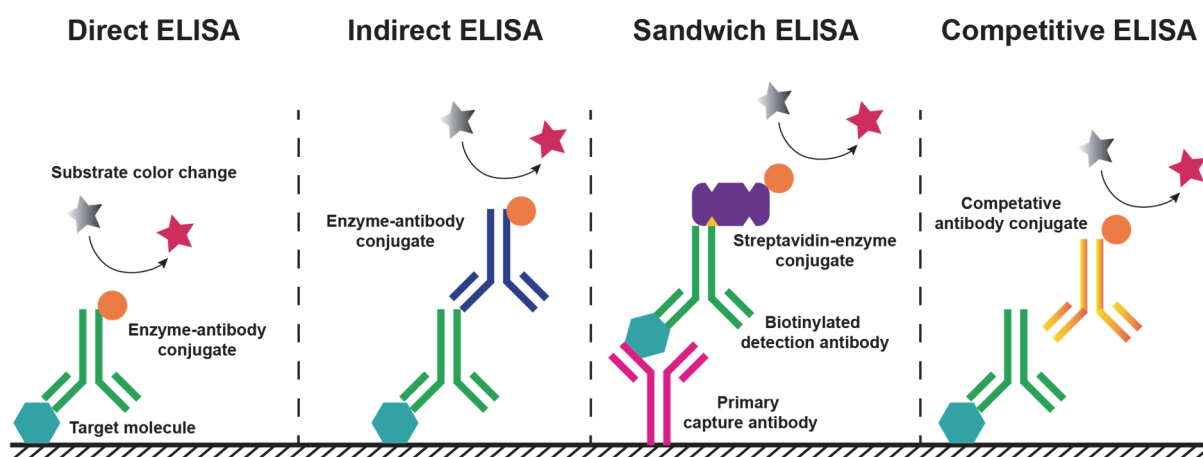
Figure 1.4. Different types of ELISA assays.

The concentrations of the target analytes are thus correlated to the absorbance of the colored solution under a specific wavelength of light. By employing the colorimetric mechanism of enzymatic catalysis, the presence of target molecules recognized by antibody-antigen binding is considerably amplified, and the detection sensitivity can easily reach several picograms per unit volume.

ELISpot

The enzyme-linked immunospot assay, or the so-called ELISpot, is another classical colorimetric assay derived from ELISA. First described and coined as this name by Cecil Czerkinsky in 1983 [28], the ELISpot assay has been adopted for multiple biochemical tasks, the most prominent being the enumeration of single immunocytes secreting one or several certain types of cytokines upon external stimulations. Unlike ELISA, ELISpot employs polymer membrane-based substrate (e.g., polyvinylidene difluoride, PVDF) in a microtiter plate for the coating of capture antibodies. As shown in Figure 1.5 [29], cells of interest, as well as the stimuli, are first pipetted into the wells and incubated for a specified duration. During this period, the antibodies located in close proximity to the secreting cells capture the secreted analyte. After removing any cells and unbound substances, the subsequent steps coincide those of ELISA. Nonetheless, instead of the color change of the solution, a purple-blue precipitate appears as spots at the sites of analyte capturing, with each spot signifying an

individual analyte-secreting cell. The quantification is done by automated or manually counting. However, quantitative molecular analysis becomes challenging.
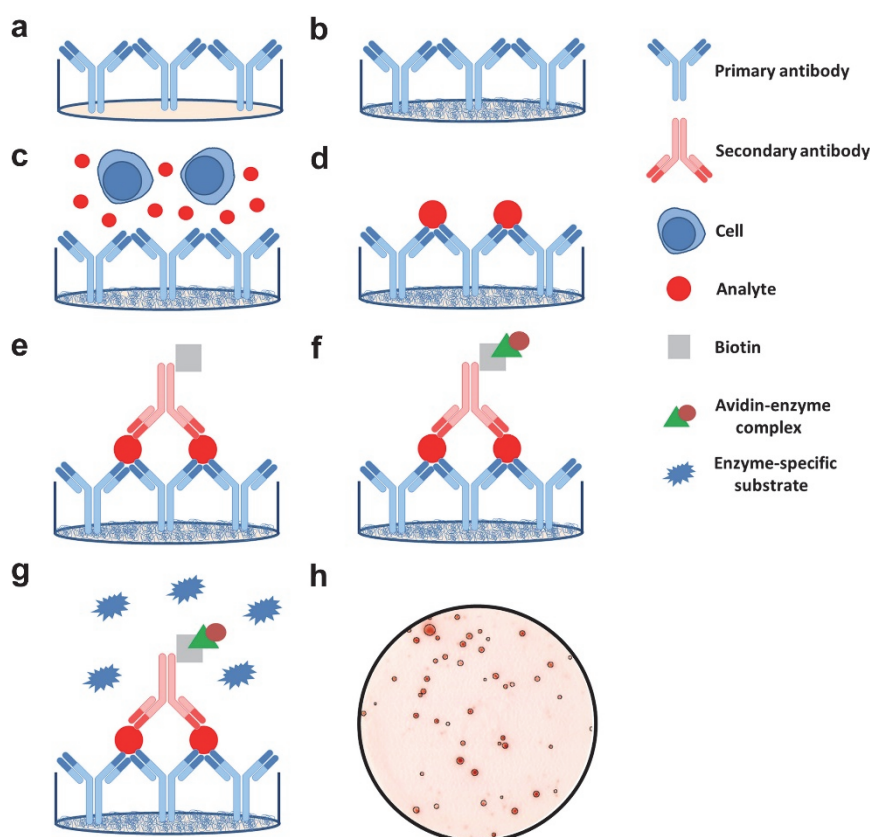
Figure 1.5. A schematic overview of ELISpot assay. (a) Primary capture antibodies are coated on the polymer membrane substrate. (b) Extra sites on the surface are blocked to minimize unspecific binding. (c) Cells as well as stimuli are subsequently added to the coated wells. By responding to the external stimuli, the active cells secrete the analyte molecules (e.g., cytokines). (d) Analytes are captured and bind to the antibodies around the cells, which are removed before proceeding the assay. (e) A secondary biotinylated antibody is added, which binds to the respective analyte-antibody conjugate. (f) Avidin-enzyme complex binds to the biotinylated detection antibody based on the robust avidin-biotin recognition. (g) Addition of the enzyme substrate solution transforms the analyte binding events to visible colored dots absorbed by the polymer membrane. (h) An example image of ELISPOT result, with each dot representing a secretory cell. Figure reproduced from [29].

Immunofluorescent assays

Besides colorimetric formats, immunofluorescence methodology could also be employed to quantify protein targets and analyte-secreting cells. Similarly, the assay specificity is guaranteed by superior antibody-antigen binding. By replacing the enzyme labels with fluorophores on the detection antibodies, the presence of specific protein targets is indicated

by the distinct light emission of the dye molecules upon selective light excitation. Multiplexing the assay for different analytes with a single sample is also feasible by labeling each antibody with fluorophores emitting at different wavelengths. However, the emission intensity is extremely responsive to the source intensity of excitation and downstream imaging parameters (e.g., exposure time, image gains), resulting in semi-quantitative readouts and less applicability.

1.2.3 Biosensors and label-free methodologies

What is a biosensor?

"A biosensor is a device incorporating a biological sensing element either intimately connected to or integrated within a transducer," as defined by Anthony P.F. Turner in 1987 [30]. Such a device produces a digitally measurable signal in proportion to the number of target chemicals. Therefore, there are three fundamentals for constructing a biosensor: biorecognition element, signal transduction mechanism and signal recording/processing (Figure 1.6). Biorecognition elements capture the specific target molecules to guarantee the selectivity of the assay. There are probe molecules that naturally bind to a specific target, such as immunoglobulins, the so-called antibodies, or that are artificially designed to have high affinity to the targets, such as DNA aptamers. Upon the selective probe-target binding, a corresponding means of the signal will be generated depending on the transduction mechanisms, which is recorded and analyzed
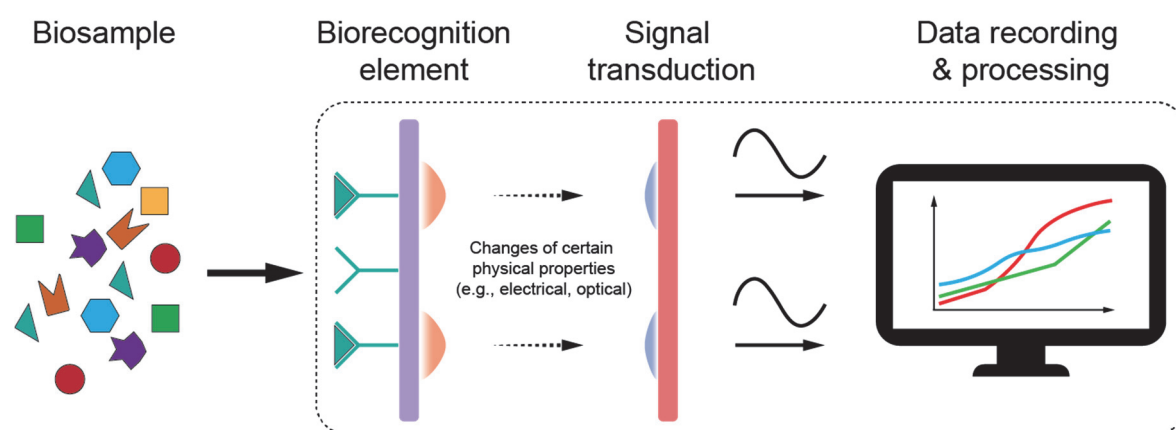
Figure 1.6. Structure of typical biosensor devices (boxed), including a biorecognition element that can distinguish and capture target molecules from heterogeneous biosample, a signal transducer and the final signal processing.

by the subsequent detectors. For instance, Wang et al. labeled the *E. coli* bacteria with antibody-coated magnetic and gold nanoparticles, forming a sandwiched structure. By this means, the existence of the bacterial targets is thus tranduced to the number of metallic nanoparticles that can be easily measured by differential pulse voltammetry (DPV) on an electrode chip [31]. Biosensors have been established as powerful bioanalysis tools for pharmacokinetic studies, biochemical research, medical diagnosis, and the pharmaceutical industry.

Label-free biosensors

The external molecular labels are indispensable for the implementation of classical analytical biochemistry assays, such as the enzymes mentioned above and fluorophores tagged on detection antibodies. Despite the outstanding sensitivities obtained from the labels, several critical drawbacks impede broader applications of this methodology. The most conspicuous is the endpoint analysis readout resulting from the labeling steps, which cripples the practice of such a methodology for continuous monitoring of binding kinetics. As such, there has been a strong drive to foster label-free biosensors that enable real-time quantitative monitoring of kinetics while reducing assay complexity.

Label-free biosensors have emerged to enable continuous, real-time monitoring of molecular binding kinetics, and rapid target detection. Being termed as 'label-free,' such assays eliminate the use of external labels (e.g., enzymes, fluorophores, and nanoparticles) that are traditionally employed to signify the existence of targets. Therefore, we do not need to pre-treat the sample before the signal acquisitions. As soon as the sample is applied to the biosensor, it will be recognized by the probe molecules, and a corresponding detectable signal will be immediately transduced and generated for the following readout. The amplitude of the signal is dependent on the target concentrations, representing an outstanding quantification methodology.

Label-free assays are typically surface-based, where the transducer surface is coated with bio-recognition elements to capture the targets-of-interest specifically. The single step of surface functionalization significantly reduces the assay complexity and facilitates high-throughput multiplexed bioanalysis in a more straightforward format. According to the signal transduction mechanisms, label-free biosensors are principally classified into **electrochemical**, **mechanical**, and **optical** biosensors.

Electrochemical label-free biosensors transduce the biochemical binding events to the electrical domain. Depending on the mode of electrical signal transduction, there are five subdivisions [32], [33] that have been distinguished: amperometric/voltammetric biosensors, potentiometric biosensors, conductometric biosensors, impedance biosensors, and field-effect transistor (FET) biosensors (Figure 1.7a). The most iconic application by far is the electrochemical detection of glucose in the blood, proposed by Leland C. Clark, Jr. and Champ Lyons in 1962 [34]. In this work, glucose oxidase was coated on the electrode that was initially designed for oxygen monitoring. The oxidation of glucose in liquid (e.g., patient blood) by the immobilized enzyme results in alterations of redox current, which can be recorded by electrodes (Figure 1.7b). This ground-breaking research presented the prototype of a glucose sensor and inspired the following generations of glucose biosensors worldwide [35]. Ever since, the field of electrochemical biosensing has gained considerable attention, leading to numerous sensitive biosensor format, such as the well-known electrochemical impedance spectroscopy (EIS) technique [36]. However, due to the nature of the detection mechanism, any alteration of the electrochemical properties in the fluid like the ionic strength or pH values will lead to signal fluctuation, imposing a strict control strategy over the assay [32], [37].

Mechanical label-free biosensors, as indicated by the naming, detect the mechanical alterations caused by the target biomolecules, often the molecular mass. For the majority of mechanical sensors, the central element is a microscale cantilever which works either in surface-stress fashion or dynamic mode (Figure 1.7c and d) [38]. For surface-stress sensors, they measure the quasistatic deflection of the cantilever, caused by the surface binding of biomolecules. By pulsing a laser beam onto the cantilever in a certain angle, the reflection output alters according to the amount of deflection. For the dynamic-mode sensors, the cantilever oscillates with a characteristic resonance frequency. The frequency changes accordingly upon the landing of biomolecules on the cantilever. Besides the cantilever-based nanomechanical sensors, there is another widely applied mechanical platform: the quartz crystal microbalance (QCM) (Figure 1.7e) [39]–[41]. These microbalances are mechanical resonators that oscillate with a specific frequency. Alterations in the resonant frequency occurs with the accretion of target molecules, which can be reliably tracked electronically. Despite the hypersensitivity, mechanical

biosensors provide exquisite performance mostly in vacuum and air, makes these assays cumbersome and challenging for fluid-phase measurements.

Optical label-free biosensors transduce the binding of target biomolecules on the sensor surface to discrepancies in optical signals, such as wavelength, light intensity, and propagation velocity. These sensors usually exploit the evanescent field generated by highly confined light as the detection probe (Figure 1.7g) [42], [43]. The light confinement is mostly achieved either in photonic waveguides [44] or at the dielectric-metal interface [45], [46]. The binding of biomolecules induces a local change of the optical properties (e.g., the refractive index) and disturbs the propagation of the evanescent field, which is immediately translated into a proportionally measurable optical signal. Interferometers [47], photonic ring resonators (Figure 1.7f) [48], [49] and plasmonic biosensors [45], [50] are some typical examples of evanescent wave biosensors. In particular, plasmonic biosensors based on the well-known surface plasmon resonance (SPR) phenomenon have achieved tremendous scientific interests and are nowadays the most widely commercialized label-free optical sensors.

1.2.4   Progress of label-free biosensors for cell analysis

Cell-based assays have been drawing increasing attention in fundamental research and preclinical studies. In particular, the urge for early cancer diagnosis has been promoting the development of biosensing techniques which can enable fast and sensitive detection of cancer biomarkers in liquid biopsy. Biomarkers for early cancer diagnosis exhibit a wide spectrum of both physical and biochemical characteristics, ranging from protein factors and nucleotide debris (e.g., mRNAs, cDNAs) to extracellular vesicles (e.g., exosomes) and circulating tumor cells, namely CTCs. Label-free biosensors that facilitate early cancer biomarker detection for monitoring the disease progression have unprecedentedly advanced in the recent years.

Among various principles, electrochemical biosensors offer excellent advantages due to their fast response, low cost and potential for miniaturization. Kilic et al. have demonstrated a remarkable label-free detection of exosomes secreted by human breast cancer cells via Differential Pulse Voltammetry (DPV) and Electrochemical Impedance Spectroscopy
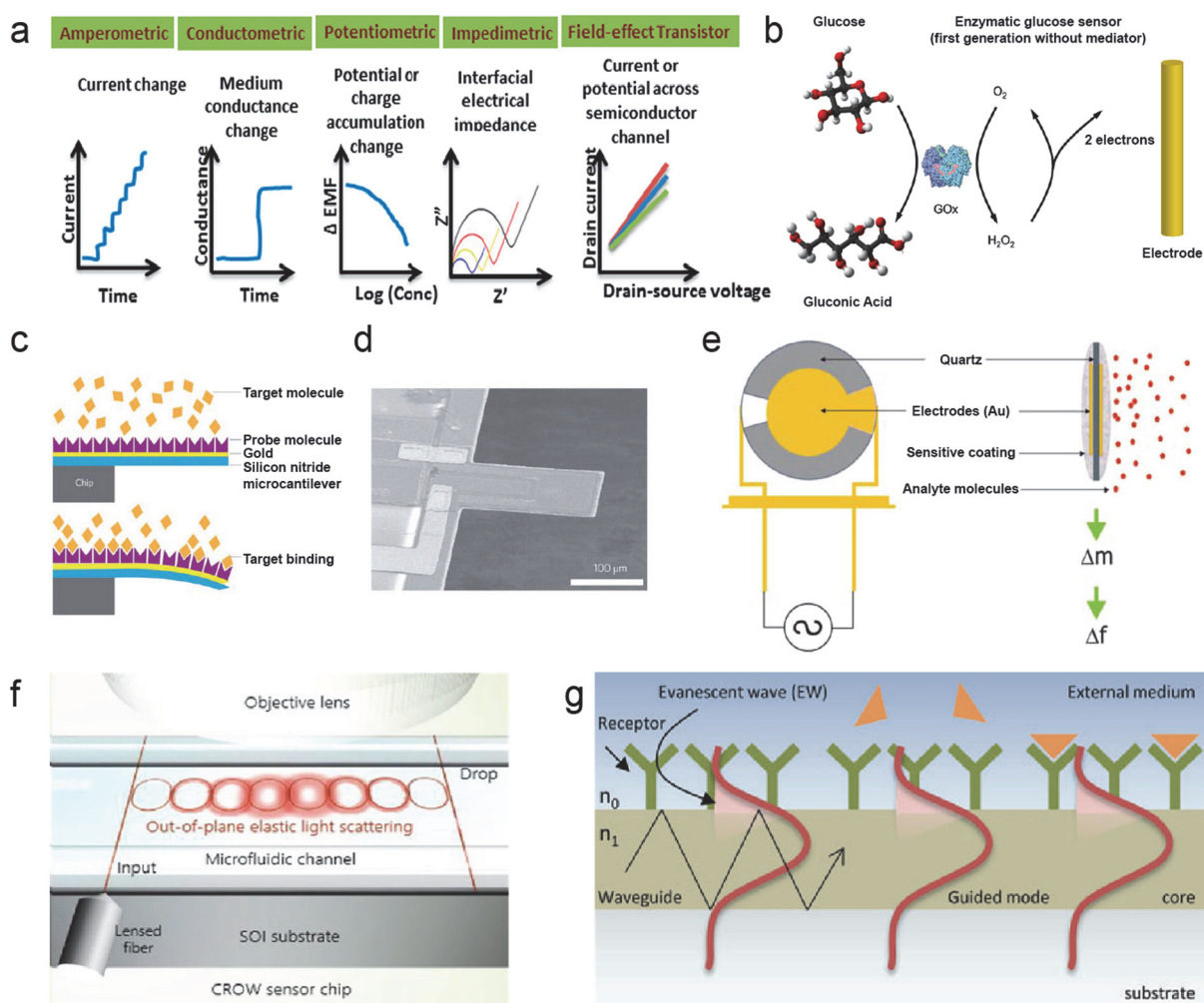
Figure 1.7. An illustrative overview of label-free biosensing principles. (a) Different modes of electrical signal transduction for electrochemical biosensors, such as glucose sensor (b). Image reprinted from [32], [34]. (c) Principle for mechanical sensing with a quasistatic microcantilever, and an SEM image of a cantilever used in dynamic mode (d). Image reprinted from [38]. (e) Principle of quartz crystal microbalance (QCM). Image reprinted from [40]. (f) Schematic of an SOI CROW-based optical sensor with eight coupled microring resonators in an add-drop filter configuration. SOI: silicon-on-insulator. CROW: coupled-resonator optical waveguide. Image reprinted from [48]. (g) Sensing principle of evanescent field-based optical biosensors. Image reprinted from [43].

(EIS) [51]. A wide density range of 10^2-10^9 EVs/mL has been distinguished by the sensor. Zhou et al. have provided an extensive overview of recent advances in using miniaturized electrochemical sensors for detection of multiple cancer biomarkers in liquid biopsies [52]. In addition, electrochemical biosensors have also demonstrated noticeable applications in monitoring physiological and pathological indices for organ-on-a-chip (OoC) platforms, such

17

as pH values, oxygen levels and cytokine concentrations [53]–[55]. For instance, Zhou et al. have reported a smart integration of microfluidic liver-on-a-chip model with electrochemical sensor to monitor liver cell signaling during alcohol injury process [56]. Alcohol-induced injuries are associated with upregulated Transforming growth factor (TGF)-β signaling. Their microfluidic design incorporated co-cultures of hepatocytes (liver cells) and stellate cells (a major cell type involved in liver fibrosis) with aptamer-coated electrodes. The responses of different cells upon injury stimulation were selectively monitored by pneumatic operation of the microfluidic system (Figure 1.8). A profound review of electrochemical biosensors applied in OoC monitoring has been provided in [57].
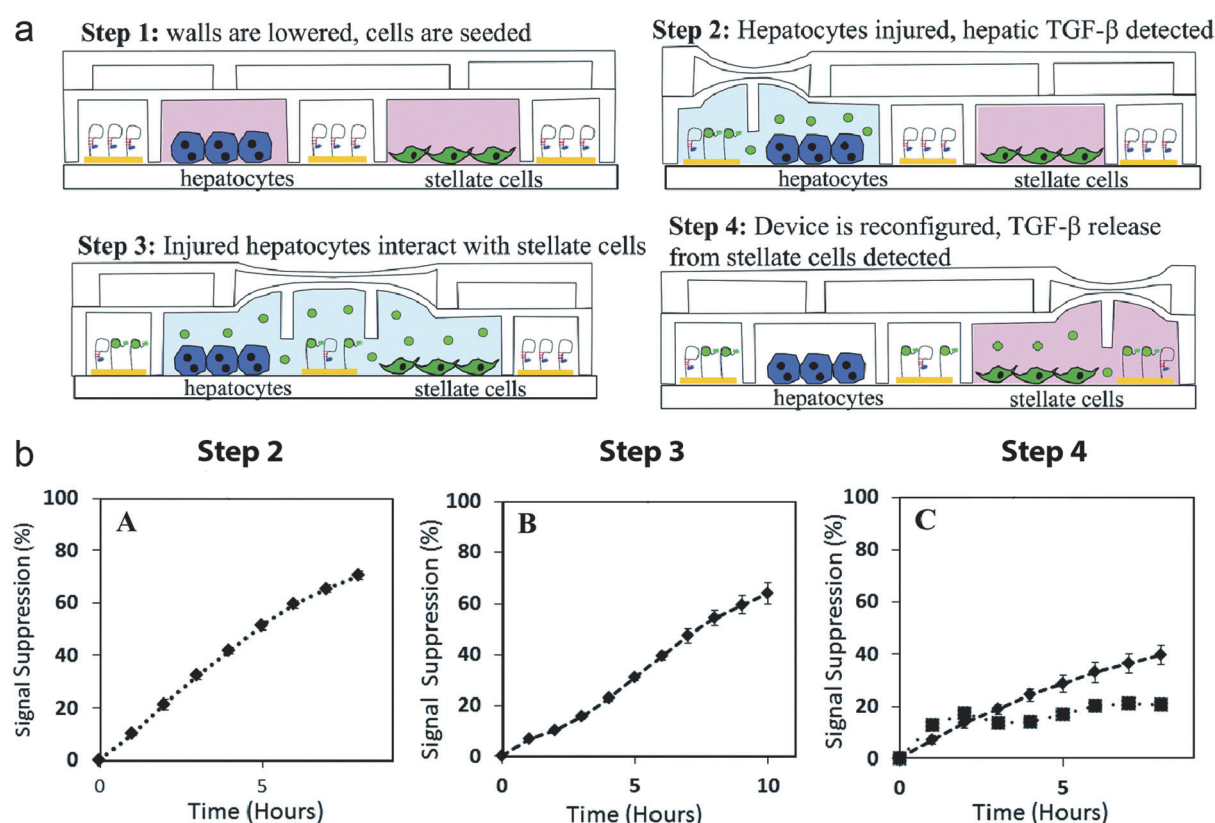
Figure 1.8. The study of alcohol-induced liver injury by employing an electrochemical biosensor in a liver-on-a-chip. (a) An illustration shows how the liver injury was initiated by pneumatic operation on the microfluidic system. (b) Kinetics of TGF-β signaling in different steps during liver injury. Image reproduced from [56].

Mechanical label-free biosensors, especially those based on atomic force microscopy (AFM), have demonstrated exceptional capability and resolution for cell analysis. For instance, by

exploiting the ultrasensitive mechanical readouts of the cantilever, Calzado-Martín et al. investigated the different cellular stiffness among normal human breast cells and breast cancer cells with high-resolution AFM imaging (Figure 1.9) [58]. Despite the complex system implementation and vulnerability of cantilever probes, AFM imaging-based techniques have been widely employed for investigating the cell-cell or cell-molecule interactions, particularly for diagnosis of cancer as summarized by Kwon et al. [59].
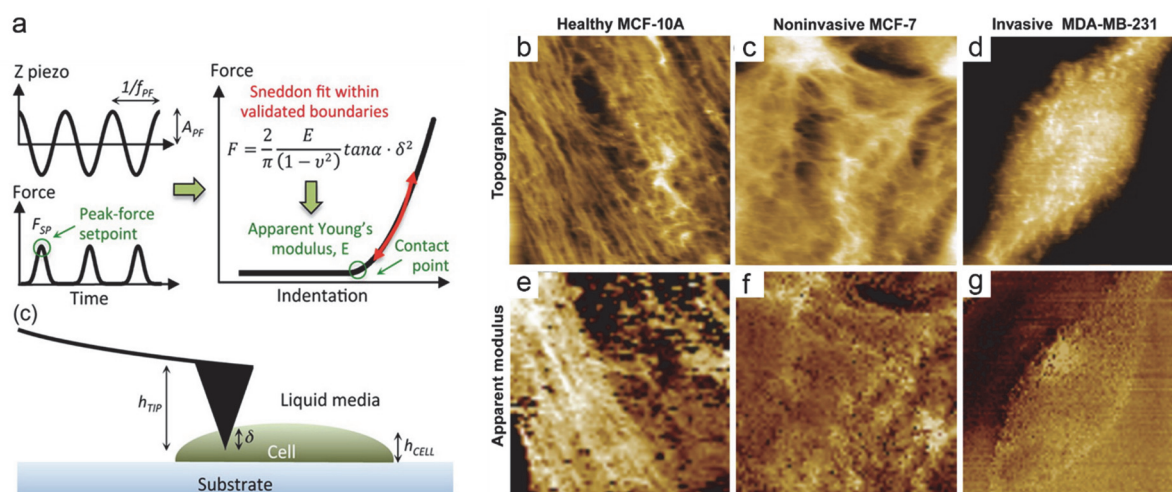
Figure 1.9. Schematic representation of live cell imaging using peak-force modulation AFM. (a) Working principle of AFM-based cell stiffness measurement. (b)-(g) AFM images of the cell surface topography and the corresponding apparent Young's modulus images (from 2.5 to 250 kPa). Images reproduced from [58].

Besides the classical techniques for label-free detection, new detection principles have been emerging with novel advantages to facilitate direct analysis of different analytes, especially with ultralow limit of detection and good miniaturization potential [60]. For instance, field-effect transistors (FET) based on carbon nanotubes, silicon nanowires and graphene have shown promising results for label-free detection of enzymatic reaction, antibody-antigen bindings and cell-based recording. Their fast response, ultrahigh sensitivity, massive manufacturing and facile miniaturization have drawn tremendous attention as new possibilities for label-free biosensors.

Chapter 2

Plasmonics: a unique principle for label-free optical biosensors

As a rapidly developing field, plasmonics bridges optics and biology, offering a new powerful tool for quantitative biomedical studies. It has been established as the principle for refractive index-based photonic sensing. The study of plasmonics focuses on the interaction between electromagnetic radiation (such as light) and metals, the so-called phenomena of surface plasmons (SPs). SPs are coherent electron oscillations propagating at a metal-dielectric interface. The resulting electromagnetic field associated with SPs, the evanescent field, is sensitive to changes of refractive indices in immediate vicinity of the interface. Therefore, plasmonics biosensors are mostly employed as refractometric sensing devices.

There are two main modes of SPs to function for biosensing: the surface plasmon resonance (SPR) on a planar metal film and localized surface plasmon resonance (LSPR) associated with metallic nanostructures.

2.1   Surface plasmon resonance

This renowned optical phenomenon has established widespread applications in numerous molecular detection applications since its first observation by Wood in 1902. A complete physical interpretation was done in 1968 when Otto [61] as well as Kretschmann and Raether [62] reported the excitation of surface plasmons. Another 15 years passed until Liederberg et al. demonstrated the first application of SPR-based sensors to monitor biomolecular interaction

[63]. SPR biosensors have so far exhibited excellent detection capabilities in environmental monitoring, food quality and safety analysis, medical diagnostics and drug discovery [64].

The principle of SPR sensing is a non-radiative electromagnetic surface wave, namely surface plasmon polaritons (SPPs) [65]. As shown in Figure 2.1, the wave propagates in a direction parallel to the interface of metal-dielectric medium (e.g., air, water), which is characterized by the wave vector k_{SPP}:

$$k_{\text{SPP}}(\omega) = \frac{\omega}{c}\sqrt{\frac{\varepsilon_d\,\varepsilon_m(\omega)}{\varepsilon_d + \varepsilon_m(\omega)}} \qquad (2.1)$$

where ω represents the angular frequency of light, c is the speed of light in vacuum, ε_d is the dielectric constant of the surrounding medium. In particular, $\varepsilon_m(\omega)$ is the complex function for the dielectric constants of the metal:

$$\varepsilon_m(\omega) = 1 - \frac{\omega_p{}^2}{\omega^2} \qquad (2.2)$$

wherein ω_p is the plasma frequency of the metal, e.g., $\omega_p \approx 1.28 \times 10^{16}$ Hz for gold [66]. Equation (2.2) clearly indicates that the dielectric function of the metal is frequency dependent, resulting in $\varepsilon_m > 0$ or $\varepsilon_m < 0$ for light frequencies above or below the plasma frequency, respectively. Furthermore, with the derivation of Equation (2.1), SPPs are solely supported when the real part of $\varepsilon_m(\omega)$ is negative and $|\varepsilon_m(\omega)| < \varepsilon_d$. Therefore, SPPs can only be
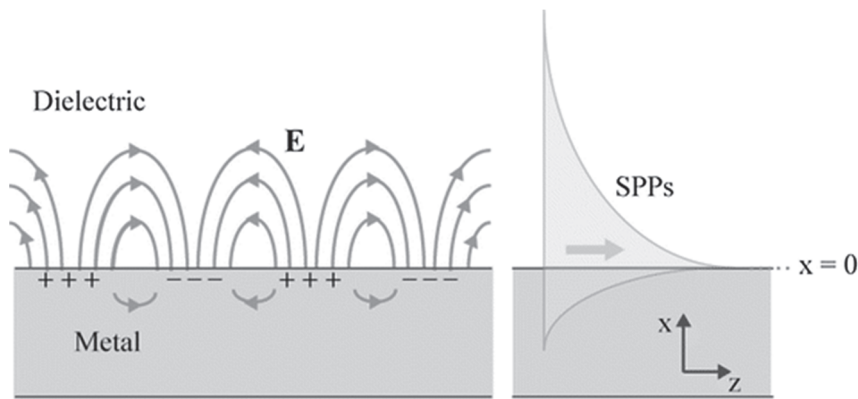
Figure 2.1. Propagation of SPPs at the metal-dielectric interface. Left: the collective electron oscillation at the surface. Right: distribution of the evanescent field. Image reprinted from [65].

fulfilled at the interface between metal (commonly gold or silver) and a dielectric medium at optical radiation wavelengths (100 nm~1 mm, DIN 5031‡).

The evanescent field generated by the SPP wave is confined at the interface and decays exponentially mainly into the dielectric medium (Figure 2.1). The decay length – the penetration depth – depends on the light wavelength and the dielectric properties of both materials. As a critical parameter for plasmonic sensing, it typically measures 100-500 nm within the visible and near-infrared spectrum [67]. Only the biomolecular interaction occurring within this depth can interfere with the SPP propagation and hence produce a detectable signal.

Generally, the wave vector k_{SPP} is considerably larger than that of the incidence light regardless of the incidence angle. This is the reason why SPR cannot be excited by direct light illumination on the metal-dielectric interface. There are several techniques to effectively couple the incident light for SPR excitation (Figure 2.2), among which the most common method is the Kretschmann configuration [50]. As shown in Figure 2.2a, the light illuminates the back side of a thin metal film through a glass prism. When polarized light shines through the prism, it is reflected by the metal film acting as a mirror. Upon reaching a certain incidence angle, the intensity of the reflected light reaches a minimum. At this angle, the incident light will excite
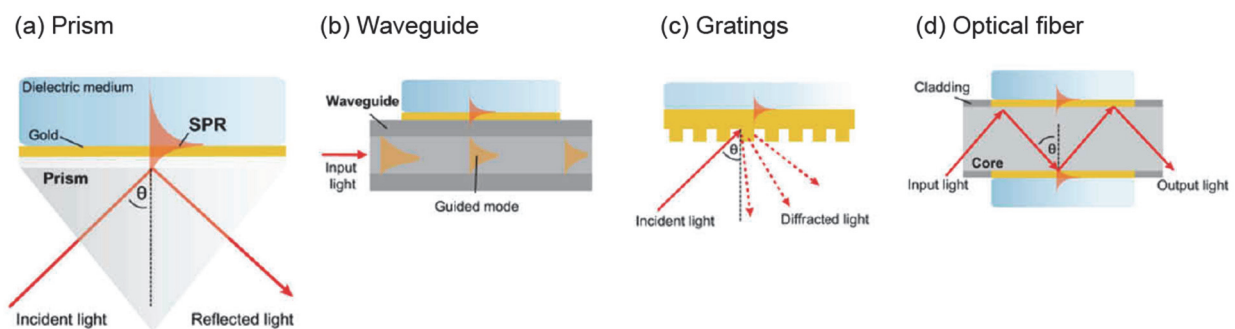
Figure 2.2. Different light coupling configurations for SPR excitation. The Kretschmann configuration is shown in (a). Image reprinted from [50].

---

‡DIN Standards for "Optical radiation physics and illumination Engineering". DIN stands for Deutsches Institut für Normung, which is the German national organization for standardization.

the surface plasmons, generating a penetrative evanescent wave through the metal film. This angle is thus named as resonance angle or SPR angle.

The SPR angle is highly responsive to changes of optical properties of the setup, such as the refractive indices of the external medium on the metal surface. In biosensing applications, such changes are commonly induced by the binding of molecules of interest (e.g., proteins). Therefore, the real-time monitoring of the molecular interactions and binding kinetics are decoded by tracking the shifting of SPR angle without the need for extra labeling (Figure 2.3) [68].

2.2   Localized surface plasmon resonance

Gold/silver colloidal suspensions have been widely used in stained glass since the middle ages: light appears yellow after transmitting through a silver colloid while ruby red through a gold
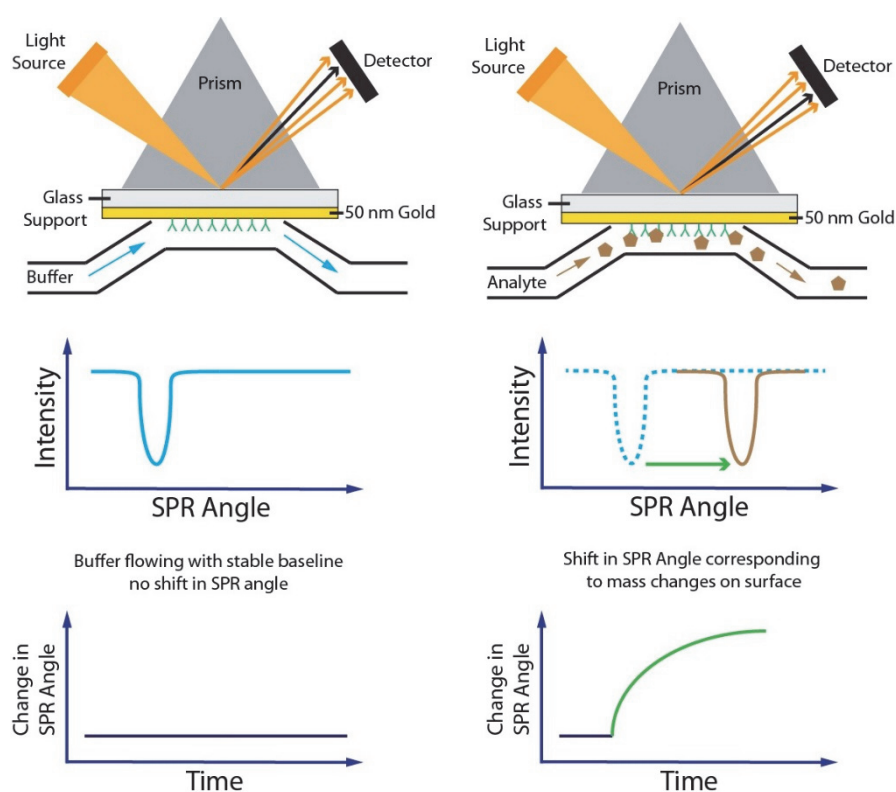
Figure 2.3. Real-time monitoring of analyte binding by tracking the changes in SPR angle. Image reprinted from [68].

colloid. Further investigations attribute this phenomenon largely to light absorption and scattering induced by the embedded metallic nanoparticles. Nowadays, the advancement of nanofabrication and chemical synthesis technologies have further enabled precise control over the size of metallic nanostructures, especially below the wavelength of light. This urges the study of optical phenomena at nanoscale metal surfaces, nanoplasmonics.

Unlike SPR, the surface plasmons excited by light are collectively oscillating within the near-field in the metallic nanostructures, known as localized surface plasmon resonance (LSPR, Figure 2.4) [69]. The resulting evanescent field is highly confined in a nanoscale volume and decays rapidly into the surrounding dielectric medium. The resonance frequency (i.e., maximum light absorption) of LSPR nanostructures can be simply tuned by changing the size, shape, and composition of the nanoparticles, as well as the bulk refractive index of the dielectric medium. Therefore, the resonance wavelength of the nanoparticles likewise shifts sensitively according to the local changes of the refractive index, such as the binding of target biomolecules.
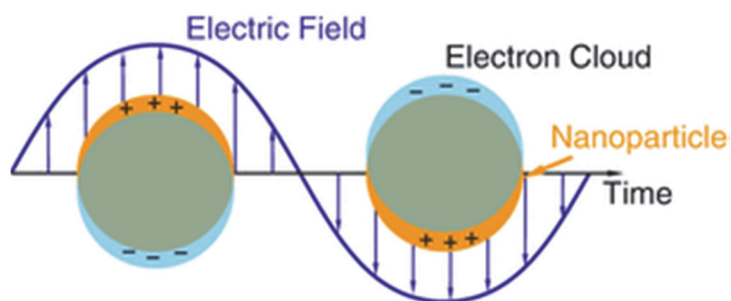
Figure 2.4. Illustration of localized surface plasmon resonance (LSPR). Coherent electron oscillations in the nanoparticle is induced by the oscillating electric field of the incident light. Reprint from [69].

As the basis of nanoplasmonics, LSPR phenomenon has been applied extensively for label-free biosensors. However, it requires additional effort to disperse metallic nanoparticles in solution to avoid the formation of particle aggregates. This urges the engineering of surface-based metallic nanostructures for nanoplasmonic sensing. The LSPR of these arrays can be excited by light illumination at normal incidence. The resonance of the nanostructures strongly

absorbs the light at certain wavelengths, generating characteristic light extinctions that can be analyzed in the transmission spectrum (Figure 2.5a). The nanoscale confinement of light around the nanostructure also allows higher spatial resolution for single particle/molecule biosensing. In such measurements, light scattering analysis is preferred to provide a higher signal-to-noise ratio, which will better distinguish the excitation light and the light absorbed by the nanostructures. This can be achieved by dark-field (DF) or total internal reflection (TIR) microscopy (Figure 2.5b and c). Moreover, compared to the SPR-based counterparts, the LSPR-based biosensors enable high-throughput analysis in a compact manner due to the flexible fabrication scheme and spectral configuration, providing a suitable format for point-of-care applications.
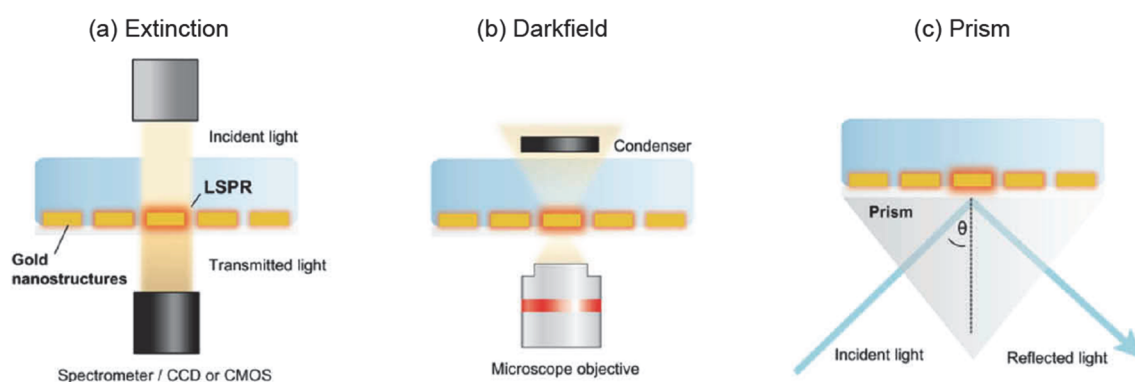
Figure 2.5. Excitation schemes of LSPR biosensors through light extinction measurement (a), dark field microscopy (b) and prism-coupling scheme (c). Image reprinted from [50].

2.3 Plasmonic nanohole arrays

Both SPR and LSPR can be employed as label-free biosensors to investigate real-time biomolecular interactions. Interestingly, one format of nanoplasmonic biosensors has emerged in the latest decades which can support both phenomena at one time: plasmonic nanohole arrays. With nanoscale apertures situated on a planar thin metal film, SPPs propagate along the metal-dielectric interface while the nanostructures confine localized plasmon resonances. By tuning

the size, shape as well as the arrangement, the optical properties of such unique nanoplasmonic structure can be tailored for efficient and sensitive biomolecular investigations.

2.3.1 A single metallic void vs. a single metallic particle

As discussed in section 2.2, a single metallic nanoparticle surrounded by dielectric medium can confine the collective electron oscillations locally around itself. Likewise, a single dielectric nanoparticle surrounded by a metal can also sustain the LSPR around its vicinity. As illustrated in Figure 2.4, a dipole moment establishes when light interacts with a metallic nanoparticle via the complex polarizability α [70]:

$$\alpha = 4\pi r^3 \frac{\varepsilon_m(\omega) - \varepsilon_d}{\varepsilon_m(\omega) + 2\varepsilon_d} \tag{2.3}$$

where, r is the radius of the nanoparticle. Notably, the induced electric field is antiparallel to the applied field. In the case of a metallic void, a dipole moment will be similarly induced, and the polarizability α' can be found by simply switching $\varepsilon_m(\omega)$ and ε_d in the above equation:

$$\alpha' = 4\pi r^3 \frac{\varepsilon_d - \varepsilon_m(\omega)}{\varepsilon_d + 2\varepsilon_m(\omega)} \tag{2.4}$$

Therefore, the induced electric field in a metallic nanovoid is in a totally reversed orientation to that in the metallic nanoparticle.

2.3.2 Periodically arranged nanoholes in thin metal film

As mentioned in the above section, a single dielectric nanohole in a thin metal film behaves similarly to typical nanoparticles concerning LSPR excitation. However, the most fundamental difference between surface-based nanoholes and nanoparticles is that the localized SPs formed around the nanoholes are able to decay along the surrounding metal surface into SPPs. If we arrange the nanoholes in a periodic format, the structure will then act as a two-dimensional grating, in which case the incidence light will be diffracted and provide additional momentum components [71], [72]. In contrast to SPR setup with a holeless flat metal film, this additional

momentum enables the SPP excitation at normal light incidence from the same side (opposed to the reflectance configuration applied in SPR sensing).

Acting as a grating, periodic nanohole arrays can couple light in the close vicinity around the rims of the voids, as shown in Figure 2.6 [73], and provide equivalent sensing capabilities to those of conventional grating-coupled SPR. For instance, Brolo et al. [74] demonstrated a bulk sensitivity of 400 nm/RIU for arrays of nanohole structures on a thin gold film, which is comparable to other grating-based SPR devices. Im et al. [75] further reported that within 50 nm from the surface for 200 nm thick metallic nanohole arrays, no essential decrease was observed in the sensor's sensitivity to bulk refractive index changes. This excellent equivalence of sensing capability results from the enhanced light transmission through periodically arranged metallic nanohole arrays, which is the renowned optical phenomenon – extraordinary optical transmission.
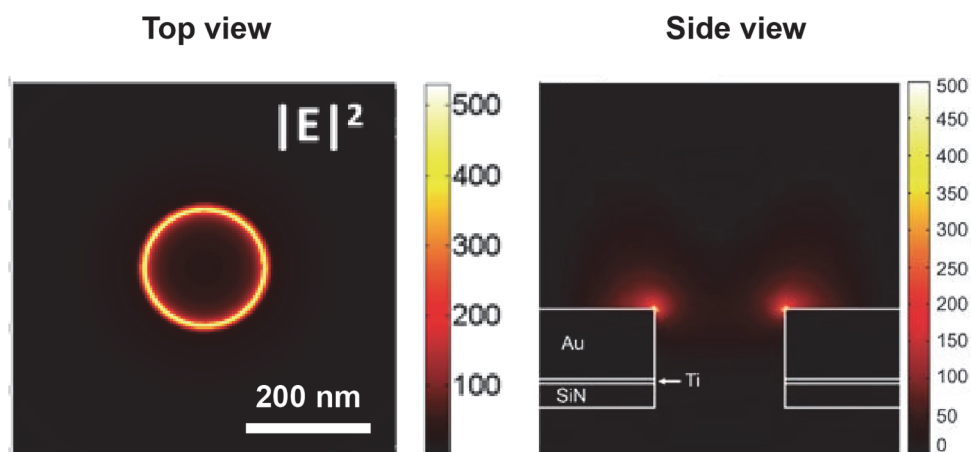
Figure 2.6. Distribution of the electric field around a gold nanohole arranged in an array format. The holes have a diameter of 200 nm and a period of 600 nm. $|E|^2$ represents the field intensity calculated by FDTD simulation. Image adapted from [73].

Extraordinary optical transmission

First described by Ebbesen et al. in 1998 [76], the light transmission through subwavelength apertures was massively enhanced when cylindrical apertures were periodically ordered in a broad array format, overcoming a fundamental constraint normally faced in manipulating light. In particular, such an array displayed unusual zero-order collinear transmission spectra at wavelengths larger than the array period, beyond which no light diffraction occurs (Figure 2.7). Further experiments confirmed that the unique properties are results of the light coupling with surface plasmons on the perforated metal film. As predicted by the authors, in the following 20 years, this finding of "Extraordinary optical transmission" – commonly referred as EOT – has sparked numerous applications in novel photonic devices, especially label-free biosensors.
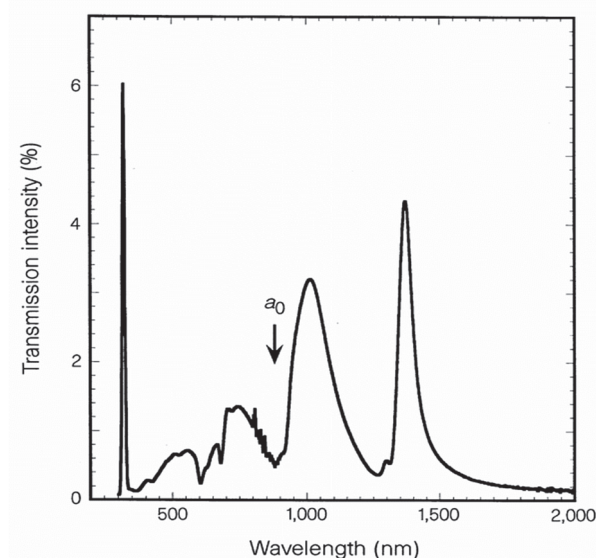
Figure 2.7. Zero-order transmission spectrum of a silver-based nanohole array. The holes have a diameter of 150 nm with a spacing of 0.9 μm in a 200 nm thick Ag film. Image adapted from [76].

Similarly, EOT-based nanohole arrays are mostly exploited as refractive index biosensors. The EOT spectrum displays a characteristic resonance observed at a specific wavelength, λ_{res}, represented by [77]:

$$\lambda_{\text{res}} = \frac{p}{\sqrt{i^2 + j^2}} \sqrt{\frac{\varepsilon_d \varepsilon_m}{\varepsilon_d + \varepsilon_m}} \tag{2.5}$$

where p is the periodicity of the nanoholes, and i and j are the grating orders. It is clear to see that the period of nanoholes influences directly the resonance wavelength: larger periodicity will increase the wavelength of resonance peaks at different grating orders, including the ones residing at the metal-dielectric interface where detection events take place (Figure 2.8) [74], [78], [79]. Meanwhile, deposition of biomolecules on the sensor surface increases the local refractive index (the dielectric constant ε_d), thus leading to increased resonance wavelength in a proportional manner. This establishes the principle for nanohole arrays in thin metal film (usually gold) to be employed as label-free plasmonic biosensors.
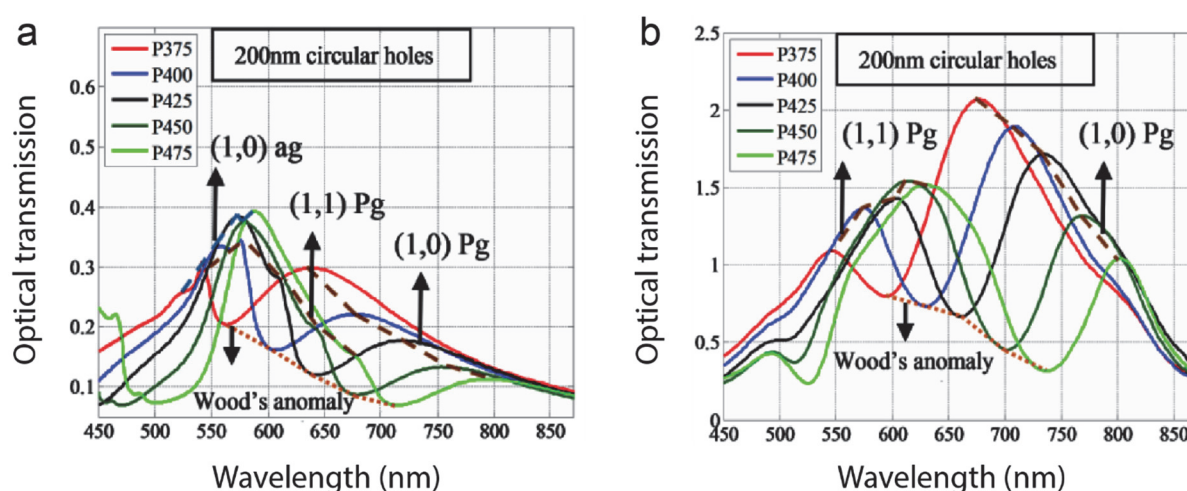
Figure 2.8. EOT spectra of plasmonic nanohole arrays with various hole periodicities. Circular nanohole arrays are fabricated on a 100 nm-thick gold flim which adheres to Pyrex substrate. Transmission spectra of arrays with various periodicities were measurmed both from numerial simulation (a) and experiments (b) in air. Here, 'ag' represents the peak at air-gold interface, while 'Pg' represents the peaks from Pyrex-gold side. Image reproduced from [79].

2.3.3   Structural parameters tailor the optical properties of nanohole arrays

Besides the apparent influence from periodicity (p) on nanoholes' optical transmission as shown in Equation (2.5), other geometrical factors also have significant impacts on the optical characteristics of plasmonic nanohole arrays. Here, the impacts of hole diameter, the thickness of plasmonic metal film as well as the intermediate layer between metal (e.g., Au) and substrate (e.g., glass) are discussed.

Effect of the metal thickness

Above 100 nm, a gold film is considered to be optically opaque and thick. The light transmission can be enhanced by perforating the film with periodic subwavelength nanoholes, which excite surface plasmons and result in EOT phenomenon. The resonance peak manifested in EOT spectrum shifts according to the change of refractive index of the surrounding dielectric medium, providing a RI-based sensing mechanism. As above-mentioned, nanohole arrays exhibit modes of both excited SPP (resulting in the so-called Wood's anomalies, WA) and LSPR. SPP and the associated WA are primarily dependent on the material of metals and the lateral geometry of the grating structures. As shown in Figure 2.9, the first peak in the spectra barely shifts when the film thickness varies while the hole diameter and periodicity remaining constant [80]. However, the wavelength and peak intensity of the second maxima in longer wavelength decrease with a thickening gold film. As the film thickness has a dominant impact on the coupling of excited LSPR mode at the front and back sides of the film, this phenomenon demonstrates how the LSPR coupling, or the film thickness influences the transmission spectrum.

Thickness (nm)	Peak 1	Peak 2
425	666	877
375	652	877
325	652	877
275	652	877
225	660	903
175	660	920
125	660	930
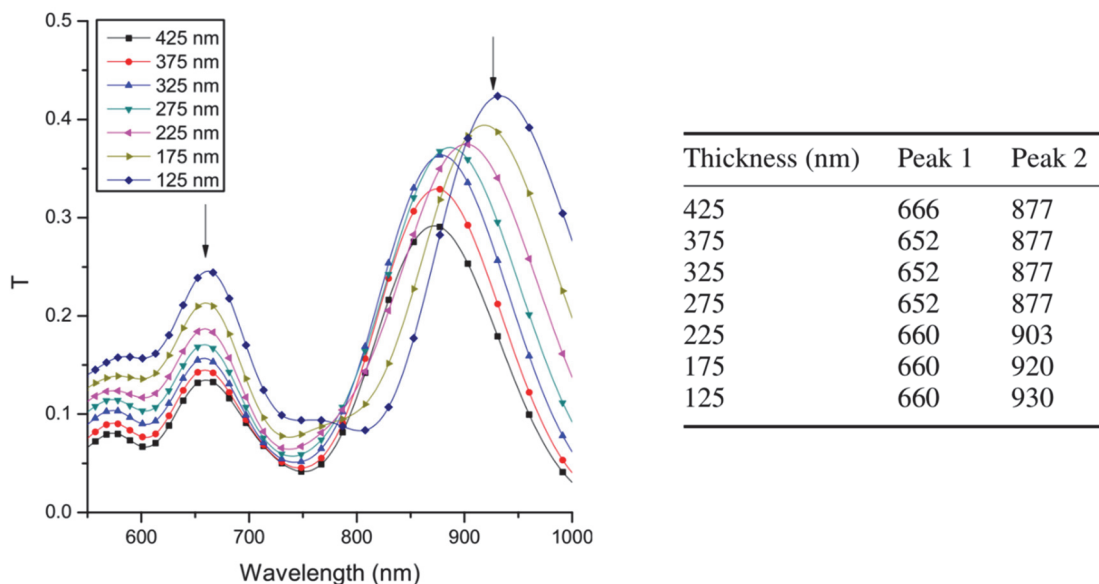
Figure 2.9. Transmission spectra of nanohole arrays on thick gold film as a function of gold film thickness. The diameter of the nanoholes is fixed at 200 nm, and center-to-center spacing is 1400 nm. Images reproduced from [80].

A gold film below 100 nm is semi-transparent in the visible to near-infrared wavelength range, therefore optically thin. The excitation of surface plasmons mediated by periodic nanoholes on thin gold film suppresses the light transmission compared to planar thin gold film, resulting in extinction, or a dip in the transmission spectrum (Figure 2.10). Likewise, the spectral position of the dip is also associated with the ambient RI, enabling nanohole array on thin film to be used for RI-based sensing [81], [82].
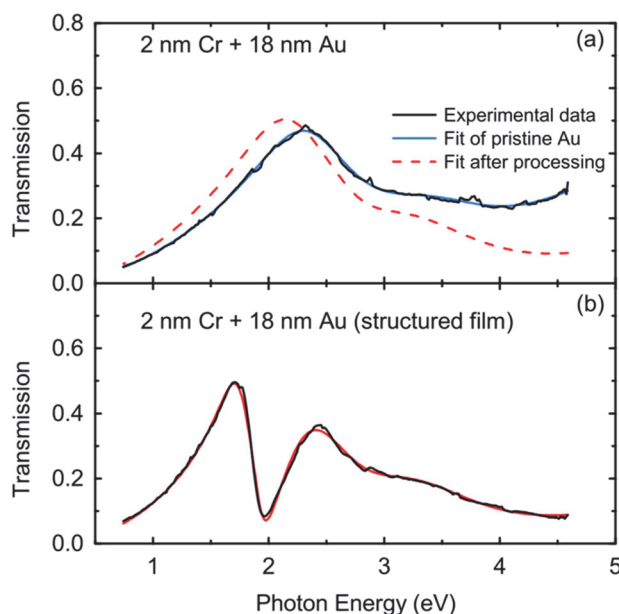
Figure 2.10. Transmission spectrum of nanohole arrays on thin gold film at normal incidence. The transmission spectrum is fitted using dielectric constants of gold and one additional Lorentz oscillator. The transmission spectrum of a planar Au film is shown in (a), and that of nanohole arrays in (b). The Correlation between photon energy (eV) and the wavelength is approximately: $E(eV) = 1.2398/\lambda(\mu m)$. Image reprinted from [81].

Effect of the hole diameter

The hole diameter seems to have negligible effect on the resonance response according to equation (2.5), as long as the periodicity is constant. However, the size variation of nanoholes indeed influences the transmission spectrum as reported by Hajiaboli et al. Larger nanoholes redshift and intensify the second peak (Figure 2.11) while the position of peak 1 barely changes [80]. Similar to peak 1 in Figure 2.9, the first peak here is also dominantly shaped by excited SPP and WAs at the gold surface. However, as the diameter enlarges, the filling factor

of the holes increases, resulting in stronger and easier in-coupling of lower energy photons to the film, namely enhanced LSPR excitations. The stronger LSPR excitations in turn enhance out-coupling of the electromagnetic field, displaying the intensified and red-shifted second peak. However, the diameters of nanoholes should always be in the subwavelength range in order to avoid direct light propagation mode and not act as waveguide channels. For instance, light transmission will become low and insufficient with hole diameters smaller than 200 nm or be distorted with holes larger than 300 nm [83].
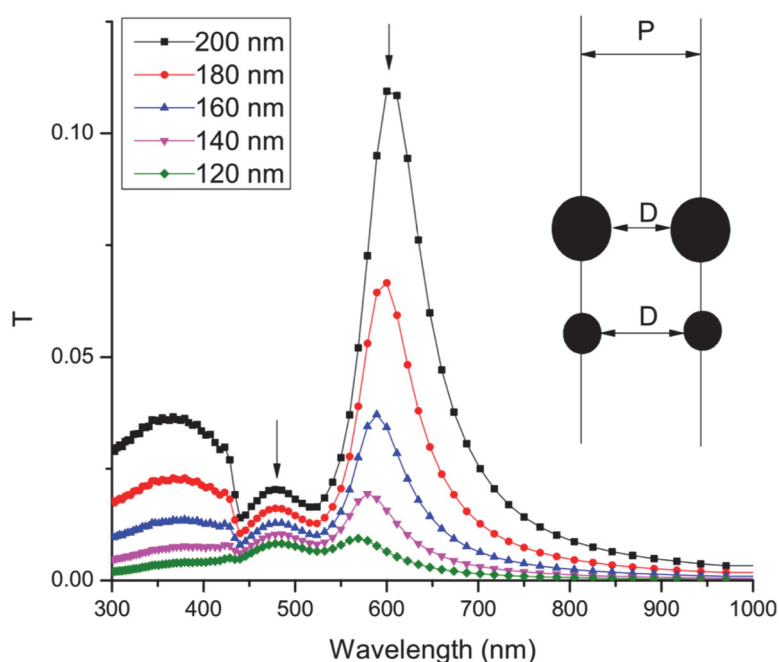
Figure 2.11. Transmission spectra of the nanohole arrays as a function of hole diameters. Gold film thickness is 425 nm, and periodicity of the holes is 1000 nm. Image reprinted from [80].

Effect of the intermediate layer between metal and substrate

Gold has been the popular choice of metal layer for plasmonic nanohole arrays as well as other plasmonic biosensors due to its high optical resonance transmission and exceptional chemical property (e.g., anti-oxidation and straightforward chemical modification). But the affinity of gold to common substrate materials, such as Si and SiO_2, is relatively low. Delamination of the metal layer happens during the fabrication process, thus disabling the robust sensor assembly.

An intermediate layer is usually added between gold and the substrate to enable stable adhesion of the metal film. Among various materials, chromium (Cr) and titanium (Ti) are often employed due to their higher affinity to Si or SiO_2. However, Cr and Ti have higher optical absorption than Au, resulting in lower light transmission efficiency and broadening the resonance band. Therefore, the thickness of the adhesion layer is mostly limited at ~5 nm to ensure sufficient EOT signal and detection sensitivity [84].

Nevertheless, the adhesion layer exhibit limited capability to suppress additional excitation modes that would complicate the sensing capability. As shown in Figure 2.12, a typical transmission spectrum of gold nanohole arrays on transparent glass substrate exhibits multiple excitation modes, including the one excited at the interface between Au and surrounding dielectric medium (1,0), and two at the interface between Au and underlying glass substrates (1,0) and (1,1) [85]. With the mode of Au/Medium (1,0) being the main role in biodetection, the spectral shifting coincides with a significant declining of the peak intensity, which severely impairs a stable and reliable readout for sensitive sensing.

To overcome this disrupting effect of metallic adhesion layer, dielectric materials have been studies as alternatives due to their relatively higher refractive indices and lower absorption of electromagnetic energy. Cetin et al. added an additional layer of 70 nm silicon nitride between
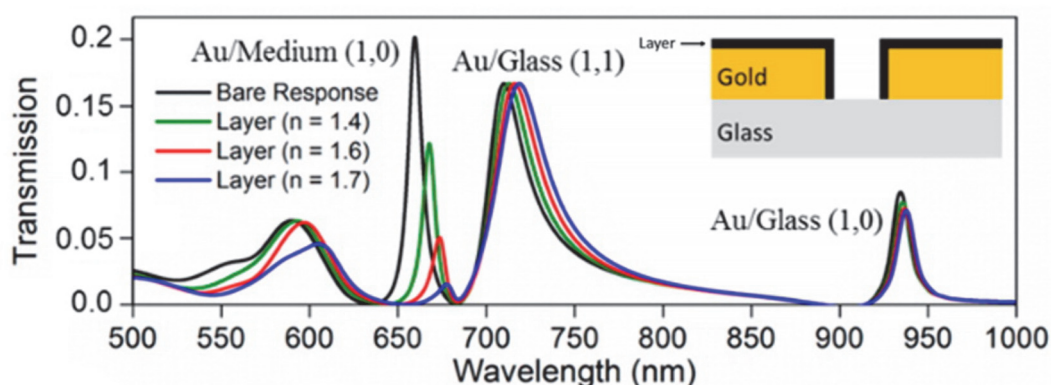
Figure 2.12. Calculated transmission spectrum of gold nanohole arrays on glass (fused silica, n = 1.42). Variation of refractive indices of the dielectric medium is represented by covering the gold surface with an 8 nm-thick dielectric layer of different refractive indices 1.4, 1.6 and 1.7. Nanohole array parameters used in the simulations are: hole diameter 200 nm, array periodicity 600 nm, thicknesses of the gold film 120 nm. Image reproduced from [85].

gold and glass to eliminate multiple modes, leaving solely the functional Au/Medium (1,0) mode in the transmission spectrum [85]. Moreover, the amplitude fluctuations of this mode have also been reduced, which enables larger spectral shifts upon analyte capturing and easy real-time spectral analysis for reliable label-free biodetection (Figure 2.13a). Colas et al. further studied the near-field and far-field optical properties of gold nanocylinders on glass substrate with different adhesion layers, especially for surface-enhanced Raman scattering (SERS) measurements [86]. It has been shown that (3-mercaptopropyl) trimethoxysilane, MPTMS results in the highest field enhancement than Ti, Cr and their corresponding oxides (Figure 2.13b).
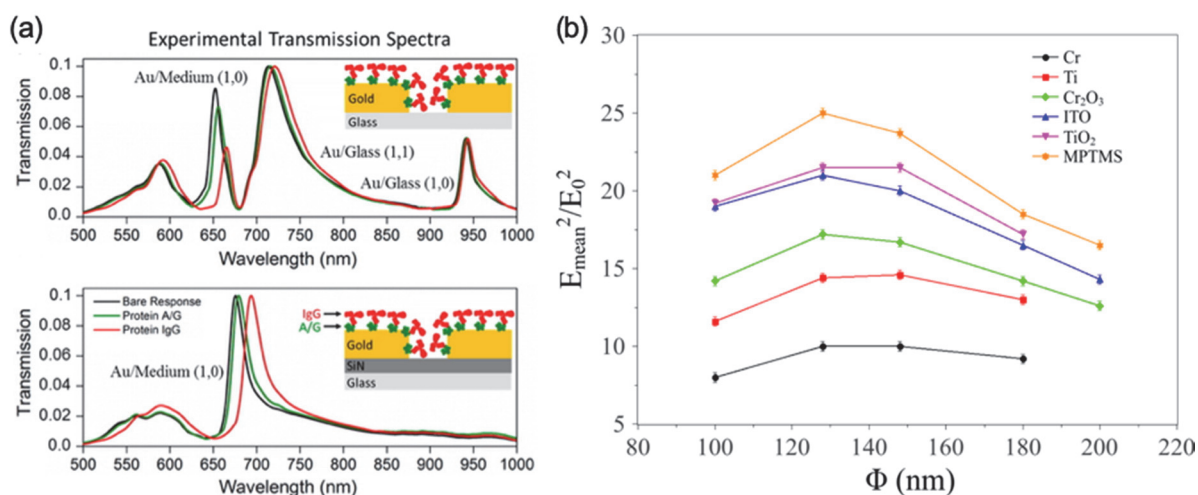
Figure 2.13. Effect of dielectric adhesion layer on the spectral response of plasmonic biosensors. (a) Transmission spectra of the gold nanohole arrays on glass with different adhesion layer compositions, where the gold surface is coated with proteins A/G and IgG antibodies. Nanohole diameter is 200 nm, the periodicity is 600 nm, and the thickness of gold and silicon nitride is 120 and 70 nm. Image reprinted from [85]. (b) Field enhancement of gold nanocylinders on different adhesion layers for SERS measurement as a function of cylinder diameters. Image reprinted from [86].

2.4 Overview of label-free plasmonic biosensors for cell-based analysis

2.4.1 SPR and LSPR biosensors

Label-free optical biosensors, vastly represented by SPR detectors, have established outstanding detection contributions, including those for a broad range of analytes (nucleic acids, proteins, bacteria and cells), and biomolecular interactions (drug–receptor, protein–ligand, protein–cell) [87]. By varying the surface coatings on biosensors, the fast recognition and capturing can be achieved over numerous analytes, although the molecular size and analyte-probe binding affinity play a critical role over the detection sensitivities [88]. However, the real-time detection scenario allows SPR-based optical biosensors to be ideal for the investigation of molecular binding kinetics, as well as the dynamics of live cell-related activities.

Stybayeva et al. integrated an enrichment flow chamber for CD4 T cells from human blood with an SPR detection module to investigate the secretion of interferon-γ without any label [89]. The subpopulation of CD4 T cells were preselected from complex red blood cell-depleted human blood on a glass surface patterned with CD4 antibodies. Culture media conditioned with activated T cells were circulated over the SPR chip so that the binding event of interferon-γ can be directly detected (Figure 2.14a). The modular configuration of the above cell-based analysis has inevitably involved temporal delay during the circulation of analytes to the biosensor. Therefore, Liu et al. incorporated the culturing of live cells directly with SPR sensor chip (Figure 2.14b) for real-time cell secretion analysis [90]. Milgram et al. adopted a similar strategy (Figure 2.14c) to monitor secretion of antibodies from hybridoma cells by using an SPR imaging setup [91]. Apart from secretion analysis, SPR configurations have also been applied to analyze other cell-based functionalities, such as molecular affinities between certain ligands and cell membrane receptors. Broader overview of advances on SPR techniques for cell-based analysis has been discussed and summarized by Nguyen et al. [92] and Abadian et al. [93].
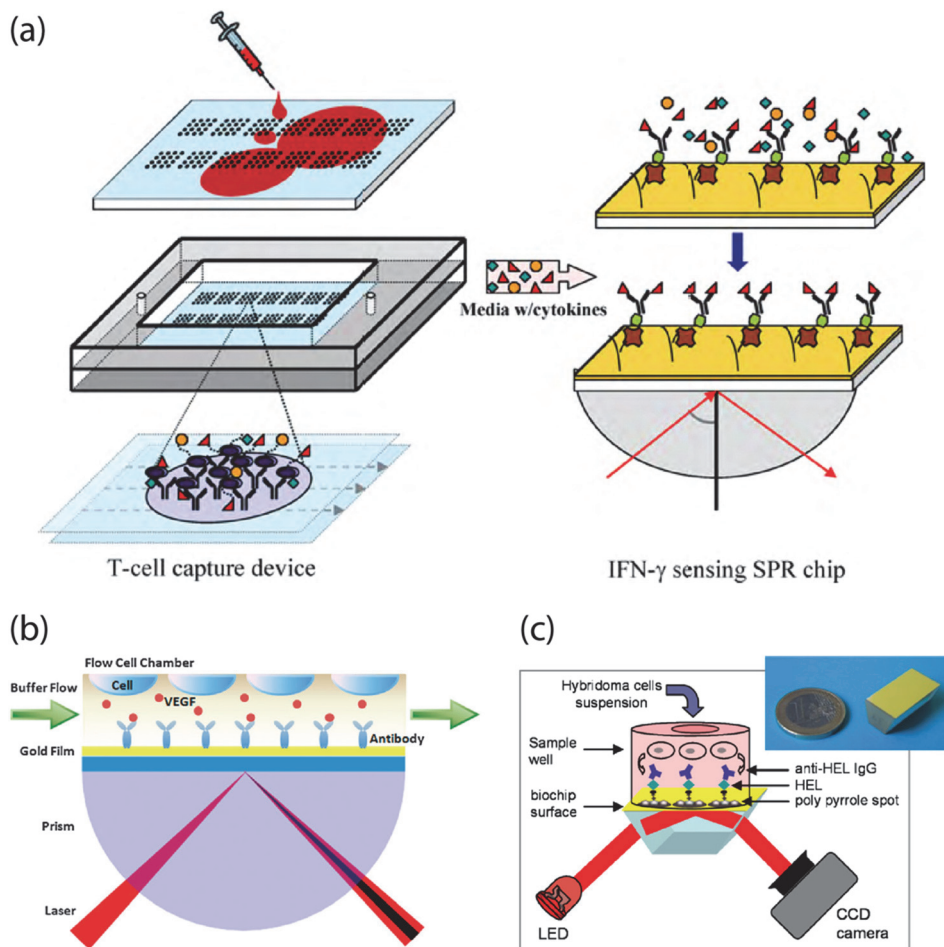
Figure 2.14. Representative cell-based studies with SPR setups. Images reprinted from [89], [90] and [91].

Plamonic biosensors based on localized SPR principle, namely nanoplasmonic biosensors, have been arising as a versatile platform for label-free detection. Owing to their easy tunability of spectral properties and flexible compatibility with lab-on-a-chip formats, nanoplamonic biosensors have drawn increasing attention in cell analysis and clinical diagnosis.

Raphael et al. mapped antibody secretions from single hybridoma cells using arrayed gold nanostructures as LSPR sensing units [94]. As shown in Figure 2.15a, the antigen molecules (in this study, c-myc) that are specific to secreted antibodies were immobilized on the sensing structures. Antibodies are detected when they bind to c-myc coated plasmonic nanostructures. The binding events not only induce a spectral shift, but also a corresponding increase in

scattering intensity. The intensity variations offer an extra advantage for the biosensor to be analyzed with intensity signatures which can be readily integrated into multiplexed and high-throughput recording format. Moreover, signals obtained from sensor units situating at different distances from the cell-of-interest allow for spatial profiling of the antibody distribution and diffusion (Figure 2.15b).
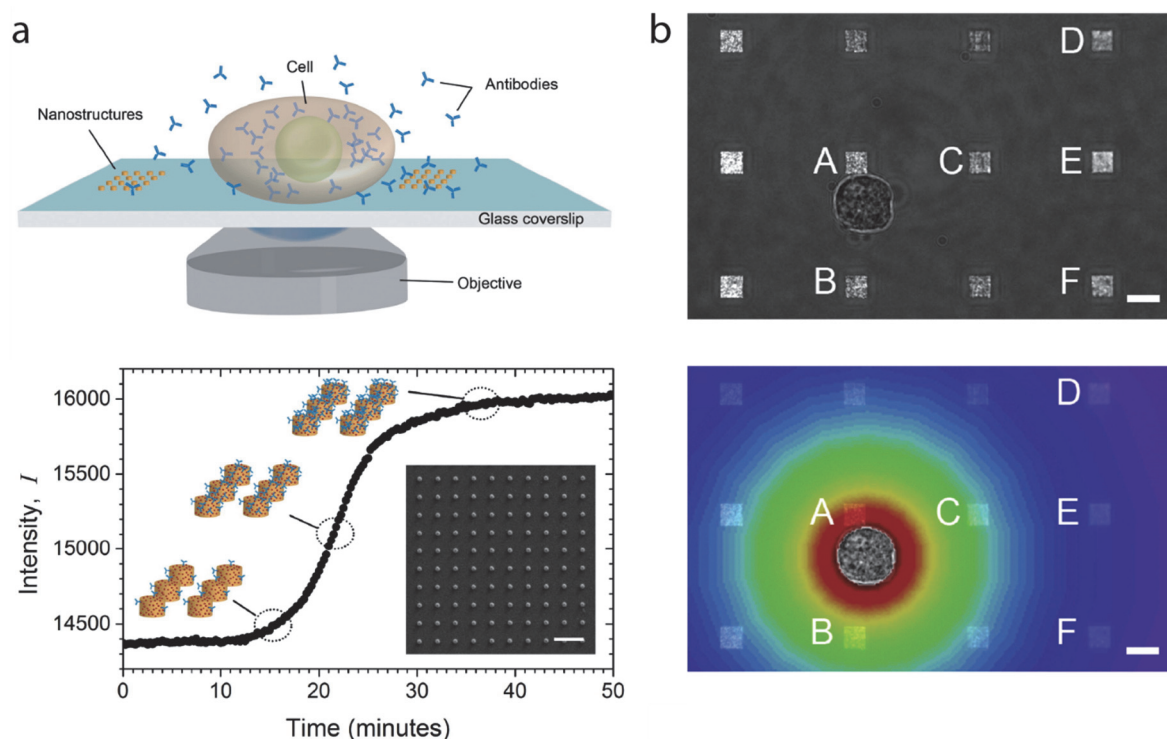
Figure 2.15. Studies of antibody production from hybridoma cells by LSPR biosensor. Images adapted from [94].

Later, Oh et al. reported a remarkable application of nanoplasmonic optofluidic biosensor for the detection of cell-secreted tumor necrosis factor-α (TNF-α) in lysed human blood samples [95]. The device incorporates a functionalized nanostructured surface (Au nanoparticles coated with TNF-α antibodies) and a microfluidic chamber to spatially confine cells and increase the target protein concentration (Figure 2.16a). In particular, the microfluidic chamber contains arrays of micropillars circling around the sensor surface to trap immune cells and separate them from the sensor to avoid unnecessary signal perturbations (Figure 2.16b). With this optofluidic

device, the authors detected TNF-α secretion from cells as few as 1000 from a minimal blood sample volume of 3 μL, while the total assay time was 3 times shorter than that of ELISA.
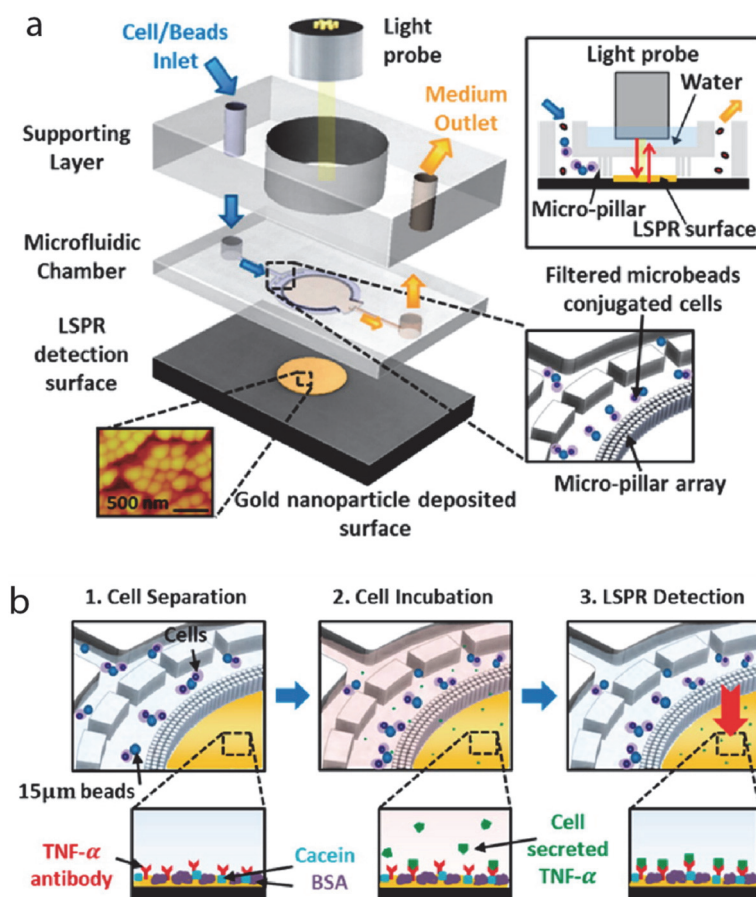
Figure 2.16. Study of cytokine secretion from lysed human blood samples by LSPR biosensor. Images adapted from [95].

2.4.2   Plasmonic nanohole arrays

Plasmonic nanohole arrays have been widely employed as refractive index (RI)-sensitive biosensors. Generally, the sensing performance of RI-based biosensors can be assessed by the bulk refractive index sensitivity and the refractive index resolution. The bulk refractive index sensitivity is defined as the ratio of $\Delta\lambda/\Delta RI$, denoting the spectral shift of the EOT peak per unit change in the refractive index of the surrounding medium. Typically, it is measured by

changing the refractive index over the sensor surface (e.g., injecting salt solutions of varying concentrations) and recording the corresponding spectral shifts of the resonance peak. Although this parameter cannot represent the ultimate sensitivity for biomolecular detection, it is a convenient way to assess the potential detection performance of the biosensor. On the other hand, the refractive index resolution determines the minimum ΔRI that the sensor can distinguish, which correlates more closely to the potential limit of detection (LoD). The performance of some representative studies is summarized in Table 2.1 [96]. In this table, the nanostructure shape is given as solid-based circular hole (Cir), free-standing circular hole (Cir FS), or solid-based elliptical hole (Ellip). Geometrical parameters are given as hole diameter (d) and center-to-center periodicity (p). The type and thickness (Th.) of the metallic substrate (Sub) are provided as well. When available, the bulk refractive index sensitivity and resonance wavelength in air (λ) are given. The sensor resolution is provided either in terms of the refractive index unit or the LoD of real type analytes.

Despite the numerous applications of plasmonic nanohole arrays for biomolecular detections, the implementation of such biosensor for direct live cell analysis is still in its infancy. Tu et al. reported an interesting study to monitor the dynamics of cell attachment by using plasmonic nanohole arrays [97]. By adhering to the sensor surface, the distance between the bottom of cells and plasmonic surface decreases, inducing a noticeable spectral shift. The heterogeneity of cell attachment kinetics among hundreds of single cells has also been profiled by integrating the biosensor with single-cell isolation microfluidics. The analysis and profiling of cell attachment reveal one aspect among various heterogeneous single-cell activities. Nonetheless, it is of greater interest and impact to monitor the biochemical cellular processes, such as cytokine secretions, which will provide significant insights for understanding cell functionalities and promoting pharmaceutical development. Romanuik et al. advanced the application of plasmonic nanohole arrays for cell-based analysis by detecting the antibody secretion from live hybridoma cells [98]. Cells were trapped in a custom-made PDMS chamber which was sealed by functionalized gold nanohole arrays on top. Although there was no pre-treatment and molecular labeling employed, the readout of relevant spectral shifts has been performed in an ELISA-like endpoint manner. There is still a need to explore the advantage of

nanohole arrays as plasmonic biosensor for label-free and real-time detection, especially for cell-based analysis.

Table 2.1. Representative applications of plasmonic nanohole arrays as a label-free biosensor.

Ref	Holes	d (nm)	p (nm)	Th. (nm)	Sub	λ (nm)	Bulk RI sensitivity	Resolution
[74]	Cir	200	590	100	Au	645	400 nm/RIU	—
[99]	Cir	200	1400	200	Au	1550	1022 nm/RIU	est. $5 \cdot 10^{-6}$ RIU
[100]	Cir	150	450	100	Au	604	333 nm/RIU	—
[101]	Cir	300	1500	150-200	Au	—	1520 nm/RIU	$6.6 \cdot 10^{-5}$ RIU
[102]	Cir	200	380	100	Au	550	16'600 %/RIU	2% BSA[§]
[103]	Cir	150	350	105	Au	—	—	13 nM anti-GST
[104]	Cir	180	419	220	Au	~510	323 nm/RIU	10 nM anti-GST[**]
[105]	Cir	150	520	40	Au	~1000	393 nm/RIU	—
[106]	Cir	150	400	200	Au	680	—	20 nM Strep.[††]
[107]	Cir	150	600	150	Au	825	1800%/RIU	—
[108]	Cir FS	300	500	100	Au	575	324 nm/RIU	—
[109]	Cir FS	220	600	125	Au	679	630 nm/RIU	—
[110]	Cir	180	500	100	Ag	~660	450 nm/RIU	$2 \cdot 10^{-5}$ RIU
[111]	Cir	200	380×420	100	Au	632.8	396 nm/RIU	$6.4 \cdot 10^{-6}$ RIU
[112]	Cir	250	430	100	Au	~570	266-pixel intensity units/RIU	$6 \cdot 10^{-4}$ RIU
[113]	Cir	200	600	100	Au	670	615 nm/RIU	—
[114]	Cir	200	600	100	Au	750	522 nm/RIU	2×10^{-5} RIU
[115]	Ellip	175/80	495	100	Au	655	$1.67 \cdot 10^5$ %/RIU	$6.8 \cdot 10^{-7}$ RIU
[116]	Cir	140	600	100	Au		—	1 pM BSA
[73]	Cir FS	200	600	120	Au	683	621 nm/RIU	3.9 µg/mL IgG[‡‡]

[§] BSA: bovine serum albumin
[**] GST: Glutathione S-Transferase
[††] Strep.: Streptavidin
[‡‡] IgG: Immunoglobulin

[117]	Circ.	200	450	200	Au	610	—	670 aM exosomes
[118]	Circ.	200	550	80	Au	610	1100 nm/RIU	—
[85]	Circ.	200	600	120	Au	660	671 nm/RIU	$2 \cdot 10^{-5}$ RIU
[119]	Circ.	200	400	100	Au	~650	302 nm/RIU	30 ng/mL HER2[§§]
[120]	Circ.	180	700	50	Ag	~650	—	$5 \cdot 10^{-4}$ RIU
[121]	Circ. FS	200	600	120	Au	—	600 nm/RIU	300 CFU/mL CT[***]; 1500 CFU/mL NG[†††]
[122]	Circ. FS	200	600	120	Au	—	—	145 pg/mL VEFG[‡‡‡]
[123]	Circ.	200	600	120	Au	—	~631 nm/RIU	50 pg/mL IL-2[§§§]

[§§] HER2: human epidermal growth factor receptor 2
[***] CT: Chlamydia trachomatis
[†††] NG: Neisseria gonorrhoeae
[‡‡‡] VEGF: vascular endothelial growth factor
[§§§] IL-2: interleukin-2

Chapter 3

Experimental methods and materials

3.1 Spectroscopic imaging setup for EOT measurements

3.1.1 Optical configurations

To facilitate the EOT-based optical measurement, we established a spectroscopic imaging setup based on a microscope commonly implemented in biological laboratories (Figure 3.1a). In brief, a spectrometer (Shamrock 303i, Andor, spectral resolution 0.1 nm) and a deep-cooled CCD camera (iKon-M, Andor) are mounted on an inverted microscope (Nikon Ti-U). A schematic illustration of the optical path for the biosensor analysis is shown in Figure 3.1b. A broadband light source illuminates the plasmonic chip at normal incidence. The EOT signals are collected by the underlying objective lens, entering the subsequent spectrometer through an entrance slit opening. The spectrometer is mounted at one of the side ports on the microscope (Figure 3.1a). Inside the spectrometer, the transmission beam is dispersed via an optical grating, which expands the wavelength elements and results in a 1D spectral image on the camera.
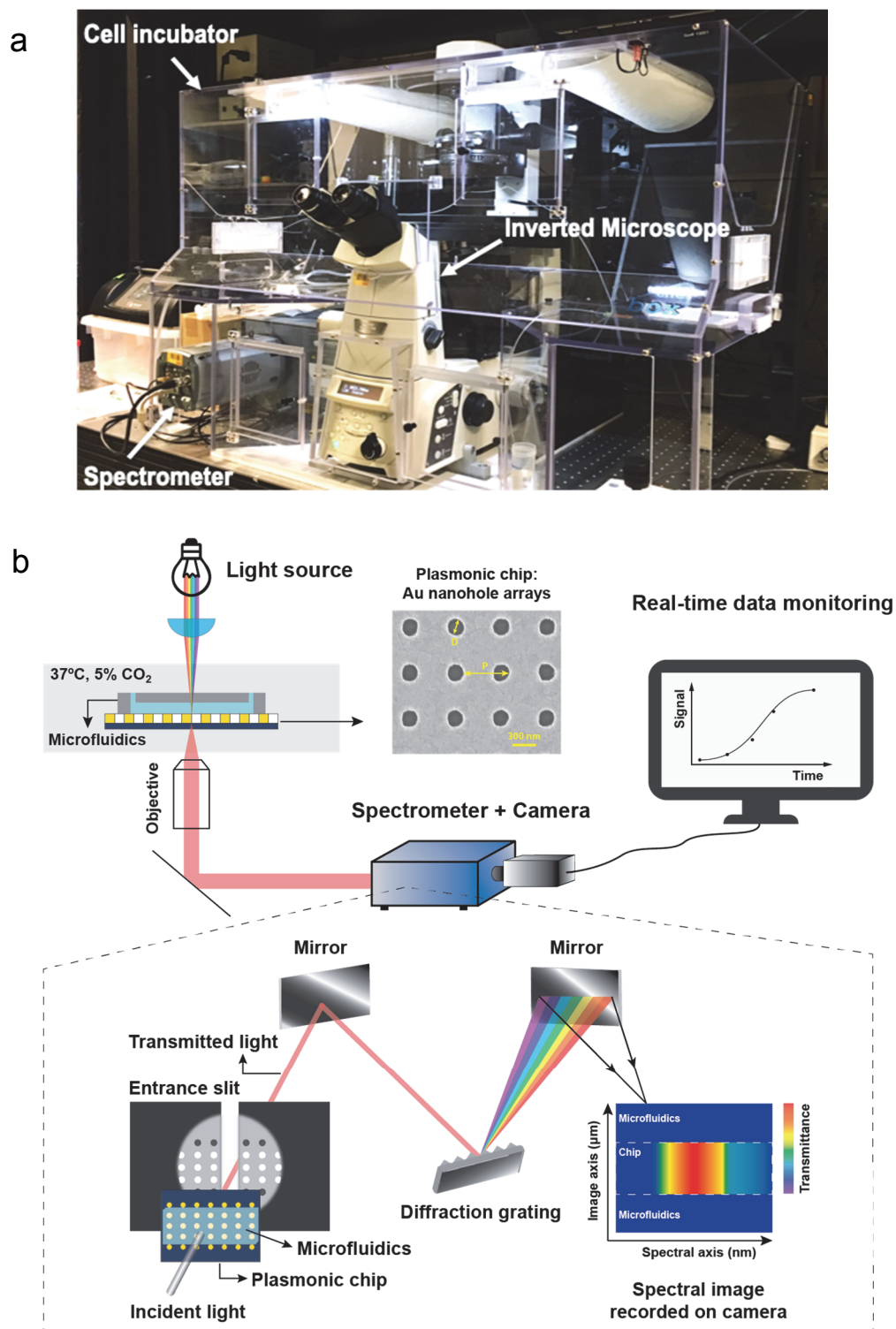
Figure 3.1. Spectroscopic imaging setup for EOT-based optical measurement. (a) A picture of the modified microscope system for real-time live cell analysis. (b) Schematic illustration of the optical configuration.

3.1.2 Image analysis

The spectral images acquired as above contain wavelength information at corresponding positions on the biosensor chip. As seen in Figure 3.2a, EOT spectra from different sensor units (e.g., with different surface coatings) are recorded simultaneously on one image. A specific spectrum can be extracted from each band (Figure 3.2b). To facilitate real-time monitoring of molecular binding, the images are recorded as a function of time, from which the EOT peaks are immediately extracted from corresponding spectra and plotted at the same time by a
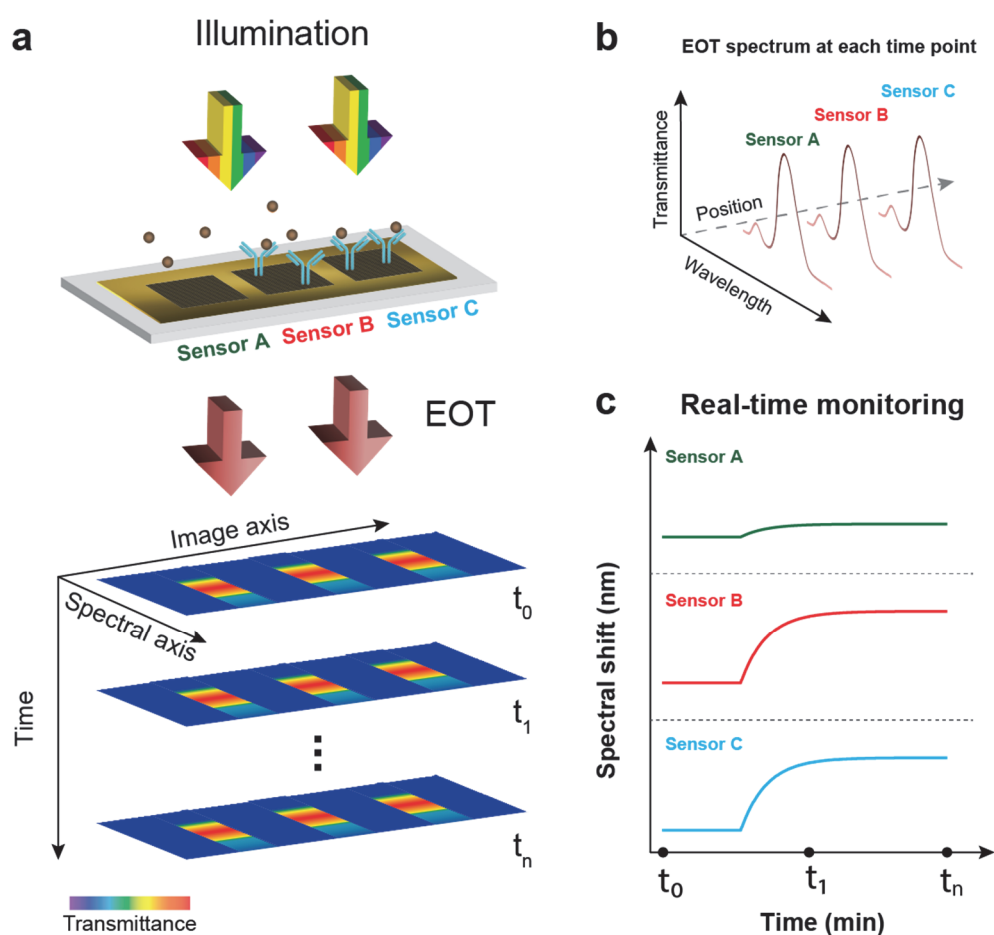
Figure 3.2. Principle of real-time image analysis for plasmonic nanohole arrays. (a) Schematic drawing of the light illumination over sensor arrays and the resulting spectral images recorded sequentially over time by the imaging set-up described in 3.1.1. (b) Spectral curves can be extracted from any region of interest designated on the image at each time point. The EOT peaks are clearly shown on the curves. (c) By tracking the evolution of EOT peaks over time, the real-time monitoring of molecular binding is thus achieved. Signal differentiation reveals the different surface functionalization on the sensor arrays.

custom-made MATLAB script. By tracking the peak shifts over time (from t_0 to t_n), a real-time binding curve, namely sensorgram, can thus be derived which reveals the capturing of molecules of interest at different sensor units. For example, as shown in Figure 3.2c, subtle binding signal is presented from sensor A due to the lack of specific antibody functionalization, whereas sensor B and C show clear analyte bindings.

3.2 Fabrication of plasmonic nanohole arrays

3.2.1 Free-standing nanohole arrays

The first format for plasmonic nanohole arrays was represented by spatially patterned array units on free-standing thin gold film. A lift-off photolithography procedure was established as shown in Figure 3.3a. A 500 μm-thick silicon wafer is selected as the sensor chip substrate, with both sides coated with 100 nm-thick silicon nitride (SiN_x) films. The nanohole structures were first patterned
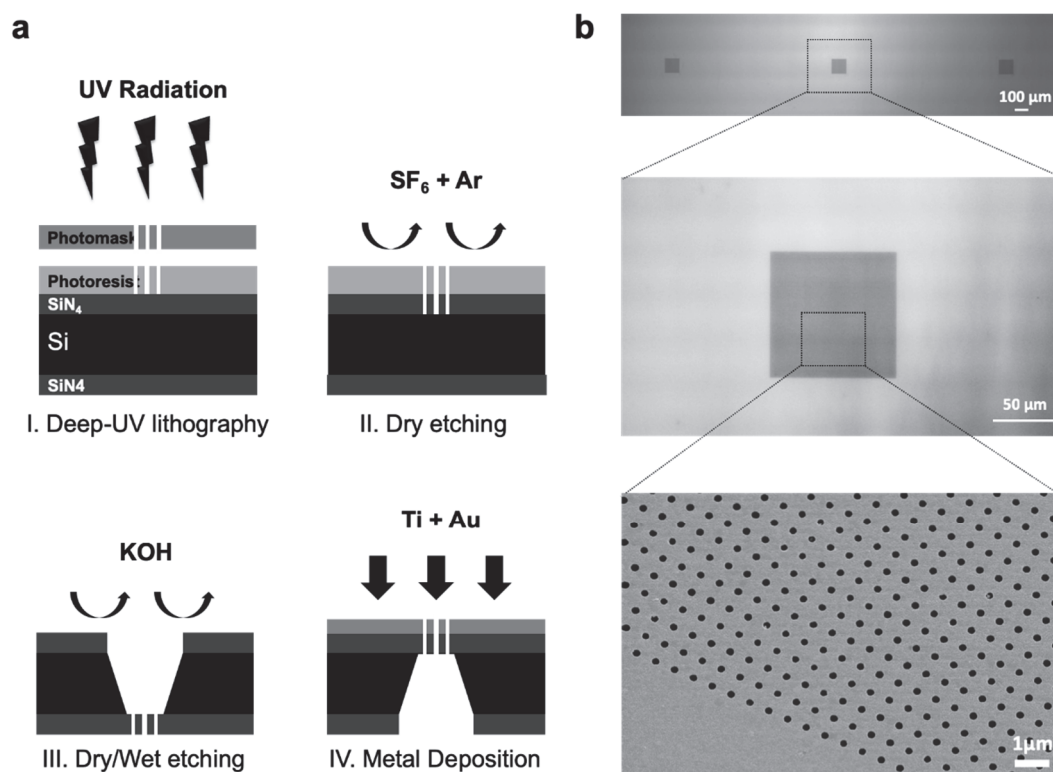
Figure 3.3. Nanohole arrays on free-standing membrane. (a) The fabrication process of the gold nanohole arrays on free-standing silicon nitride membrane. (b) The optical image on the top panel showed the layout of the three in-line nanohole arrays, with each array measuring 100×100 μm as shown in the middle panel. The nanohole structures on the membrane were shown in the zoomed SEM image.

on photoresist layer on top of SiN_x by UV lithography fulfilled with a stepper (ASML S500/300 DUV). The photoresist was then developed and nanoholes were further etched through the SiN_x film on the same side by SF_6/Ar plasma treatment. Likewise, the SiN_x on the backside of the wafer was removed, and free-standing SiN_x membranes was ultimately generated by KOH wet etching. Finally, a 5 nm thick Ti adhesion layer followed by a 120 nm thick Au sensor layer were evaporated. The resulting sensor units measures 100×100 μm^2, and with a center-to-center separation of 1 mm. Each nanohole has a diameter of 200 nm and a period of 600 nm (Figure 3.3b).

3.2.2   Solid-based nanohole arrays

A large-scale fabrication scheme is necessary to provide a cost-effective and robust sensor chip supply. The above nanohole structures sitting on free-standing membranes require a multi-step fabrication process and the membrane is very fragile and vulnerable to mechanical deformation. Therefore, a modified fabrication strategy was developed where the nanostructures were eventually produced on solid substrate: a transparent quartz wafer. As shown in Figure 3.4, a cleaned fused silica wafer was firstly coated with 10 nm thick Ti and 120 nm thick Au by an e-beam evaporator (Alliance Concept EVA 760). Besides enabling the Au adhesion on silica, the Ti layer also suppresses the irrelevant SPP mode at the Au/glass interface. The nanohole arrays with the same
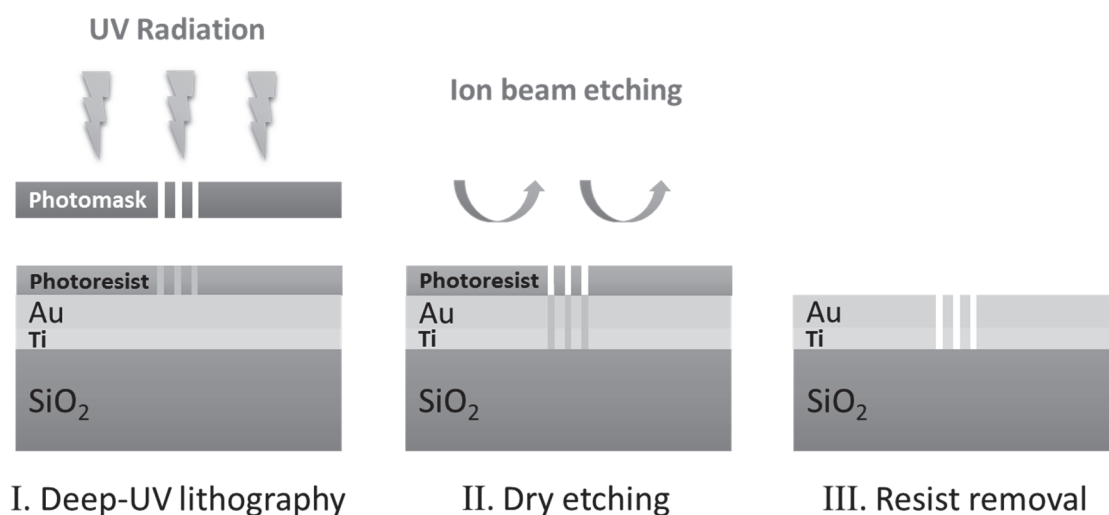
Figure 3.4. The schematic wafer-scale fabrication procedure for plasmonic nanohole arrays.

geometry and layout as above were then patterned using a 248 nm deep-UV stepper (ASML PAS 5500/300 DUV) on the photoresist layer and were transferred into the metal layer by ion beam etching (Oxford Instruments PlasmaLab 300 IBE). With this scheme, the nanoplasmonic structures are fabricated in one step across the whole wafer scale, providing a cost-effective and efficient strategy for bulk production.

3.3   Design and fabrication of the microfluidic devices

Generally, microfluidic devices were fabricated with polydimethylsiloxane (PDMS, SYLGARD® 184 SILICONE ELASTOMER KIT). The PDMS prepolymer was prepared by mixing the elastomer and curing agent in 10:1 weight ratio and degassed for 20 min in the desiccator. Following the degassing, the prepolymer was gently poured onto the passivated mold and cured at 80 °C for at least 4 hours to form the desired structures used. Finally, the molded PDMS layer was released from the wafer and inlets and outlets were punched.

For the study described in Chapter 4, we prepared two microfluidic assemblies: one for the HeLa cell culture (the microfluidic culture module) while the other one for fluidic transportation over the plasmonic biosensor (the optical detection module). The master mold was prepared on a 4-inch Si wafer where the microchannel structures were directly engraved on 50 μm-thick photoresist layer (mr-DWL_40) by maskless laser aligner (Heidelberg MLA150, Germany). Before the PDMS preparation, a silanization process with trimethylchlorosilane (TMCS, 92360, Sigma) in vacuum for 20 min was performed to passivate the mold surface to aid release of PDMS from the mold. As shown in Figure 3.5a, the microfluidic cell chamber was designed in winding channels of 500 μm wide. The total length of the channel is adjustable according to the number of winding units. The chamber used in this study provides a surface area of ~1 cm^2 for cell growth. To assemble this module, the PDMS slab and the glass slide were treated with oxygen plasma cleaner, followed by immediate contact that results in irreversible bonding. For the optofluidic detection module, the sensor microarrays were optically aligned with the corresponding sensor channels embedded in the PDMS slab on an upright microscope.
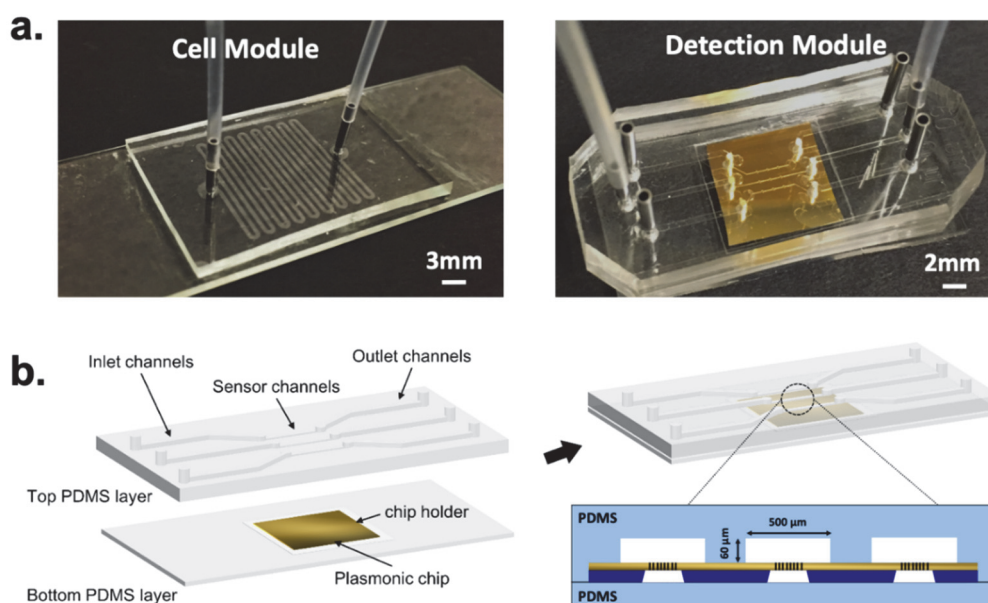
Figure 3.5. The microfluidic modules used in the VEGF study. (a) Pictures of the cell culture module bonded to a glass slide with inlet and outlet connections (left), and the detection module consisting of the plasmonic chip embedded in a microfluidic system (right). (b) Details of the microfluidic detection module.

Each sensor channel measures 60 μm high, 500 μm wide and 5 mm long, resulting in a volume of ~150 nL (Figure 3.5b).

For the study described in Chapter 5, a multifunctional microfluidic device was manufactured with PDMS by using a combination of the membrane sandwich fabrication method and PDMS injection molding technique. Figure 3.6 illustrates a pair of complementary molds that are utilized for the injection molding process.

Molds are fabricated by standard photolithography techniques, as described in the previous work [124]. In brief, SU-8 3050 (MicroChem Corp) is used to pattern the transparent upper borosilicate glass wafer substrate, and lower silicon wafer substrate with protruding features, with a height of 160 and 180 μm respectively. PDMS pre-polymer is introduced between the molds, which are optically aligned and clamped in position under a dissecting microscope. Standoff distance between the molds can be adjusted by changing the spacer material positioned between supporting pillars regularly

positioned across the molds. The clamped mold assembly is cured in an oven at 80 °C for one hour and separated to extract the cured PDMS slab, which is further cut to size and biopsy punched with viaducts providing a pathway between the primary channel and primary channel interface lines. The upper surface is plasma bonded to a 5mm thick blank PDMS interface slab that is previously biopsy punched with 1mm interface holes aligning with the interface areas on the fluidic inlets, outlets, and pneumatic interface areas. Microchannels are patterned on both sides of the injection molded slab, namely the primary channel measuring 500 µm in width for cell culture on the bottom surface, which corresponds to 500 µm-wide fluidic interface lines on the upper surface, pneumatic actuation channels and 300 µm-wide fluidic regulation channels are also patterned on the upper layer. The fluidic interface lines connect through biopsy-punched viaducts to the accessible interface areas, allowing fluidic access to the primary channel on the bottom layer.

The complementary molds are separated by approximately 60 µm during PDMS casting, resulting in a thin PDMS membrane (i.e., the regulation membrane) between the regulation and the primary channels. The detailed fabrication process of the pneumatically controlled valves was described elsewhere in a previous work outlining the simplified method by injection molding [124]. Briefly, the valve gates consist of protruding barriers obstructing fluid flow positioned within the primary channel, directly under the actuation chambers, and forming an isolated channel segment as the incubation chamber. A thin PDMS membrane separates the hexagonal pneumatic actuation chambers and primary channel. When the actuation chambers are evacuated, the valve membranes are deflected upwards, raising the valve gates clear of the primary channel floor and allowing fluid flow across the valves. The regulation channel passes in parallel above the primary channel and follows a serpentine configuration directly over the valve-gated area, readily maintaining the steady state of the isolated volume underneath the membrane.

Figure 3.6. Fabrication and illustration of the multifunctional microfluidics system. (a) The pair of complementary molds for the injection molding process. (b) Assembly of the PDMS microfluidic slabs with the nanohole array chip as the optofluidic biosensor.

3.4 Chemical and biological reagents

3.4.1 Chemical reagents

PEGylated alkanethiol compounds:

- HS-C$_6$EG$_4$OH, HS-C$_{11}$EG$_4$OCH$_2$COOH
- HS-C$_{11}$-EG$_3$-biotin

were purchased from Prochimia Surfaces (Sopot, Poland).

Lipid molecules:

- 1-palmitoyl-2-oleoyl-sn-glycero-3-phosphocholine (POPC)
- 1,2-dioleoyl-sn-glycero-3-phospho-L-serine (DOPS)
- biotinylated 1,2-dioleoyl-sn-glycero-3-phosphoethanolamine (biotin-DOPE)

were obtained from Avanti Polar Lipids Inc. (Alabas-ter, Alabama, USA).

Other reagents for crosslinking and buffer preparation:

- N-(3-imethylaminopropyl)-N'-ethylcarbodiimide hydrochloride (EDC)
- sulfo-N-Hydroxysulfosuccinimide (sulfo-NHS)
- octadechanethiol (ODT)
- octyl glucopyranoside (OG)
- streptavidin
- poly-L-lysine (PLL) solution
- bovine serum albumin (BSA)
- Krebs-Ringer bicarbonate buffer
- MES (2-(N-Morpholino)ethanesulfonic acid hydrate)
- Ethylenediaminetetraacetic acid (EDTA)

were purchased from Sigma-Aldrich (Buchs, Switzerland).

3.4.2 Cell culture related materials

Phosphate saline buffer (PBS), Dulbecco's Modified Eagle Medium (DMEM), Roswell Park Memorial Institute 1640 Medium (RPMI 1640), Penicillin/Streptomycin, fetal bovine serum (FBS), TrypLE™Express for HeLa cell culture, and eBioscience™ Cell Stimulation Cocktail for the EL4 cell culture were purchased from ThermoFisher Scientific (Reinach, Switzerland). Human VEGF ELISA kit and anti-human CD3 antibody was obtained from Abcam (Cambridge, UK). Biotinylated IL-2 antibodies and standard IL-2 proteins were purchased from MABTECH (Sweden). Calcium ionophore A23187 were purchased from Sigma-Aldrich (Buchs, Switzerland). Biotinylated pMHC monomers (HLA-A0201/NY-ESO-1157-165) were obtained from the Tetramer Core Facility (Ludwig Institut for Cancer Research, Lausanne, Switzerland). All other materials were purchased from EPFL chem shop.

3.4.3 Protocols for routine cell culture and cell loading for measurements

For the VEGF secretion study, human cervical cancer cells, HeLa cells were employed. Cells were cultivated in high glucose DMEM supplemented with 10% FBS, 100 units/mL Penicillin and 100μg/mL Streptomycin at 37 °C in humidified 5% CO_2 incubator. The cells were cultured routinely in cell culture flasks (Nunc™ EasYFlask™, surface area of 75 cm^2), harvested and counted based on general protocol. Briefly, cells were rinsed with PBS for 2~3 times to remove the trace of remaining serum proteins

from the medium. Then 5 mL of TrypLE^{TM}Express was added to the flask that was incubated for 2~3 min. Cells detached from the culture flasks are well suspended for counting on a standard hematocytometer glass slide. For seeding into the microfluidic culture chamber, a cell suspension with a density of 10^5 cells/mL was injected into the culture chamber and incubated overnight at 37 °C before the measurement.

For the single-cell IL-2 secretion, mouse lymphoma cells, EL4 cells were cultivated in RPMI 1640 medium supplemented with 10% FBS, 100 units/mL penicillin and 100 μg/mL streptomycin at 37 °C in a humidified 5% CO_2 incubator. The cells were subcultured routinely and counted as mentioned above. For cell harvesting, gentle pipetting suffices as EL4 cells suspend in the culture medium and do not attach to the flask surface. Before cell seeding in the microfluidic channel, the cells were harvested by gentle washing off the culture flask and centrifuged at 1000 rpm for 5 min. The cell density was adjusted to 3×10^4 cells/mL, and the suspension was subsequently injected into the primary channel by actuating the pneumatic valves. Once the injection was finished, the pneumatic control was dismissed, and the cells were enclosed in the isolated valve-gated microchamber. Finally, we achieved 4~5 cells in the isolated valve-gated region, with each cell separated as a single entity for the measurement. The seeded microfluidic assembly was incubated for at least 20 min at 37 °C before the measurement.

For cell affinity experiments, SupT1 cells (CRL-1942, ATCC) were employed. CD8$^+$ SupT1 cells were transduced with different TCR sequences (DM β, V49I, wild-type: WT and T1ϕ: knockout TCR) as described in previous works [125], [126]. Cells were cultured in RPMI 1640 medium supplemented with 10% fetal bovine serum, 100 units/mL penicillin and 100 μg/mL streptomycin at 37 °C in a humidified 5% CO2 incubator. The cells were subcultured routinely and counted based on a general protocol. For the measurements, cells were harvested from the culture flask and medium was exchanged to ice-cold Krebs-EDTA (3 mM) buffer by centrifugation (1000 rpm, 3 min) and resuspension three times. The cell density was adjusted to 10^6 cells/mL and the different cell samples were prepared by serial dilution. After sensor functionalization, 250 μL ice-cold cell samples of different densities ($10^2 - 10^5$ cells/mL) were sequentially injected into the SPR flow cells at flow rate of 10 μL/min for 25 min and rinsed

afterwards for 10 min. Sensorgrams were acquired by monitoring the weighted centroid of the SPR peak in real time, with simultaneous subtraction of the total internal reflection (TIR) angle displacements, which are related to bulk refractive index changes.

3.5 Surface functionalization for label-free biodetection

3.5.1 Self-assembled monolayer

Proper coating of the biorecognition layer is essential for label-free biosensors as it guarantee a reliable and robust quantitative analysis. We adopted the well-established chemistry of sell-assembled monolayer (SAM) for gold-based biosensor surface. SAM consists of amphiphilic molecules that self-organize a tightly ordered matrix on the surface. Due to the naturally robust affinity to gold, most widely applied SAM molecules include thiol group as the anchorage end on gold surface. On the other end of the molecule lies the external functional group that can bind the biorecognition molecules in a covalent manner. This strategy of surface chemistry offers high robustness and stability of the biosensor functionalization. Upon the SAM, we chose monoclonal antibodies to ensure a highly selective and efficient capturing of the target molecules.
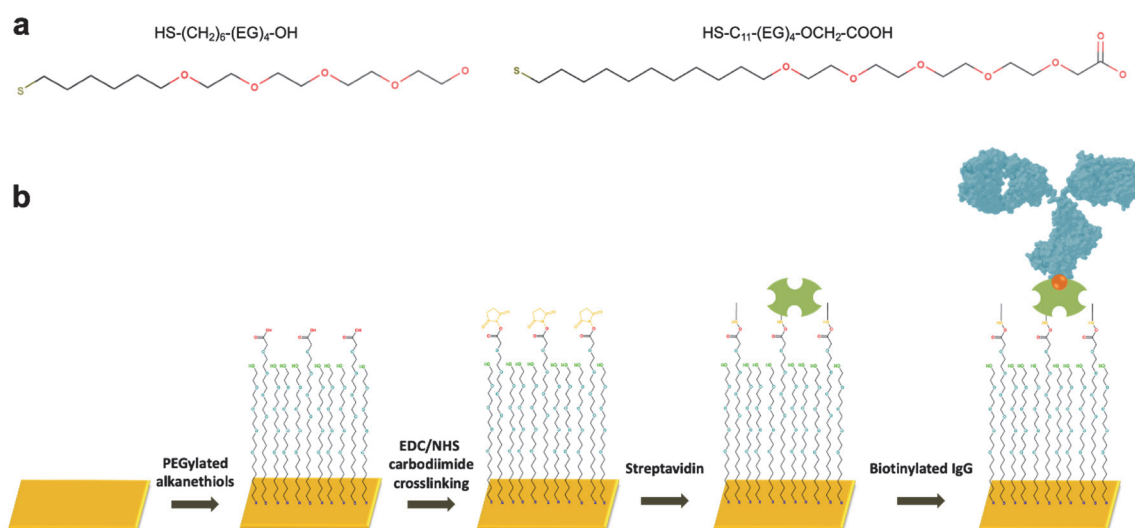
Figure 3.7. Surface functionalization for gold-based plasmonic sensor chips. (a) Structures of the hydroxyl- and carboxyl-ended alkanethiol molecules used for the formation of SAM on gold. (b) Stepwise illustration of the surface functionalization process.

The conventional stepwise biofunctionalization procedure is illustrated in Figure 3.7. Prior to functionalize the chip with antibodies, the gold chip was cleaned by consecutive washes in acetone, ethanol, and MilliQ water, then further treated with a UV-ozone cleaner (Bioforce Nanosciences) for 20 min. The cleaned chip was incubated with a mixture of PEGylated alkanethiols made of $HS-C_6-(EG)_4-OH$ as well as either $HS-C_{11}-(EG)_4-O-CH_2-COOH$ or $HS-C_{11}-EG_3$-biotin (total $[-SH]$ = 1μM, molecular ratio=5:1 for routine molecular detection and 10:1 for cell capturing) in absolute ethanol overnight at room temperature. The carboxylic groups on the chip surface were then activated for tethering proteins by incubating with 100 μL cross-linking solution containing 200 mM EDC and 50 mM sulfo-NHS in 0.1 M MES buffer (pH=4.5) for 15 min at room temperature. Subsequently, the activated chip was ready for the immobilization of biorecognition molecules: the antibodies. Alternatively, in order to orient the antibodies for efficient antigen capturing, the activated chip was first incubated with 100 μg/mL streptavidin solution diluted in PBS for 1 h at room temperature (0.01% PLL was supplemented for the study in Chapter 5 to facilitate cell attachment). Biotinylated antibodies (anti-VEGF or anti-IL-2) were then immobilized on the chip as the biorecognition layer due to the extremely strong streptavidin-biotin bond.

3.5.2 Formation of lipid bilayer for cell affinity study

A supported lipid bilayer (SLB) is traditionally formed by disruption of small unilamellar vesicles (SUVs) on hydrophobic planar surfaces. SUVs were prepared according to the manufacturer's instructions (Avanti Polar Lipids Inc.). Briefly, desired lipid compositions were prepared by mixing the different phospholipids dissolved in chloroform: POPC 90% with either 10% DOPS or 10% biotin-DOPE at 1 mg total mass. Chloroform was gently evaporated under vacuum at room temperature overnight. Lipid precipitate was then dissolved in PBS buffer to 1 mg/mL and the lipid suspension was sonicated for 1 h at room temperature to achieve small liposomes (50-100 nm).

SLB formation was carried out on SiO_2-coated sensor chips with the following flow sequence:
- 1 mg/mL SUVs in PBS buffer for 20 min
- 20 mM NaOH cleaning for 5 min
- BSA in PBS for 20 min.

For the formation of hybrid bilayer membrane (HBM), the Au-sensor chip was modified *ex situ* by immersing in an ethanol solution of ODT at 5 mM overnight at room temperature. After rinsing and drying, the procedure follows the sequence:

- 40 mM OG priming in PBS buffer for 10 min
- 1 mg/mL lipid vesicles in PBS buffer for 20 min
- 20 mM NaOH cleaning for 5 min; BSA in PBS for 20 min.

To immobilize biotinylated-pMHC monomers on lipid bilayer, a layer of streptavidin (100 μg/mL) was first tethered on SLB or HBM, and the monomers (200 nM) were subsequently attached.

3.5.3 Surface multiplexing

The spatially separated nanohole array units on the free-standing membrane format enabled each area to be individually functionalized for possible multiplexed analysis. To achieve this,
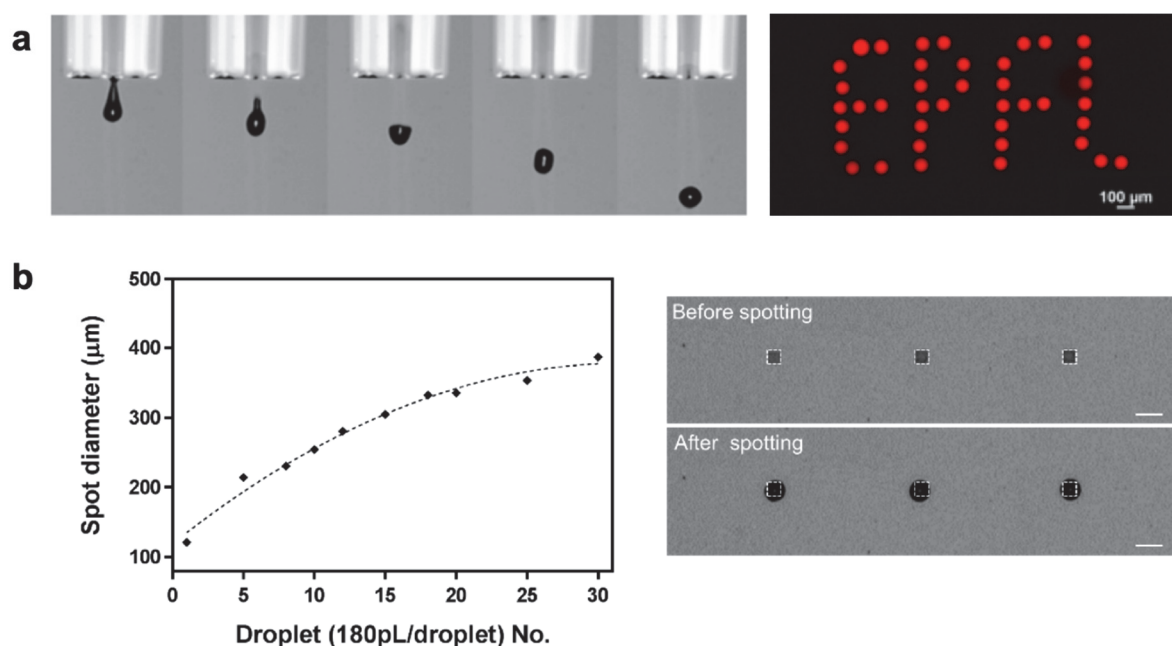
Figure 3.8. Multiplexing the biosensor surface coating by microdispensing technique. (a) A time lapse sequence of a liquid droplet being ejected out of the nozzle (left). On the right is 'EPFL' printed with red-fluorescent proteins on a microscope glass slide. (b)The correlation between droplet number and resulting spot size was shown on the left. On the right, the nanohole array units were highlighted by the white dashed boxes, and they were entirely covered by antibody droplets after the spotting. (Scale bar: 200 μm).

we employed the state-of-the-art micro-spotting technology. The antibody solutions were spotted onto the streptavidin-coated chip using a piezoelectric microdispensing system sciFLEXARRAYER S3 (Scienion Germany, spatial precision < 5 μm). This technique employs a nozzle with microscale opening to dispense liquid droplets of ultralow volume (in the order of picoliters) on planar surfaces in a fast and high-throughput fashion (Figure 3.8a). Due to the minute amount of the liquid droplet during spotting, the antibodies were diluted in PBS solution supplemented with 2% glycerol to prevent liquid evaporation. Meanwhile, the spotting device is equipped with an airtight hood where high humidity (> 65%) was supplied and with a cooling unit to maintain the target stage at low temperature (e.g. 10-15 °C). The correlation between droplet number and the resulting spot size was shown in Figure 3.8b. To fully cover the sensor surface, the droplet size was tuned to reach ~180 pL and 5 droplets were deposited on each sensor unit. The chip was incubated at 4 °C overnight following the spotting to allow stable immobilization of biotinylated antibodies on streptavidin layer. The chip was subsequently blocked with complete cell culture media prior to the detection.

3.6   Surface plasmon resonance instrumentation

3.6.1   General configuration

For the proof-of-concept study of anti-tumor cell affinity, we employed a commercial multi-parametric SPR setup (MP-SPR Navi 210A VASA, Bionavis Ltd, Tampere, Finland) equipped with lasers of 3 different wavelengths (670 nm, 785 nm, 980 nm). This SPR model is equipped with 2 flow cells which can be connected either in parallel or serial manner. It also has 6 independent sample lines that automates liquid handling for unattended runs. In particular, measurements with all 3 lasers can be done with the same spot in a flow cell, enabling detection of layer thickness, refractive index or conformation changes on the senso r surface.

SPR metal sensor chips were acquired from Bionavis. The sensors were made of glass slide (e.g., BK7) coated with 10 nm chromium adhesion layer and 50 nm gold plasmonic layer (Figure 3.9). SAM can be readily functionalized on the gold surface with universal cleaning. For supported lipid bilayer formation, an additional 10-15 nm SiO_2 layer was coated on the
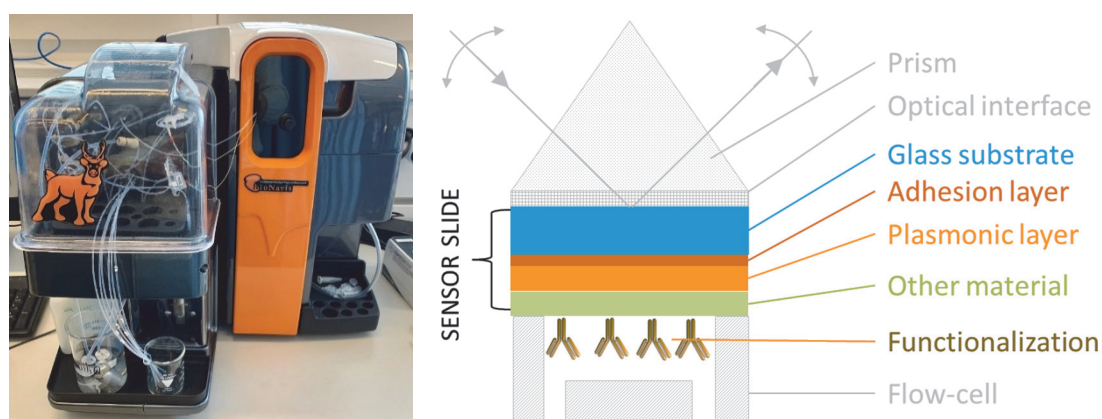
Figure 3.9. Configuration of the MP-SPR facility. Picture of the SPR instrument is shown on the left, while a schmatic illustration of the sensor slide is shown on the right. The sensor slide measures 12×20 mm and different materials can be coated on top of the plasmonic layer via spin-coating, atomic layer deposition (ALD), chemical vapor deposition (CVD) and others.

gold surface via ALD. Prior to use, the chips were consecutively rinsed with acetone, ethanol and water, and further cleaned in piranha solution (H_2SO_4:H_2O_2 = 3:1) for 1 minute. Functionalization of SMA or lipids is described in section 3.5.1 and 3.5.2.

The SPR instrument was thoroughly cleaned and sterilized with 70% ethanol before use in cell affinity measurements. Affinity analyses were performed with the real-time sensorgrams obtained at 670 nm in both flow cells. All affinity measurements were carried out by angular scanning (60°–75°, scan speed 1.5 s) with a continuous buffer flow and constant temperature at 16 °C.

3.6.2 Determination of layer thickness with BioNavis LayerSolver™

The characterization of layer thickness is performed by spectral peak analysis using the three wavelengths with curve fitting and iteration. To extract the thickness, we fit a dielectric multilayer model to the measured SPR curves using the BioNavis LayerSolver™ software. The fitting procedure works by modeling the multilayered optical system in terms of thickness (d), refractive index (n) and attenuation coefficient (k), and then numerical calculations are iteratively performed using Fresnel's equations and a transfer matrix formalisms of 2×2 matrices [127], [128].

3.7   Real-time analysis of spectral data

We developed a customized MATLAB script based on centroid algorithm for real-time sensorgram recording with the spectroscopic imaging setup. The acquired sensorgrams were further processed in Origin 8.0 for baseline corrections and offsetting curves from multiple sensor units or ROIs to a common starting point for data showcase and quantification. To quantify the spectral shift and interpolate the calibration curve, curve fitting of the sensorgrams was performed with nonlinear regression using GraphPad Prism 7. The spatial mapping (correlation between molecular amplitude and multiple ROIs locations in Chapter 5) was done by fitting with Gaussian Lorentizian distribution. For the cell affinity analysis, affinity parameters were extracted by fitting the SPR sensorgrams to a 1:1 interaction model for association and dissociation. Data analysis was carried out with GraphPad Prism 7 software.

3.8   Evaluation of water evaporation through thin PDMS membrane

In chapter 5, a multifunctional microfluidic system is employed to minimize the water evaporation from the single-cell microchamber. This system can be considered as three distinct PDMS membranes from a cross-sectional view (Figure 3.10). These include the bulk PDMS which can be considered as a thick membrane (No. 1), the pneumatic valve actuation
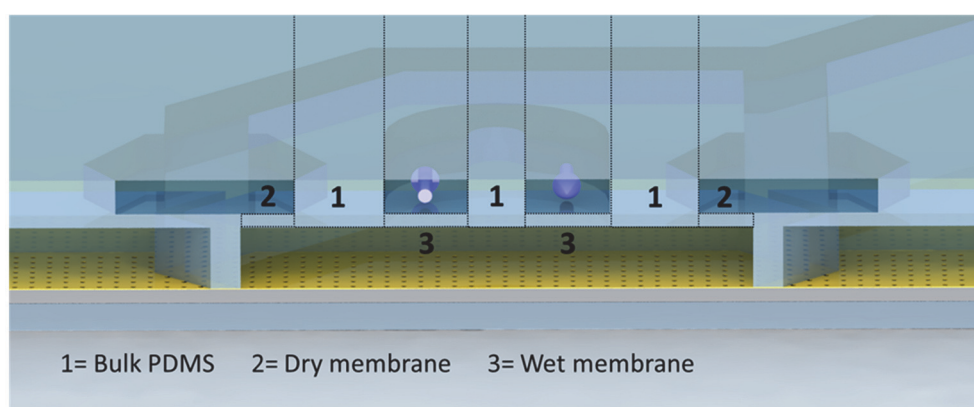
Figure 3.10. Schematic cross-sectional view of the microfluidic device, where numbers label the different membrane areas of the device.

membranes which are considered as a dry membrane (ambient humidity, No. 2) and the regulation channel which can be considered as the wet membrane (No. 3).

Therefore, the total vapor loss $\dot{V}_{\text{total}}$ can be expressed as:

$$\dot{V}_{\text{total}} = \dot{V}_{\text{PDMS}} + \dot{V}_{\text{dry membrane}} + \dot{V}_{\text{wet membrane}} \tag{3.1}$$

The evaporation rate $\dot{V}$ across each of these membranes can be described as [129]:

$$\dot{V} = \lambda_{\text{water-PDMS}} \left(P_{\text{saturation}} - P_{\text{vapor}} \right) \frac{A_{\text{membrane}}}{d_{\text{membrane}}} \tag{3.2}$$

where $\lambda_{\text{water-PDMS}}$ is the permeability of water vapor through PDMS which is reported as 3600 cm^3$_{\text{(STP)}}$ · cm/(s · cm^2 · cmHg)**** [130]. $P_{\text{saturation}}$ and P_{vapor} are the vapor saturation pressure, and the vapor partial pressure, respectively. A_{membrane} and d_{membrane} are the surface area and thickness of the PDMS membrane, respectively, which vary for the three components of our system. Since P_{vapor} depends on the relative humidity (RH, or φ) of the surroundings, it can be described as [131]:

$$P_{\text{vapor}} = \varphi \, P_{\text{saturation}} \tag{3.3}$$

Meanwhile, $P_{\text{saturation}}$ depends on the ambient temperature [131], and varies as below for ambient temperatures ranging from 20 to 70 °C:

$$P_{\text{saturation}} = 0.1348 \, T_{\text{amb}}^3 - 6.6754 \, T_{\text{amb}}^2 + 274.28 \, T_{\text{amb}} - 1570.7 \tag{3.4}$$

Once combining the above equations, the volume evaporation rate of water vapor through PDMS membranes can be calculated as below:

$$\dot{V}_{\text{vapor}} = \lambda_{\text{water-PDMS}} \cdot P_{\text{saturation}} \cdot (1 - \varphi) \frac{A_{\text{membrane}}}{d_{\text{membrane}}} \tag{3.5}$$

**** This is a non-SI unit for gas permeability through polymer membranes, which is called **barrer**. Here, the cm^3$_{\text{(STP)}}$ means standard cubic centimeter, referring to a unit of amount of gas rather than a unit of volume.

Chapter 4

Real-time monitoring of cytokine secretion from cancer cells

Disclaimer: This chapter is adapted from the following article by permission of The Royal Society of Chemistry:

- **X. Li**, M. Soler, C. I. Özdemir, A. Belushkin, F. Yesilköy, H. Altug, Plasmonic nanohole array biosensor for label-free and real-time analysis of live cell secretion, Lab Chip 17, 2208–2217 (2017)

My contribution: Study conceptualization, experiment design and operation, result analysis, and manuscript drafting

---

4.1 Introduction

Over the past decades, label-free biosensors have emerged as a powerful analytical tool for sensitive and real-time detection of biomolecules (e.g. proteins and nucleic acids), and more complex entities such as bacteria, viruses, and mammalian cells [60], [132]. Among them, plasmonic biosensors have demonstrated high sensitivity and robustness, presenting promising compatibility for laboratory research and development of point-of-care devices [133], [134]. For instance, the surface plasmon resonance (SPR) biosensors enable direct monitoring of biomolecular interactions in real time and accurate quantification of the analytes without the need for labels or amplification steps [135]. However, the conventional SPR biosensor

platforms require complex prism-coupling instrumentation, which hampers both the high throughput required for multiplexed analysis and the integration of lab-on-a-chip systems.

Nanoplasmonic biosensors featuring nanoscale structures (e.g. nanoapertures, nanoparticles) have recently gained significant attention as they can meet the above needs [136]. In particular, those consisting of gold nanohole arrays (nanohole arrays) have demonstrated unique capabilities for multiplexed and label-free detection in a compact footprint, which are promising for miniaturization and integration in lab-on-a-chip devices [73], [137]. Several studies have demonstrated the excellent performance of nanohole array-based biosensors for the direct detection of proteins, nucleic acids, exosomes, or microorganisms [117], [138], [139]. Furthermore, nanohole arrays have shown an outstanding multiplexing capability as high-throughput analysis platform since they can be organized in a highly compact manner. Chang et al. fabricated an array of up to 1.5 million nanohole sensor pixels on a single glass slide with a packing density of 816 sensors per mm^2, which is comparable to that of state-of-the-art fluorescence-based microarrays [113]. Moreover, as the EOT phenomenon circumvents the need of prism-coupling mechanism, the nanohole array-based biosensor could be readily fit with lens-free on-chip imaging setups, providing an ideal sensing format for miniaturized point-of-care devices [140].

Although nanoplasmonic biosensors are highly promising for sensitive biomolecular detection, their application to incorporate live cells and to study cellular functions is still in their infancy. The extension to in situ cell analysis applications requires the biosensor to support a highly robust and stable microenvironment for long-term cell characterization, which can range from several hours to days. So far, the cell secretion analysis with nanoplasmonic biosensors has been limited either to protein quantification in isolated blood, serum samples and culture supernatants or to the monitoring of immediate cell responses covering only a few hours (1-3 h) [94], [95], [141], [142]. The integration of cell culture modules is thereby necessary to control and preserve cell viability and facilitate long-term analysis of cellular activities in appropriate conditions. Furthermore, the device needs to operate in complex solutions (e.g. cell culture media) to maintain high cell functionality. This implies that the sensor should be able to discriminate the target proteins from other fouling agents, ensuring a high detection selectivity. And finally, it is important to mention that the secreted cytokines or signaling

factors are usually small biomolecules (<30 kDa) produced at low concentrations. Therefore, it demands a highly sensitive performance of the biosensor to detect the molecules in a direct manner, without the need for labels or amplification steps.

In this study, we introduce a nanoplasmonic biosensor platform integrated with microfluidic live cell culture for real-time monitoring of cellular secretion directly in complex culture media. The platform consists of a highly versatile microfluidic cell culture module combined with a readily implementable nanohole array-based biosensor. The sensing principle of our plasmonic sensor enables high-resolution spectroscopic imaging of multiple sensor arrays simultaneously by utilizing normal broadband illumination and simple bright-field transmission optics. This operation scheme provides direct compatibility of our platform with a conventional inverted microscope, which is usually available in a general biology laboratory.

We demonstrated the excellent performance of our biosensor by analyzing the real-time secretion of vascular endothelial growth factor (VEGF) from live cancer cells. This cytokine plays a key role in various processes in developing cancers, such as angiogenesis, progression, and metastasis. Thus, the label-free monitoring of VEGF secretion could be of genuine interest for cancer research and the development of anti-cancer therapies. We performed stable real-time monitoring of cytokine secretion over 10 hours by employing a comparable number of cells to that adopted in conventional methods. Cell viability was not only well preserved throughout the measurements, but we could also recover the cells after the experiment for further studies. The nanoplasmonic biosensor demonstrated successful functionality with complex cell culture media by achieving an outstanding sensitivity of 145 pg/mL (~5 pM) for VEGF detection. We obtained equivalent results from independent cell measurements, and the detection outcome was validated with standard ELISA experiments, confirming the good reproducibility and accuracy of the biosensor. Similarly, our nanohole array-based biosensor platform could be extended to the analysis of other cell types (e.g. stem cells) and also for the real-time monitoring of cytokine secretion in a multiplexed configuration. This platform may provide new analysis tools that offer significant insights into cell biology and facilitate the development of more efficient therapies.

4.2 Results and discussion

4.2.1 Biosensor system assembly and working principle

Our integrated biosensor is composed of two complementary and adjustable microfluidic modules, namely the cell culture module and the optical detection module (Figure 4.1). For the microfluidic cell module, we fabricated a single zigzag channel in a polydimethylsiloxane (PDMS) slab that was permanently bonded to a glass slide (Figure 3.5). The growth area could be easily adjusted to provide an appropriate number of cells by simply changing the length and width of the channel. The cell module also includes inlet and outlet tubing connections for introducing fresh culture media, chemical stimuli, and directly delivering the secreted proteins to the adjacent detection module. The optical detection module consists of gold nanohole array-based biosensor, which is also integrated with a PDMS microfluidic system. The nanoholes (200 nm diameter, 600 nm period) were fabricated by deep-UV lithography on freestanding SiN_x membranes, and each nanohole array was defined to have an area of 100×100 μm (Figure 3.3). In this module, the microfluidic system includes three parallel microchannels, and each channel covers three in-line nanohole arrays with a volume of
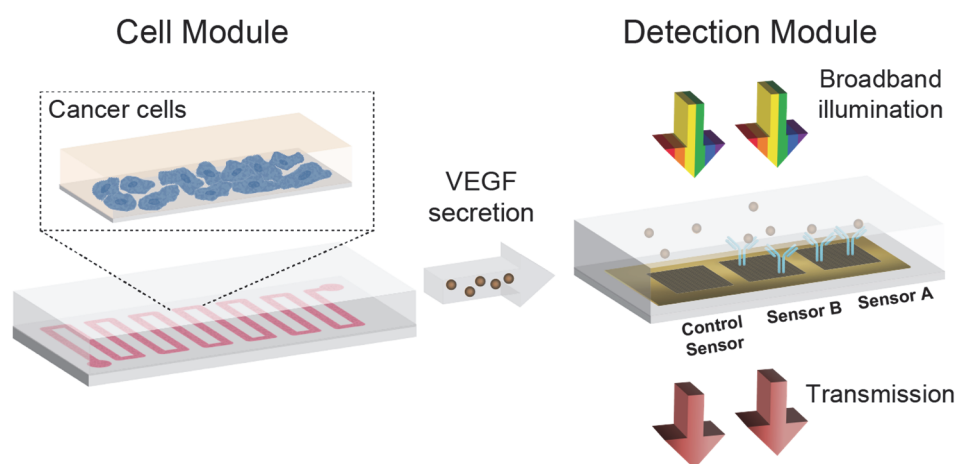
Figure 4.1. The illustration of the biosensor system configuration. Cancer cells grow in a zigzag single-channel PDMS unit, and the secreted cytokines are directly delivered to the adjacent detection module. The detection module illustrates the three in-line nanohole arrays in one microfluidic channel. Two of the arrays are functionalized with specific anti-VEGF antibodies (blue) and the third one without antibodies as a negative control sensor.

4.2. Results and discussion

150 nL. The complete biosensor system including the two modules has approximate dimensions of 2.5×6 cm².

Taking advantage of the multiplexing capability of our biosensor, we functionalized two of the nanohole arrays with anti-VEGF antibodies, leaving the third one as a negative control. For our experiments, we employed one microfluidic channel at a time, but it is worth mentioning that we could also incorporate multiple cell culture modules for different channels, enabling the simultaneous analysis of distinct types of cells. Antibodies specific to VEGF were selectively immobilized on the gold nanohole arrays as biorecognition molecules to capture the analytes (Figure 4.2). In this way, the VEGF secreted by the cancer cells can be directly captured by the specific antibodies without the need for sample pretreatment or purification steps.
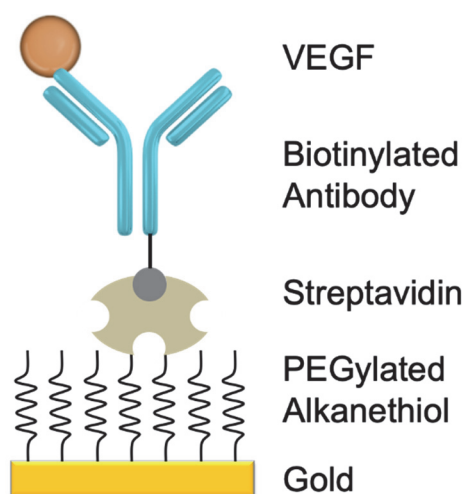
Figure 4.2. Schematic illustration of the surface chemistry for selective detection of VEGF.

For real-time analysis, we placed the biosensor on the inverted microscope, and a collimated broadband light source illuminated the three in-line nanohole arrays at normal incidence (Figure 4.1). The transmitted light is collected simultaneously by a 4× objective and entered the imaging spectrometer through a 400 μm-wide input slit. The three sensors are simultaneously imaged along the vertical slit of the spectrometer. The spectral content of each sensor is dispersed by a medium grating (600 lines/mm)

and recorded on a 1024×1024-pixel CCD with a pixel size of 13×13 μm. In this optical read-out scheme, the recorded two-dimensional CCD data contains spatially resolved 1D spectral image: one axis of the image corresponds to the positions of three sensors, and the other axis corresponds to their spectral response (Figure 4.3).

Using this readout scheme, the EOT spectrum from each sensor unit is simultaneously acquired for biosensing analysis. The spectral coverage and resolution are controlled by the choice of the grating. The number of spectrally resolvable sensors is determined by the total magnification of the system, as well as the size and positioning of the nanohole array sensors on the chip. For instance, with one sensor unit measuring 100×100 μm and being separated by 50 μm in between, we could image 20 in-line sensors with a 4× objective simultaneously. In our case, the spectral content of each nanohole array sensor is recorded by ~30 pixels, and the entire spectral coverage ranges from 830 nm to 890 nm. In aqueous solution, the EOT resonance peak of nanohole array sensor locates at 850 nm approximately, which is well accommodated within the spectroscopic imaging range.

The capture of VEGF on the sensor induces the change of refractive index proximate to the surface and thus results in a peak shift of the EOT spectrum. By tracing the spectral
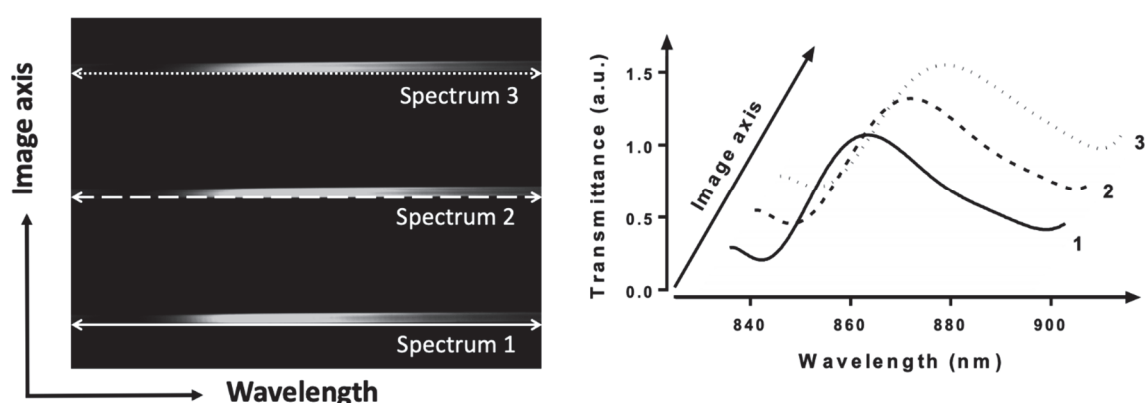
Figure 4.3. Spectroscopic imaging of the nanohole arrays. The spectral image recorded by the spectrometer and CCD camera shows the spectral information from the three in-line NHA sensors simultaneously (left). Each spectrum is then extracted from the image, showing the EOT resonance peaks for detection analysis (right).

shifts continuously, we are able to resolve the sensorgram (i.e. binding curve) of VEGF binding kinetics, and thus monitor the dynamics of cell secretion (Figure 4.4). We implemented a custom MATLAB script based on the centroid algorithm to track the spectral shifts [143]. This data processing method calculates the center of mass of the resonance peak and plots the corresponding wavelength as a function of the time. Unlike the conventional interrogation of the maximum value of the peak, this centroid algorithm can extraordinarily minimize the systematic noise and increase the signal-to-noise ratio, therefore reaching lower limits of detection.
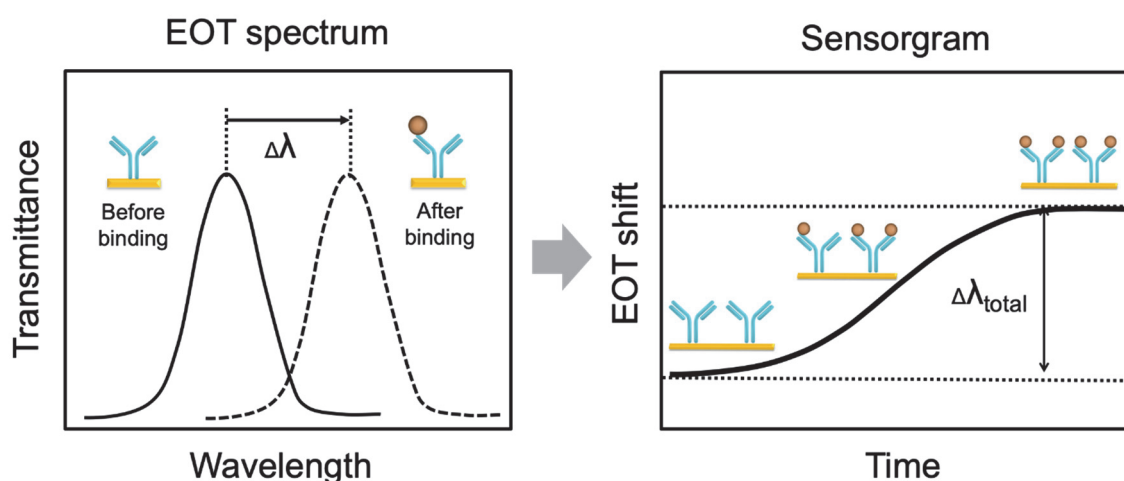
Figure 4.4. Sensing principle of the real-time detection. The EOT spectrum from each nanohole array shows a characteristic resonance peak (solid line). Biomolecular binding on the sensor surface induces an EOT spectral shift of the peak (dashed line). As molecular binding accumulates, the spectral displacements of the resonance peak are then plotted in the sensorgram (EOT shift vs. time) to reveal the real-time binding dynamics.

4.2.2 Surface functionalization and biosensor calibration for VEGF detection

Before measuring the cell secretion, we characterized the performance of our biosensor for VEGF detection. In affinity-based biosensors, it is essential to establish a robust and stable surface chemistry strategy that ensures sensitive, selective and reproducible detection of the analyte of interest. This is particularly important for live cell secretion analysis since we monitor the cellular activity for extended periods of time, and we need

to detect low concentration of proteins (usually in the range of pg/mL). We employed the well-known biotin/streptavidin interaction for the biofunctionalization of the nanohole array sensors (Figure 3.7). This strategy enables a highly stable immobilization of biotinylated antibodies due to the high affinity between the streptavidin and the biotin molecule ($k_D \approx 10^{-14}$ mol/L). Furthermore, since the biotin tag is conjugated to the Fc domain of the antibodies (i.e. non-antigen binding domain), the antibodies are immobilized in an oriented manner, leading their antigen binding sites (Fab' domains) entirely available for antigen capture.

First of all, we created an anti-fouling layer on the sensor surface that prevents binding of nonspecific molecules. We took advantage of polyethylene glycol (PEG) derived compounds, which have demonstrated high resistance to protein adsorption due to its hydrophilic properties [144]. In particular, we created a mixed self-assembled monolayer (SAM) consisting of two kinds of PEGylated alkanethiols carrying a reactive carboxylic functional group (–COOH) and a non-reactive hydroxyl group (–OH), respectively. The latter was used as a lateral spacer to minimize steric hindrance issues during protein attachment. The –COOH functional groups were activated by the general carbodiimide chemistry (i.e. EDC/NHS activation) and then a layer of streptavidin was covalently bonded. Finally, we employed the state-of-the-art piezoelectric micro spotting technique to locally deposit the biotinylated anti-VEGF antibodies on two of the nanohole array sensors (Figure 3.7). This allowed us to define the third sensor in the same channel as a reference to compensate the possible false positive signal produced by nonspecific molecular binding or systemic perturbations.

Once the plasmonic microarray was functionalized, it was assembled with microfluidics and connected to a syringe pump and a manual injection valve for the characterization measurements. We carried out a standard calibration curve to evaluate the sensitivity of our plasmonic biosensor for VEGF detection. Samples spiked with various concentrations of recombinant VEGF, ranging from 200 pg/mL to 1 ng/mL, were introduced and flowed over the functionalized microarrays. The binding of VEGF to the antibodies was clearly detected by resonance peak shifting ($\Delta\lambda$) in a concentration-

dependent manner (Figure 4.5a). The values obtained from each sample were plotted and fitted to a linear regression model (Figure 4.5b). We determined the Limit of Detection (LOD) of our biosensor, which is the lowest analyte concentration that the biosensor can reliably detect. It is defined as the concentration with a signal corresponding to three times the standard deviation of the blank [145]. We achieved an outstanding LOD of 145 pg/mL (5.37 pM) for VEGF, which overlaps the physiological concentration range reported in other related biological studies [146], [147].
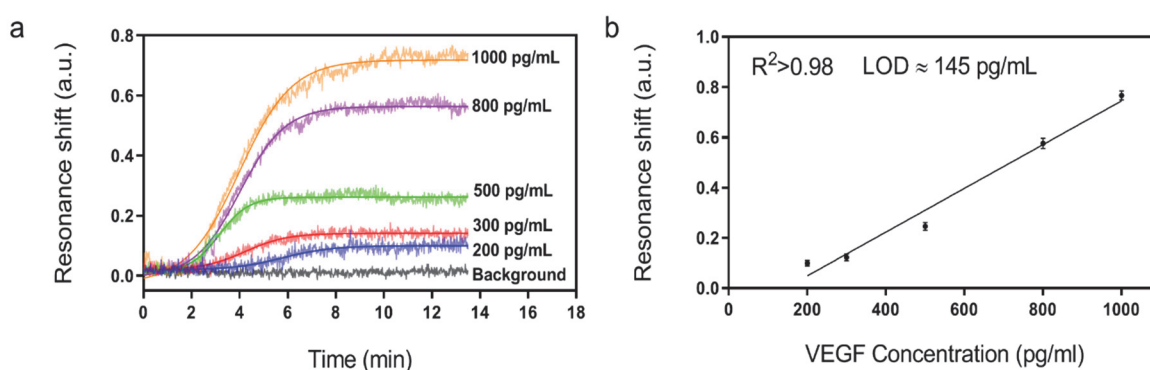
Figure 4.5. **Evaluation of the plasmonic biosensor sensitivity for direct detection of VEGF**. (a) The sensorgrams of the direct detection of VEGF ranging from 200-1000 pg/mL. (b) Standard calibration curve for VEGF detection. Data plots represent the mean and standard deviation of each concentration measured in triplicate. Plots are fitted to a linear regression model ($R^2 > 0.98$), and the Limit of Detection (LOD) is calculated as the concentration corresponding to 3 times the standard deviation of the blank signal.

4.2.3 Probing the optimal condition for VEGF secretion from HeLa cells

In parallel to the biosensor characterization, we determined the stimulation scheme for VEGF secretion of HeLa cells. Currently, there is no uniform protocol to stimulate the VEGF secretion from the cells. A calcium ionophore, namely A23187, has been employed as a popular stimulus for VEGF secretion in various studies. It can increase the intracellular Ca^{2+} levels rapidly and allow divalent ions to cross plasma membranes. Various reports have demonstrated a significant increase in VEGF secretion from different cells stimulated by the ionophore, albeit reporting a broad range of concentrations from hundreds of nanomolar to micromolar [90], [146]. Therefore, we

tested a variety of cell culture conditions to stimulate the exocytosis of VEGF from HeLa cells. Cells were grown in multi-well plates and incubated overnight with different concentrations of A23187, ranging from 1 to 100 μM. Supernatants were collected and analyzed by sandwiched VEGF ELISA assay. As shown in Figure 4.6a, the VEGF secretion showed a biphasic profile depending on the concentrations of A23187. A marked increase in VEGF production was achieved with 1 and 10 μM of A23187, which was more than two times higher than the control group (i.e. Ctrl, w/o stimulus). Whereas, the stimuli exhibited significant cytotoxicity with concentrations greater than 100 μM. Cellular viability was significantly reduced by exhibiting apoptotic cellular morphology under optical microscopy, along with scarce secretion of VEGF. Therefore, to facilitate maximum VEGF secretion and avoid cytotoxicity induced by the ionophore, the concentration of A23187 was selected to be 10 μM for the following studies.

Additionally, we also tested the influence of different serum concentrations in the culture media as another critical role for cytokine secretion. The serum is supplemented with 10% v/v in routine cell culture for the majority of mammalian cells. However, reduced serum contents have been studied as a typical starvation condition to stimulate a variety of cellular metabolic activities, including VEGF expression [148], [149]. Therefore, we incubated HeLa cells in serum-free media (SFM), and media with serum concentrations of 1%, 5%, and 10%. We compared the VEGF secretion amount by analyzing the supernatants from each group with sandwiched ELISA. As shown in Figure 4.6b, serum-free media (SFM) and 1% serum induced a decrease in VEGF secretion compared to conventional cell media (10%), which could be attributed to cell death during incubation. However, 5% of serum showed a comparable VEGF production without adverse effect in cell viability. Moreover, reduced serum components could ameliorate microfluidic performance by reducing bubble generation, and even improve the antigen-antibody interaction with fewer interferences. Therefore, the cell culture media supplemented with 5% of serum and 10 μM of A23187 (hereinafter VEGF-stimulating media) was employed in the following experiments to induce VEGF secretion from HeLa cells.
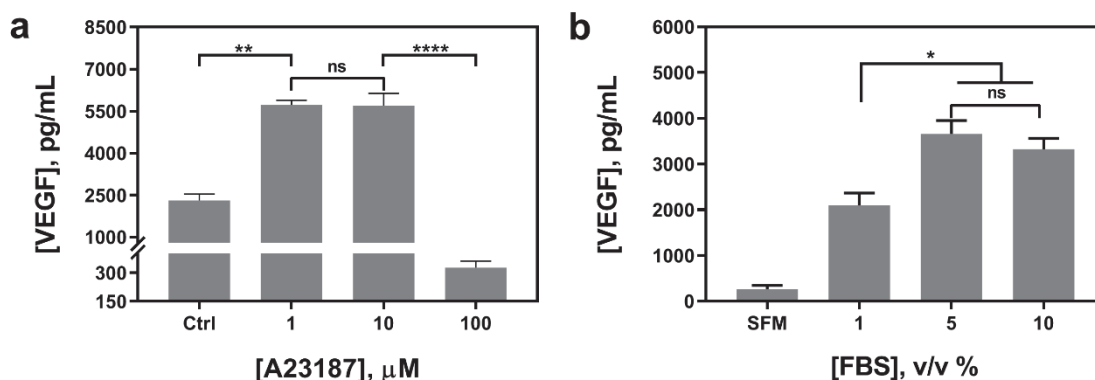
Figure 4.6. Assessment and optimization of cell culture conditions for VEGF secretion from HeLa cells. (a) VEGF concentration measured in cell culture supernatants after administration of calcium ionophore at different levels ([A23187] = 0 as Ctrl; $p<0.005$: **; $p<0.0001$: ****; ns: non-significant; n=2) (b) VEGF concentration measured in cell culture supernatants in presence of different serum concentrations ([FBS] = 0 as SFM; $p<0.05$: *; ns: non-significant; n=2)

4.2.4 Evaluation of cell viability and VEGF secretion in microfluidic culture

Once the conditions to stimulate VEGF secretion were established, we examined the influence of our microfluidic culture module on the behavior of living cells, instead of the conventional multi-well plates (Figure 4.7a). First, we studied the effect of constant media flow on cell attachment, cellular morphology, and their viability in our microfluidic module. The flow is necessary to assure an immediate delivery of the secreted cytokines to the optical module. The glass surface in the microfluidic chamber was coated with 0.1% gelatin to improve cell attachment. Later, HeLa cells (cell number $\approx 10^5$) were seeded into the channel (growth area: 1 cm^2) and incubated overnight at 37 °C and 5% CO$_2$, allowing cells to attach and spread along the substrate. As shown in Figure 4.7b, the cells firmly attached and spread extensively on the glass surface. The module was then placed back in the incubator (37 °C and 5% CO$_2$), connected to a syringe pump and a flow of VEGF-stimulating media was introduced. Different flow rates were tested (from 5 to 50 µL/min) in order to set a suitable flow velocity. A flow rate of 10 µL/min was found to preserve a low shear stress by avoiding cell detachment while enabling rapid delivery of the secreted cytokines to the detection module.

Furthermore, we performed a preliminary study for the time profile of VEGF secretion under microfluidic flow conditions. After the injection of the stimulus with a constant flow rate through the cell module, we collected the outgoing supernatant in different vials (~300 µL) before transferring the samples to an ELISA plate for VEGF quantification. The samples were collected every 1 hour for 10 hours. Results in Figure 4.7c showed the VEGF concentrations obtained from the discrete supernatant samples. The amount of VEGF gradually increased and reached a peak level around the 5th hour, which remained at a plateau for 4 hours. The concentration of VEGF in the plateau phase reached ~380 pg/mL, which is within the detection range of our label-free nanoplasmonic biosensor (Figure 4.5).
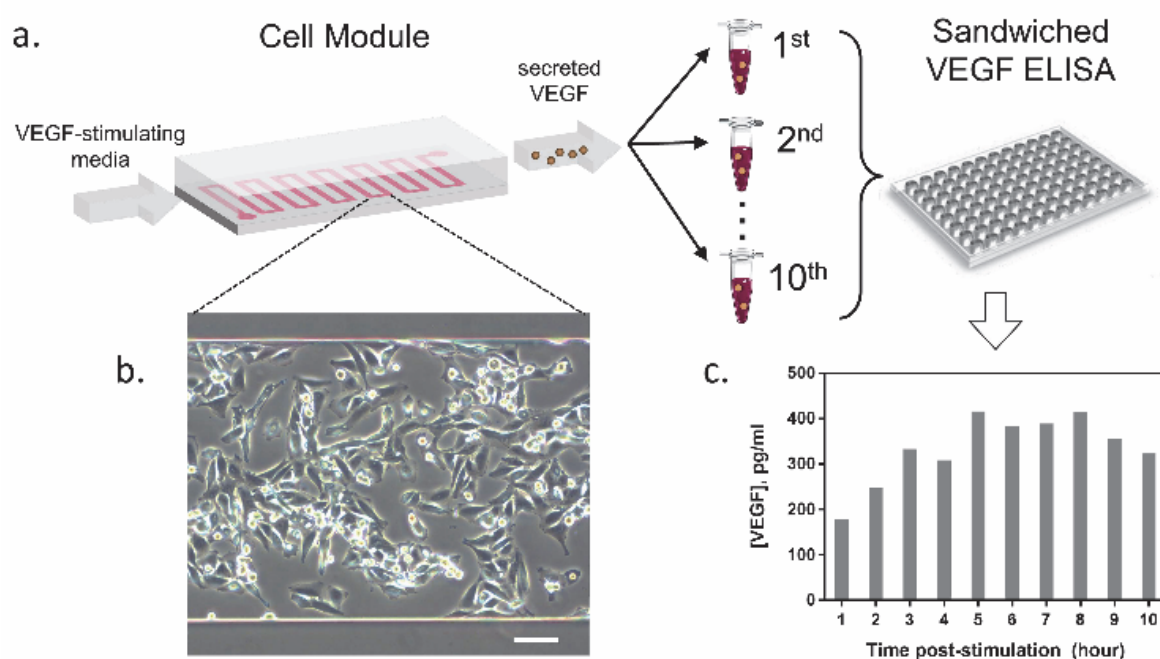
Figure 4.7. Study of the cell viability and VEGF secretion in microfluidic culture. (a) HeLa cells were cultured in the microfluidic module with VEGF-stimulating media and supernatants were collected every hour for 10 hours. The discrete samples were analyzed by sandwiched ELISA. (b) The magnified microscopic image of live HeLa cells cultured in the microfluidic channel. (c) Discrete time profile of VEGF secretion analyzed by ELISA, with a maximum peak reached after approximately 5 hours post-stimulation.

4.2.5 Monitoring the VEGF secretion in real-time

Following the characterization of our biosensor for VEGF detection and establishing the optimal secretion scheme from cells, we demonstrate the ability to perform real-time analysis of VEGF secretion from live cells. The gold nanohole array biosensor was functionalized as described above and integrated with the microfluidic system as the detection module. The multiplexing capability of our biosensor enables to include within the same microfluidic channel two independent nanohole arrays for the specific detection of VEGF (Sensor A and Sensor B) and a reference sensor (Sensor C). This ensures the reliability of the experiment by providing two assay replicates simultaneously, and guarantees the selectivity and specificity of the measurements, as the reference sensor provides an integrated negative control. To further ensure the selectivity of the biosensor to VEGF from the complex composite of cell media, the sensor surface was first blocked with the complete cell media after antibody immobilization. This blocking step prevents undesired nonspecific adsorptions of other proteins present in the media, so that the sensor response can only derive from VEGF specifically captured on the antibodies.

In parallel, a microfluidic cell module was prepared by seeding the HeLa cells and incubating them overnight under the same conditions as described before. Then, the two modules were connected by microfluidic tubing and placed on the inverted microscope. A custom incubation box was put on the cell module to provide the appropriate culture conditions (37 °C and 5% CO_2). The VEGF-stimulating media was introduced with a flow rate of 10 μL/min throughout the measurement. The stimulus A23187 was confirmed not to interfere with the VEGF detection (Figure 4.8). The EOT spectra from the three in-line nanohole array sensors were simultaneously monitored for 10 hours (1 spectrum per second).
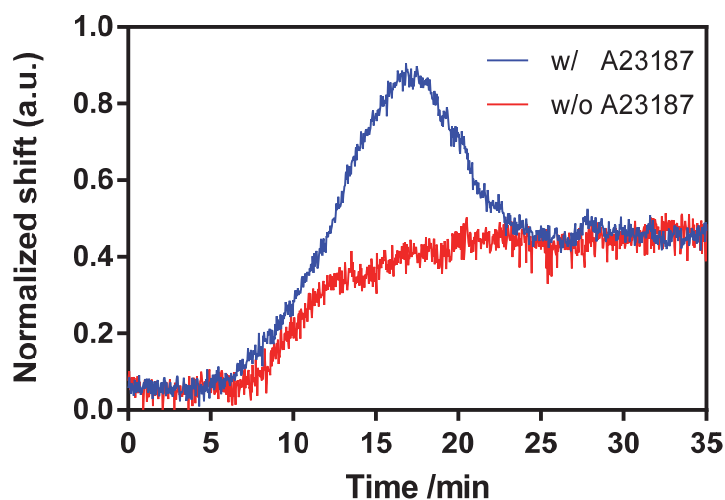
Figure 4.8. Influence of A23187, on the optical signal. The VEGF samples (1μg/ml) prepared with A23187 (blue curve) or without A23187 (red curve) were injected into the bisosensor functionalized with anti-VEGF antibodies. Despite the bulky refractive index change induced by the stimuli, there is no significant spectral shift between these two samples, indicating that A23187 does not interfere with VEGF detection.

During the measurement, we observed a significant resonance shift emerging at approximately 5.5 h after the introduction of VEGF-stimulating media (Figure 4.9a), which corresponds well to the time profile obtained by ELISA analysis. The signal was obtained from the two nanohole array sensors functionalized with the anti-VEGF antibody (Sensor A and Sensor B) while the control sensor remained in a stable baseline. The absence of resonance response on the control sensor implies the lack of interference from other proteins and confirms the selectivity and specificity of our biosensor for VEGF detection. By interpolating the resonance shifts from both functionalized sensors with the VEGF calibration curve, it corresponded to an average VEGF concentration of 239.7 pg/mL. Following this increase, no significant binding events were observed from the optical responses, implying that the secretion of VEGF reached a peak.

In order to ensure the reliability of our results, we performed a second independent measurement with new cells and a different plasmonic microarray but employed the same conditions as described before. A similar shift emerged at approximately 6 hours

of monitoring, which corresponded to an average VEGF concentration of 235.8 pg/mL (Figure 4.9b). Again, this time, the signal was clearly seen for the two specific anti-VEGF sensors while the control reference showed a flat baseline. The two concentrations for VEGF secretion were equivalent, which demonstrates good reproducibility of our biosensor. Besides, the values obtained with our plasmonic microarray were in the same concentration range as those measured by ELISA with samples at discrete time points, therefore proving that our integrated biosensor can be used for continuous real-time monitoring and label-free quantification of cell secretion with good accuracy. It is worth mentioning that in this case, we employed ELISA to primarily confirm the time profile of VEGF secretion, rather than a validation method in terms of quantification due to the different working principle and sample collection manner. For ELISA, each sample was harvested for one hour, thus the VEGF is accumulated resulting in a relatively high concentration. In our plasmonic biosensing, the supernatant is not accumulated but it is immediately and continuously flowed over the sensor surface. Thereby, the VEGF does not accumulate, and its concentration may be lower. Furthermore, we checked the viability and number of cells after both experiments, which were well maintained after the long-term measurements, confirming the reliability of the obtained signals.

Our experiments demonstrated the significant advantages that nanoplasmonic label-free biosensor offers versus the traditional enzymatic immunoassay techniques (e.g. ELISA), regarding simplicity, reagent consumption, and especially the real-time monitoring capability. Poor time resolution is inevitable with conventional analysis as samples are harvested at discreet time points and each sample has to be accumulated for a certain duration, causing laborious experimental operation for long-term analysis. However, label-free nanoplasmonic biosensors do not require pre-harvested samples and are capable to operate continuously for the analysis, which greatly enhance the temporal resolution and enable cost-effective and effortless biodetection. This label-free biosensing platform paves a new avenue for quick evaluation of secretion ability among

different cells (e.g. VEGF-secreting vs. non-secreting cells), or potent chemical agents for drug development.
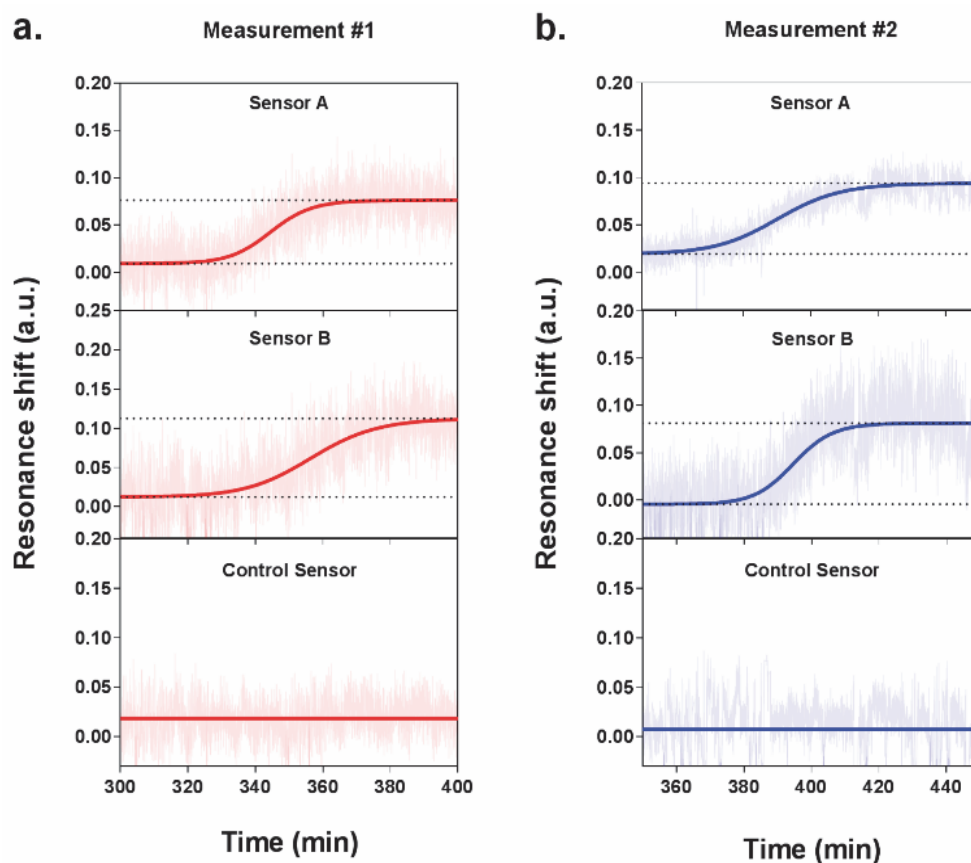
Figure 4.9. Real-time detection of VEGF secretion from live HeLa cells with the plasmonic nanohole array biosensor. The real-time measurements obtained from two independent experiments are showed in (a) and (b). Each graph showed the three sensorgrams acquired from the three individual sensor arrays in the detection module: Sensor A and Sensor B were functionalized with anti-VEGF antibodies, while Sensor C without antibodies as a negative control. In both experiments, sensorgrams obtained from Sensor A and B showed a clear increase of the signal while the Control Sensor remains at a low flat baseline.

4.3 Conclusion

We introduced a novel nanoplasmonic biosensor platform for the monitoring of live cell secretion activity in a real time and label-free configuration. By incorporating a microfluidic cell culture module and an optofluidic biosensor equipped with a robust and specific surface chemistry, we performed the first reported label-free and long-term analysis of cytokine secretion events by using plasmonic nanohole array-based biosensors. The biosensor functions based on plasmonic EOT principle, enabling effortless device operation on a basic inverted microscopy setup and circumventing the needs of complex prism-coupled configuration in SPR. We achieved an outstanding sensitivity of 145 pg/mL for VEGF detection in complex media. Additionally, the nanohole array biosensor showed excellent agreement with measurements performed by the current gold-standard ELISA technique, validating our results and demonstrating the reliability of our biosensor. The presented nanoplasmonic biosensor also represents a promising multiplexed sensing platform due to the high-throughput format of nanohole microarrays and versatile surface chemistry on individual sensors. With these capabilities, the proposed label-free plasmonic nanohole array biosensor system provides a powerful analytical tool to monitor live cellular activities in a label-free and real-time manner for various fundamental biological studies, such as the analysis of tumor microenvironments or the evaluation of new therapies.

Chapter 5

Real-time secretion analysis at single-cell resolution

5.1 Introduction

Single-cell analysis is one of the most powerful approaches towards the development of new therapies for serious diseases such as cancer or autoimmune disorders [20]. The analysis of individual cell secretion is essential to fully understand the functional heterogeneity and decipher the underlying mechanisms of cellular interactions and communication. The past few years have seen the advances of innovative strategies for both cell isolation and protein secretion analysis to enable single-cell resolution [150]–[153]. For instance, Love et al. introduced a large-scale microengraved array which is able to generate the populational secretion profiles from single hybridoma cells [150], or even to characterize the cytokine

secretion of single T lymphocytes upon different activation scenarios [153]. While their methods are efficient enough to provide a high-throughput dataset, the intensive washing steps involved in the fluorescence labeling procedure dramatically impairs the temporal resolution (limited to a few hours) of the analysis. On the other hand, droplet microfluidics has been presented as a promising platform for single-cell sorting and analysis [154]–[156]. The technique basically involves encapsulating individual cells in droplets loaded with specific fluorescent antibodies or enzymes for capturing and detecting the secreted cytokines. However, subsequent cytokine quantification requires external readout means, such as flow cytometry or spectroscopic methods that increase the overall system complexity and only provide an end-point result. Despite the capabilities of these new techniques for single-cell isolation, the need of either fluorescent or enzymatic labels for detection significantly impairs the dynamic analysis and monitoring of the secretion in real time.

Label-free biosensors emerge as a unique solution for the sensitive, accurate and real-time analysis of cell secretion [60], [117], [157]. This detection scheme circumvents the tedious and costly molecular tagging and enables the elucidation of biomolecular interactions in a non-invasive and dynamic manner. Among various label-free sensing platforms, nanophotonics, by supporting strong light-matter interaction and dramatically confining light in small volumes, enables ultra-low detection limits, exceptional miniaturization, and ultimate on-chip integration [45]. Particularly, plasmonic nanohole arrays (nanohole arrays) have demonstrated a unique potential and flexibility for the implementation of powerful biosensors with high-throughput analyses and capabilities for point-of-care deployment and utilization [73], [113]. Furthermore, gold nanohole array biosensors have demonstrated exceptional performance for the analyses of proteins and cells in a real-time and multiplexed label-free configuration [121], [122], [137], [158].

5.2 Results and Discussions

5.2.1 Biosensor design for reliable single-cell secretion monitoring

Label-free nanoplasmonic biosensors face critical challenges for addressing single-cell secretion analysis. Cytokines are relatively small molecules (MW[††††] 15-30 kDa) and are secreted in minute amounts (femtograms/ (cell·day)). Therefore, the direct detection of single-cell secretion in real time without any signal amplification is not straightforward. In order to achieve the ultra-high sensitivity required for the detection of cytokines secreted from an individual cell, it can be effective to minimize the local volume surrounding the cells by encapsulating them with micro-chambers. This will result in concentrated molecular distribution in the vicinity of the sensor surface. In this regard, microfluidics technology offers a powerful tool to create a highly miniaturized environment with compartmentalization for the analysis [159].

Nevertheless, the optical monitoring of an ultralow volume in cell culture conditions (i.e., 37°C) introduces a significant evaporation problem. This is especially challenging when using polydimethylsiloxane (PDMS) as the material for microfluidics. This widely used material provides excellent transparency and high gas permeability, making it an ideal substrate for optical cellular bioassays [160]. However, the gas diffusion also leads to evaporation and associated optical noise when handling the ultralow volume of fluid [161], [162]. Water evaporation through PDMS membranes may cause not only an increase in osmolality of the cell media but may also result in bubble formation and eventually dehydration of the cell chamber. These evaporation-mediated osmolality alterations induce local changes of the fluid refractive index, causing dramatic optical signal fluctuations that overwhelm the low magnitude secretion signature of single cells. Conventional approaches to prevent liquid evaporation, such as sealing the aqueous surface with mineral oil [161] or placing numerous sacrificial drops in the vicinity of the analyte chamber [162], can be effective but increase

---

[††††] MW stands for molecular weight.

overall system complexity, limit on-chip integration and pose potential contaminations to the assay. Conversely, thin PDMS membranes between culture areas and oxygen equilibrated water channels have been shown to reduce evaporation, while at the same time maintaining oxygen levels required for sustained culture [163].

We introduce a new approach for the single-cell secretion analysis in real time using a label-free nanoplasmonic biosensor. We have developed an optofluidic device based on a gold nanohole array sensor integrated into an innovative multifunctional microfluidic system for the dynamic and accurate monitoring of cytokine secretion from individual cells (Figure 5.1a). We utilize the single step injection molding technique [124] to create a microfluidic system equipped with pneumatic valves that enables both the in-flow introduction of cells into the device and isolation of a microchamber on the nanostructured sensor chip to confine and analyze individual cells. Figure 5.1b shows a closer scenario of the device structure where a valve-gated microchannel allows us to introduce the cells followed by isolating them within a low volume cell chamber. This creates a high effective concentration of the cytokine molecules and improves the biodetection accuracy. Moreover, we harness the ability of our injection molding approach to create a continuous regulation channel that interacts with the underlying valve-isolated submicroliter cell chamber through thin PDMS membranes. The regulation flow
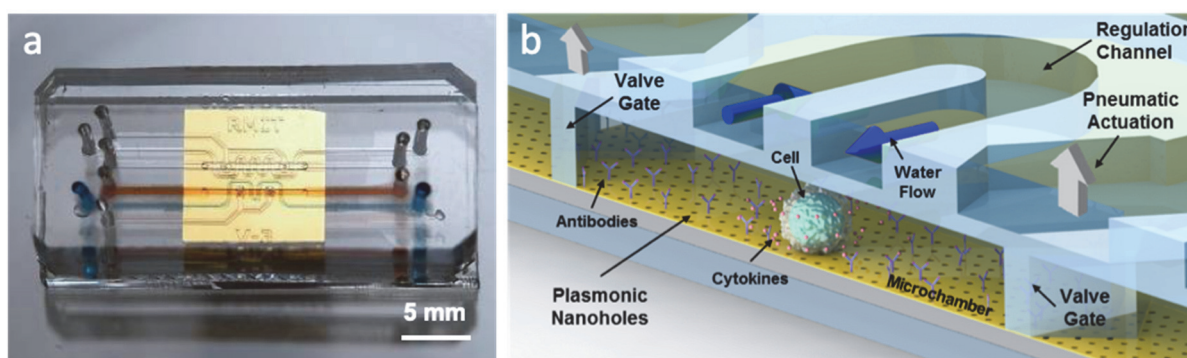
Figure 5.1. Illustration of the optofluidic system for real-time single cell analysis. (a) The picture of the integrated optofluidic device. We highlight the primary channel (orange) and the regulation channel (blue) with flowing colored dyes, respectively. (b) Schematic representation of the microfluidic-integrated nanoplasmonic biosensor. The microfluidic system consists of two fundamental parts: a primary channel in contact with the plasmonic nanohole arrays, which includes two pneumatic valve gates for enclosing a small-volume microchamber, and a hydraulic regulation channel fabricated on top of the microchamber to provide humidity regulation through serpentine water flow.

simultaneously ameliorates evaporation, prevents bubble formation and enables a stable optical background signal for robust monitoring of single cell secretion analysis.

5.2.2 Optical configuration of the nanoplasmonic biosensor

The plasmonic nanohole arrays offer highly sensitive label-free biosensing and are distinguished among other state-of-the-art plasmonic sensors due to the well-proven capabilities for device miniaturization, multiplexed analysis, and easy integration in lab-on-a-chip devices [73], [117], [121]. The current fabrication process for nanoplasmonic sensors requires sophisticated and costly techniques, such as e-beam lithography. This inevitably hinders the implementation of nanoplasmonic technology for routine biological analysis. Therefore, we have employed a nanofabrication procedure [164] enabling efficient and large-scale production of plasmonic nanohole array chips, which minimizes the costs and promotes the real application both in research and clinical fields. The fabrication process is based on deep-UV photolithography technique (Figure 3.4) by using robust quartz wafers as the sensor substrate. As a result, we obtained 4-inch diameter wafers (Figure 5.2a) patterned with uniform arrays of gold nanoholes (200 nm diameter, 600 nm period) across the entire wafer surface as confirmed by SEM image analysis (Figure 5.2c). Wafers were further diced into small sensor chips of 1 x 1 cm^2 (Figure 5.2b) for cell analysis.
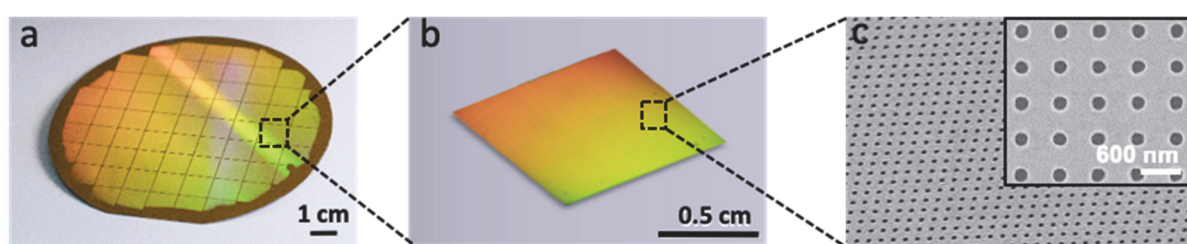
Figure 5.2. Wafer-scale production of nanoplasmonic sensor chips. (a) The plasmonic nanohole arrays are fabricated uniformly on a thin gold film by wafer-scale deep-UV photolithography over the entire 4-inch diameter quartz wafer. (b) The nanopatterned wafer is diced to 1 x 1 cm^2 sensor chip for analysis. The appearance of colors on the chip when viewed at a tilt shows the diffraction grating effect resulted from the nanohole arrays on its surface. (c) An SEM image shows the uniformly distributed nanohole structures on the quartz substrate, where the nanoholes have a diameter of 200 nm and are separated center-to-center by 600 nm.

The working principle of this biosensor is based on the phenomenon of extraordinary optical transmission (EOT), which is represented as a dramatic enhancement of light transmission through the regularly periodic subwavelength nanohole structures [165], [166]. This light enhancement is characterized by the appearance of an EOT resonance peak in the transmission spectrum (Figure 5.3a). The EOT resonance is highly sensitive to minute changes in the near-field refractive index over the nanohole surface. The molecular binding on the sensor surface induces a variation of the refractive index that leads to a spectral shift of the peak wavelength (Figure 5.3b). By tracing the spectral shifts with ongoing experiment time, we are able to depict the molecule binding events in a real-time format.
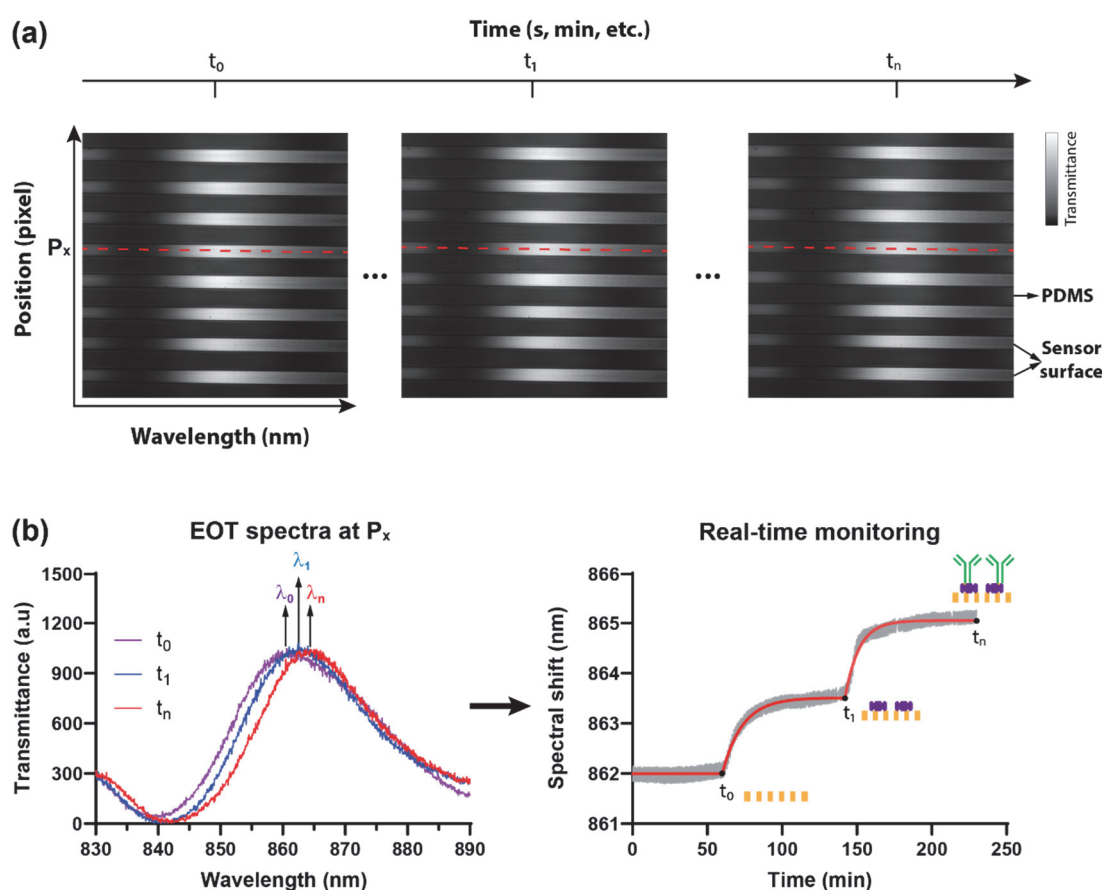
Figure 5.3. EOT-based Sensing principle. (a) The transmission spectra are recorded and analyzed by the spectroscopic imaging setup, forming spectral images over time from t_0 to t_n. The two axes of the spectral images correspond to spatial position and wavelength. (b) Upon bindings of molecules to the sensor surface, spectral shift of the resonance peaks are induced: from λ_0 to λ_n (right panel). By tracking the spectral shifts over time, the real-time monitoring of binding kinetics is achieved.

Regarding the optical measurement, we exploit a spectroscopic imaging method which converts each imaged point to an effective sensing element (Figure 3.1). We placed the sensor chip on an inverted microscope where a collimated broadband light source illuminated the nanohole arrays at normal incidence, resulting in the onset of EOT phenomenon [138]. The transmitted light was collected by the objective underneath and coupled to a spectrometer through a 500 μm-wide slit opening. The spectral content is then dispersed by a grating (600 lines per mm) and recorded on a 1024×1024-pixel CCD camera with a pixel size of 13×13 μm². The recorded CCD image consists of a spatially resolved 1D spectral image in which the horizontal axis represents the range of optical wavelength while the other represents the positions across the illuminated area of the nanohole arrays through the slit opening (Figure 5.3). By adjusting the wavelength to the EOT resonance position (i.e., approximately 860 nm in aqueous solution), we can directly observe the EOT peak and monitor the spectral displacements in real time.

To evaluate the system sensitivity, we carried out a bulk refractive index calibration. A series of glycerol solutions with increasing concentration were injected across a bare sensor surface (Figure 5.4a). The peak shifts were plotted with respect to corresponding refractive index change (the difference of refractive index between each glycerol solution and water). The slope
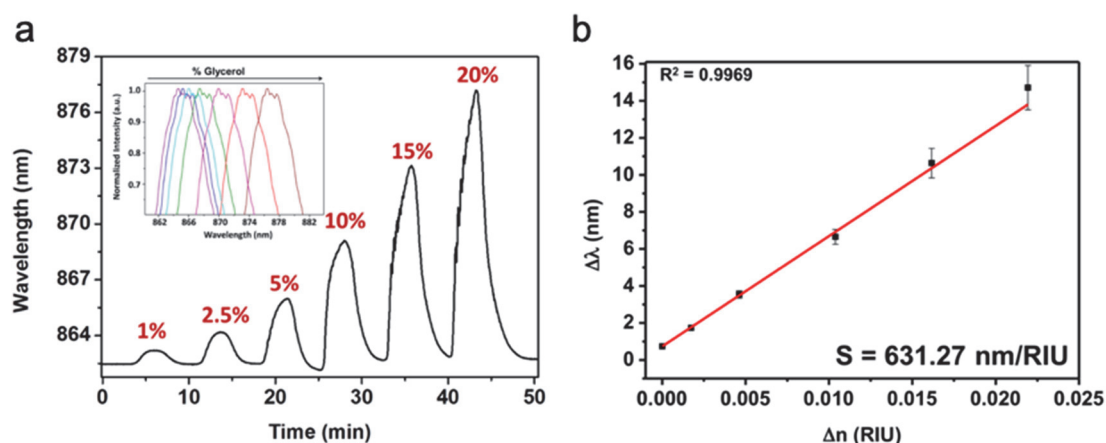
Figure 5.4. Bulk sensitivity characterization. (a) Real-time sensorgram of different concentrations of glycerol, with the inset graph highlighting the spectral shifts of the resonance peak. (b) Bulk sensitivity calibration, where the sensitivity S is determined by the slope of the linear regression equation.

of a linear fitted curve shows the bulky sensitivity of the sensor, which was determined to be 630 nm/RIU (Figure 5.4b). This sensitivity outranges the majority of the state-of-the-art nanoplasmonic biosensors, demonstrating the unique potential of our system to perform single-cell secretion analysis [45], [167], [168].

5.2.3 Surface functionalization for cell capture and cytokine detection

Figure 5.5a illustrates the schematics of the designed surface functionalization. First, we coated the gold chip surface with an anti-fouling self-assembled monolayer (SAM) composed of polyethylene glycol (PEG) derived compounds, preventing binding of non-specific molecules [169]. In particular, a mixture of two kinds of PEGylated alkanethiols was employed, with one carrying a reactive carboxylic functional group (–COOH) and the other nonreactive hydroxyl group (–OH), respectively. The latter serves as a lateral spacer to minimize steric hindrance effects during protein attachment. The reactive carboxylic groups were subsequently activated by the general carbodiimide chemistry (i.e., EDC/NHS activation) that allows covalent binding of molecules presenting terminal amine groups (–NH2). At this point, we co-immobilized a mixture of streptavidin and poly-L-lysine (PLL), both containing a significant amount of terminal amine groups. PLL is a well-known polymer with the positive net charge that acts as an electrostatic force to attach floating cells (negative net charge) [170], avoiding any chemical modification of the cell membrane and therefore ensuring immobilization without affecting the cell physiology. Streptavidin was in turn used for the highly stable and oriented immobilization of biotinylated antibodies (Ab) against the cytokine of interest (IL-2). We tested the efficacy
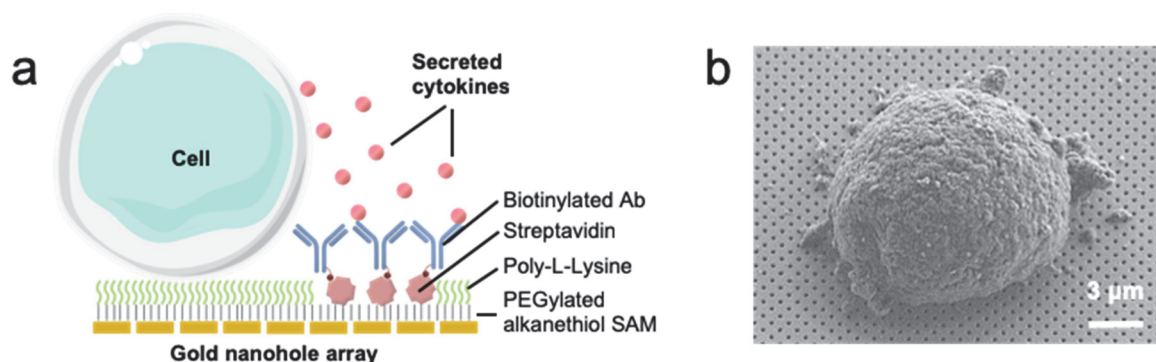
Figure 5.5 Surface chemistry on gold sensor surface and an SEM image showing a single cell attached to the sensor.

of our surface chemistry strategy for both cell attachment and cytokine detection, by depositing a cell suspension sample on the functionalized chip and incubating for 1 h at 37 °C. After carefully rinsing, we confirmed the presence of cells immobilized on the nanohole array surface by scanning electron microscopy (Figure 5.5b).

To evaluate the biosensor sensitivity for cytokine detection, we performed a calibration curve with standard protein samples. Samples spiked with different concentrations of recombinant IL-2 proteins (from 50-1000 pg/mL) were introduced over the functionalized nanohole arrays. We employed a conventional PDMS microfluidic system with microchannels (500 μm wide, 180 μm high) for the sample injection, which was connected to a syringe pump for a continuous buffer flow. As shown in Figure 5.6a, the capturing of IL-2 to the antibodies was depicted by resonance shifting ($\Delta\lambda$) in a concentration-dependent manner. Higher concentrations of IL-2 samples lead to a greater resonance shift, as well as the progression of signals being accelerated with increasing concentrations. The plateau $\Delta\lambda$ values obtained from each sample were then plotted as a function of the corresponding concentrations. By fitting to a nonlinear regression model (Figure 5.6b), we determined the limit of detection (LOD) of our biosensor, which is defined as the concentration with a signal amplitude corresponding to three times the standard
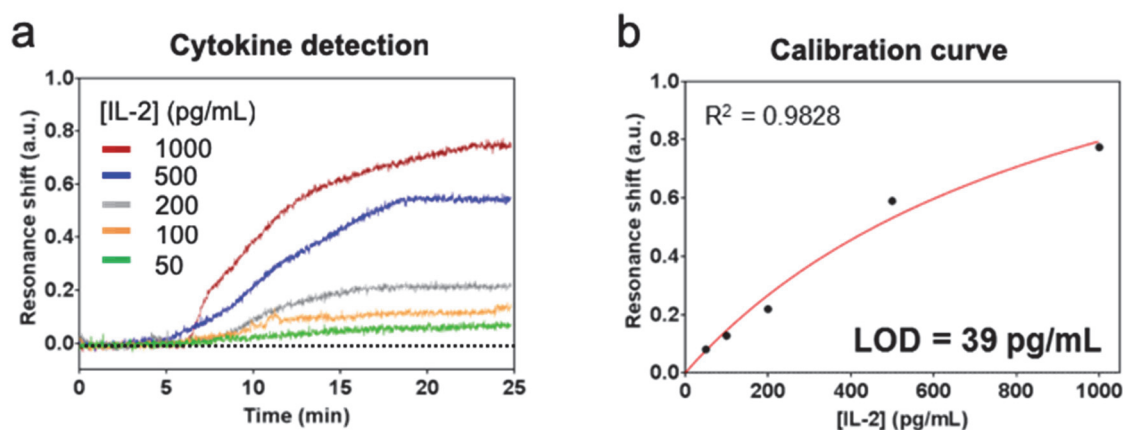
Figure 5.6. Characterization of the nanohole array biosensor for IL-2 detection. (a) Real-time sensorgrams of different concentration of cytokines (IL-2) ranging from 50 pg/mL to 1 ng/mL. (b) Standard calibration curve for direct and label-free detection of IL-2 molecules. Each data point represents the mean value of 3 replicates. The limit of detection (LOD) is determined as the signal corresponding to three times the standard deviation of the blank.

deviation of the blank signal [171]. Based on the background signal we obtained from the zero-spiked sample, we achieved an outstanding LOD of 39 pg/mL (2.6 pM) for IL-2 detection.

5.2.4   Design and characterization of the multifunctional microfluidic system

Renewal of continuous media flow as employed in conventional microfluidic cell assays is not practical for single cell analysis, as it inhibits the accumulation of cell secretions, and thus results in depletion of target molecules. Isolating target cells within an enclosed volume, and minimizing this incubation chamber size would naturally facilitate sensitive biodetection required for single-cell resolution, through minimization of diffusive target loss. However, a number of challenges emerge. The intrinsic property of high gas permeability of thin PDMS membranes enables this material to be ideal for live cell culture. However, this permeability also leads to evaporation of water through the PDMS structure, which can be problematic for long-term experiments. The significant degree of evaporation and subsequent shift in refractive index hampers the nominal operation of the nanohole array biosensor. (Figure 5.7a).

We experimentally verified the detrimental effects of fluidic evaporation through bulk PDMS on sensor reliability with a basic microfluidic channel design placed within a 37 °C environment (Figure 5.7b). The evaporation induced significant drift in the resonance response compared to room temperature with the same relative humidity and under the same illumination
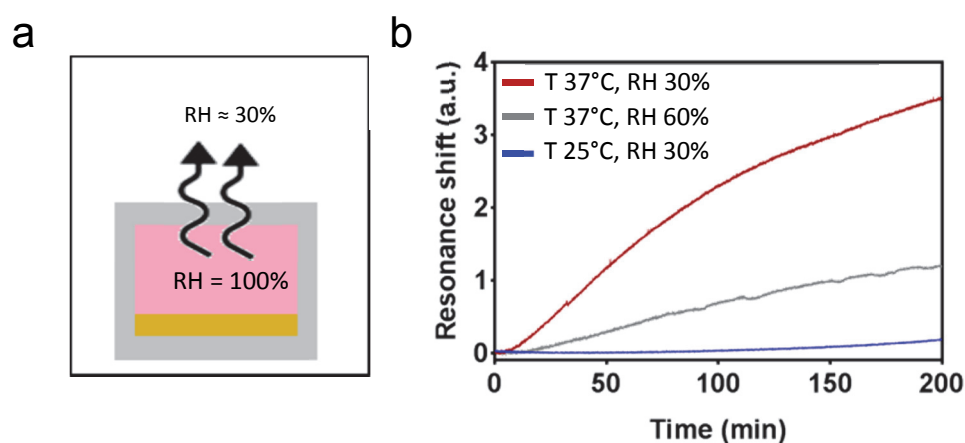
Figure 5.7. Evaporation across PDMS membrane and the resulting optical signal fluctuation. (**a**) Schematic illustration representing the evaporation of water from the PDMS microchamber (RH_{in}) to the surroundings (RH_{out}). (**b**) Baseline drifts of the resonance peak under different conditions surrounding the microchamber with varying temperature and relative humidity.

scheme. Whereas, we obtained a more stable optical readout by supplying doubled humidity surrounding the microfluidics placed in a custom humidity box. This experiment confirmed that relatively high humidity is crucial to prevent evaporation and therefore to facilitate stable optical measurements.

In order to stabilize optical response under cell culture conditions, we have designed a novel multilayered microfluidic system utilizing our recently introduced injection molding fabrication technique (Figure 3.5) [124]. A schematic of this system is shown in Figure 5.8. This system allows an isolated microchamber (length × width × height ≈ 2 mm × 500 μm × 180 μm) with a chamber volume of 180 nL for cell measurements while compensating for
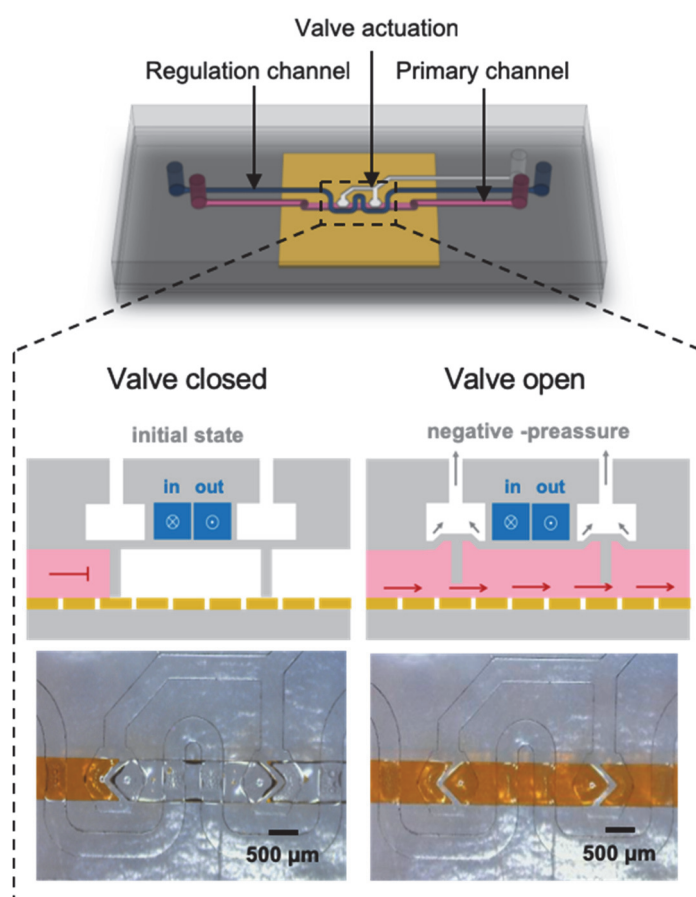
Figure 5.8. Schematic representation of the microfluidic system design. The primary channel for cell injection and culture is highlighted in pink, while pneumatic actuation in white and the regulation channel blue. Zoom-in figures represent the cross-sectional view of the microfluidic system and the valve actuation mechanism. Real pictures of the microfluidic system are shown at the bottom.

vapor loss across the gas permeable PDMS structure. The microfluidic device utilises normally closed pneumatically actuated microvalves to isolate the fluid within the small incubation chamber. The primary channel is fabricated in the bottom layer for simple introduction of cells to the biosensor and potential cell retrieval after analysis. The upper layer incorporates the pneumatic lines and actuation chambers required to actuate the isolating microvalves, and a serpentine hydraulic regulation channel to regulate the local humidity and temperature of the incubation chamber. This is facilitated through a thin PDMS membrane present between the regulation and primary channel.

Evaporation of water occurs due to the vapor pressure difference across the wet and dry sides of a PDMS membrane. Based on the theoretical evaluation (section 3.8), the evaporation rate through a PDMS membrane would mainly depend on the surface area and thickness of the membrane as well as the temperature and relative humidity of the ambient environment. Using this equation, we calculated the evaporation rate versus different environmental parameters, particularly the typical cell culture temperature (i.e., 37 °C). As shown in Figure 5.9a, increasing temperature promotes evaporation. In contrast, elevating the relative humidity on the wet membrane minimizes the evaporation from the incubation chamber, and ultimately reduces to nearly zero at a relative humidity of 100% (Figure 5.9b), which corresponds to the conditions when the regulation channel is filled with water, as shown in Figure 5.9c. At this point, although the vapor loss through the bulk PDMS and dry membranes persist, it is
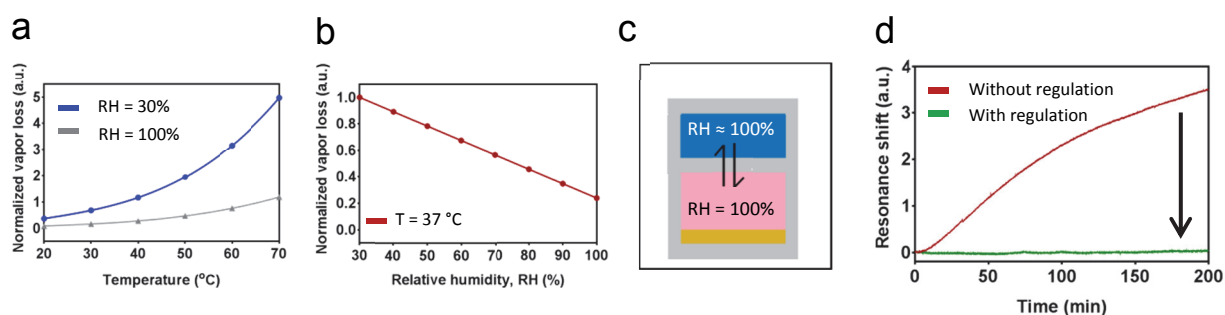
Figure 5.9. Numerical calculations of evaporation across PDMS membrane and the efficiency of new microfluidic device. (a) Numerical calculations of the vapor loss dependency on the temperature at different relative humidity. (b) Numerical calculations of the vapor loss dependency on the relative humidity at 37 °C. (c) Schematic illustration representing the compensation for the evaporation by the regulation channel filled with water. (d) Baseline drift comparison of the sensor signal obtained without regulation (red) and with the regulation system (green) filled with water (100% humidity).

compensated by vapor transfer across the wet membrane driven by resulting vapor pressure difference. This is evidenced by the improved stability of the signals shown in Figure 5.9d.

5.2.5   Real-time analysis of IL-2 secretion from single EL4 cells

After characterization and optimization of our optofluidic biosensor, we examined the performance for direct and label-free single cell IL-2 secretion analysis. IL-2 is one of the essential cytokines that are actively involved in numerous biological activities of the immune system, and it particularly exerts prominent functions in regulating the proliferation, activation, and differentiation of T lymphocytes [172]. Therefore, the dynamic analysis of IL-2 secretion events provides insights to better understand its pathophysiological roles in the immune system as well as its potential applications in disease treatments. We selected EL4 lymphoma cells for our experiments, as these cells are engineered to secrete IL-2 cytokines only upon defined chemical stimulus [173], which represent an optimum IL-2 secretion cell population to evaluate the sensitivity and specificity of our new analytical platform.

To perform the assay, we functionalized the nanoplasmonic chip as described before and assembled it with the multilayer microfluidic system. EL4 cells suspended in cell media were introduced into the primary channel with an ultralow cell density. The pneumatic valves were subsequently closed to stop the flow which resulted in a few isolated single cells being enclosed in the valve-gated chamber (Figure 5.10a). After a short period of incubation at 37 °C to allow firm cell attachment to the nanohole array surface, the optofluidic device was placed in the inverted microscope equipped with a customized incubator box that provides the proper temperature and CO_2 to maintain appropriate cell culture conditions. Afterward, a collimated beam of broadband light illuminated the assembled device at normal incidence. We used a 20x magnification objective to image a single EL4 cell. The transmitted light through the nanohole arrays entered the partially open slit in the spectrometer, forming an optical image recorded by the CCD camera as shown in Figure 5.10b. For illustration purpose, the acquired image was cropped to highlight the location of the cell. By further expanding the recorded image across the wavelength range, we obtained a 1D spectroscopic image (Figure 5.10c), where the spectral information was revealed alongside the exposed region of the nanohole arrays through the slit.

An evident signature in the spectrum appeared at the exact location where the single EL4 cell resides, which resulted from the distinct refractive index of cells. This unique phenomenon allowed us to position a single cell during spectroscopic imaging and define a specific region of interest (ROI) for biodetection. The ROI was subsequently defined in a way that it covers the cell position and the immediate surrounding nanohole array areas functionalized with anti-IL2 antibodies. In particular, we designated a 40-pixel ROI which corresponds to approximately 30 μm on the nanohole array surface. Then, we extracted the corresponding spectrum of the transmitted light, which shows the EOT resonance peak at approximately 860 nm. In order to monitor the capture of analytes in real time, we developed customized MATLAB scripts based on the centroid algorithm [122] to continuously interrogate the resonance peak shifts and to provide a precisely recorded sensorgram. Rather than simply tracking the shifts of maximum peak value, we significantly enhance the signal-to-noise ratio and improve the biosensor sensitivity. We exploited a custom-built MATLAB interface that allows ROI definition, spectrum visualizing, centroid calculation and real-time sensorgram display in a user-friendly manner.

To start the analysis, we injected the chemical stimulus including the Ca^{2+} ionophore ionomycin and the phorbol ester PMA into the primary channel to initiate the activation and secretion of the EL4 cell. Immediately following stimulation, we closed the valve gates to keep a static and controlled volume in the cell microchamber. Then, we commenced the continuous monitoring of the peak position that displays the sensorgram in real time (t=0). As shown in Figure 5.10d, we observed a significant resonance shift emerging at around t=110 min (black curve). The signal increase could be directly attributed to the secretion and in situ capture of the IL-2 molecules. We performed an independent negative control experiment employing the same cell culture environment and analysis conditions but without injecting any external stimuli to verify this phenomenon. EL4 cells are a well-characterized cell line that only secretes IL-2 proteins upon proper activation by the chemical stimulus, so cells in common culture media should not produce any sensor response. As can be seen in Figure 5.10d, the grey line remained stable over the whole analysis duration. The absence of resonance response from the negative control indicates that our biosensor is not only selective for the detection of IL-2 but also repellent to other matrix proteins present in the culture media, avoiding any interference

with the cell analysis. We demonstrated that our innovative lab-on-a-chip system is able to detect protein secretion from a single cell in a precise and accurate manner.
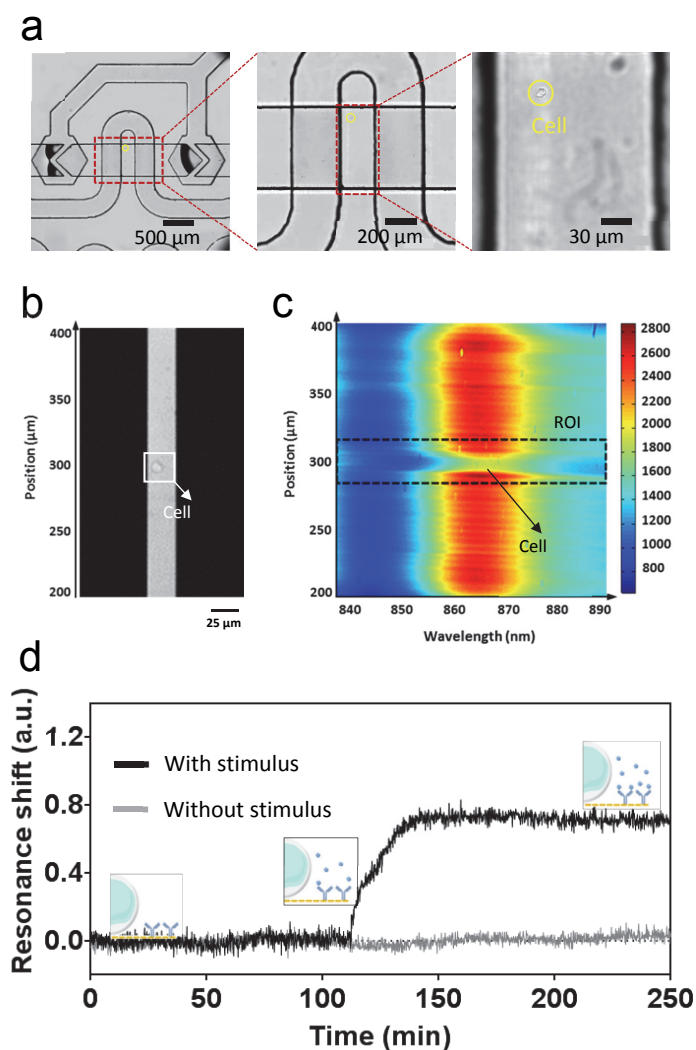
Figure 5.10. Real-time spectroscopic imaging of single-cell secretion. (a) Optical images of an isolated cell encapsulated in the microfluidic chamber. (b) CCD image of a single cell positioned in the center of the partially closed slit in the spectrometer. We cropped the image to highlight the attached single cell. Scale bar: 25 μm. (c) The 1D spectroscopic image shows the EOT peak intensifies around 865 nm (red region) and the spectral signature generated by the cell spot. The region of interest (ROI, boxed with dashed line) for measurement is defined around the cell spot. (d) Real-time sensorgrams obtained from a single EL4 cell secreting IL-2 cytokine upon chemical stimulation (black) and a negative control without the stimulus (grey). Inset figures schematically illustrate the IL-2 secretion and *in situ* capture by co-immobilized antibodies.

5.2.6   Temporal and spatial diffusion analysis of single-cell secretion

To account for the detection flexibility of our nanohole array sensing surface, we further exploited the biosensor to characterize the spatial features of single cell secretion in real time. The design of our nanoplasmonic surface with a uniform surface-spanning nanohole arrays enables the simultaneous and independent monitoring of different ROIs. This feature permits not only analysis and detection of single-cell secretion in real time, but observation of the molecular diffusion along the sensor surface. Following the same procedure described before, we introduced different EL4 cells in the biosensor and enclosed them in the microfluidic chamber. Figure 5.11a shows the spectral signature of an isolated cell attached to the nanohole array chip and enclosed within the valve-gated PDMS microchamber. In order to analyze the spatial diffusion of the secreted cytokines, we defined different ROIs covering the specific cell spot and surrounding areas (Figure 5.11b). In this case, each ROI measures 20 pixels in width and separates 40 pixels (center-to-center) away from each counterpart. Considering the overall optical magnification of the system, each ROI was ~13 μm in width and ~27 μm in period. The ROIs were extracted as independent spectral curves, and the peak centroids were interrogated in real time (Figure 5.11c).

We performed this measurement for three independent single EL4 cells (Figure 5.11 d-f). In all cases, we observed a burst of IL-2 secretion at around 110-120 min post-stimulation from the cell spot, as well as from the adjacent ROIs (ROI 1 and 1'). There was roughly 20 min of delay for the onset of resonance response from ROI 2/2'. The amount of resonance shifts declined from the cell spot outwards, which we attribute to the diffusion process of cytokines in the static media environment. By plotting the endpoint secretion amount of IL-2 (in this case, at 180 min) as a function of different ROIs' locations, we obtained a bell-shaped secretion distribution (Figure 5.11g-i), where the secretion apex occurred within the central cell spot and declined almost symmetrically outwards. It should be mentioned that the label-free biosensing configuration is not able to provide a three-dimensional mapping of the cytokine secretion around the cell, but only the spatial distribution along the sensor surface surrounding the cell. However, the absence of flow in the microchamber and the long-time monitoring might facilitate the secreted cytokines to diffuse effectively across the sensor surface and therefore

enable the quantification. The local IL-2 concentration was calculated by interpolating the relative resonance shift to the calibration curve (Figure 5.6). We found significant differences among the three different cells. Especially the second measurement (Cell 2) showed a higher amount of secreted IL-2 (2500 pg/mL) while Cell 1 and Cell 3 appear to secrete less cytokine. This was also reflected in the spatial diffusion analysis, where we observed a more centralized spatial distribution for Cell 2. This phenomenon reveals the intrinsic heterogeneity in a bulk cell population. Whereas by using conventional methods for cell secretion analysis (e.g.,
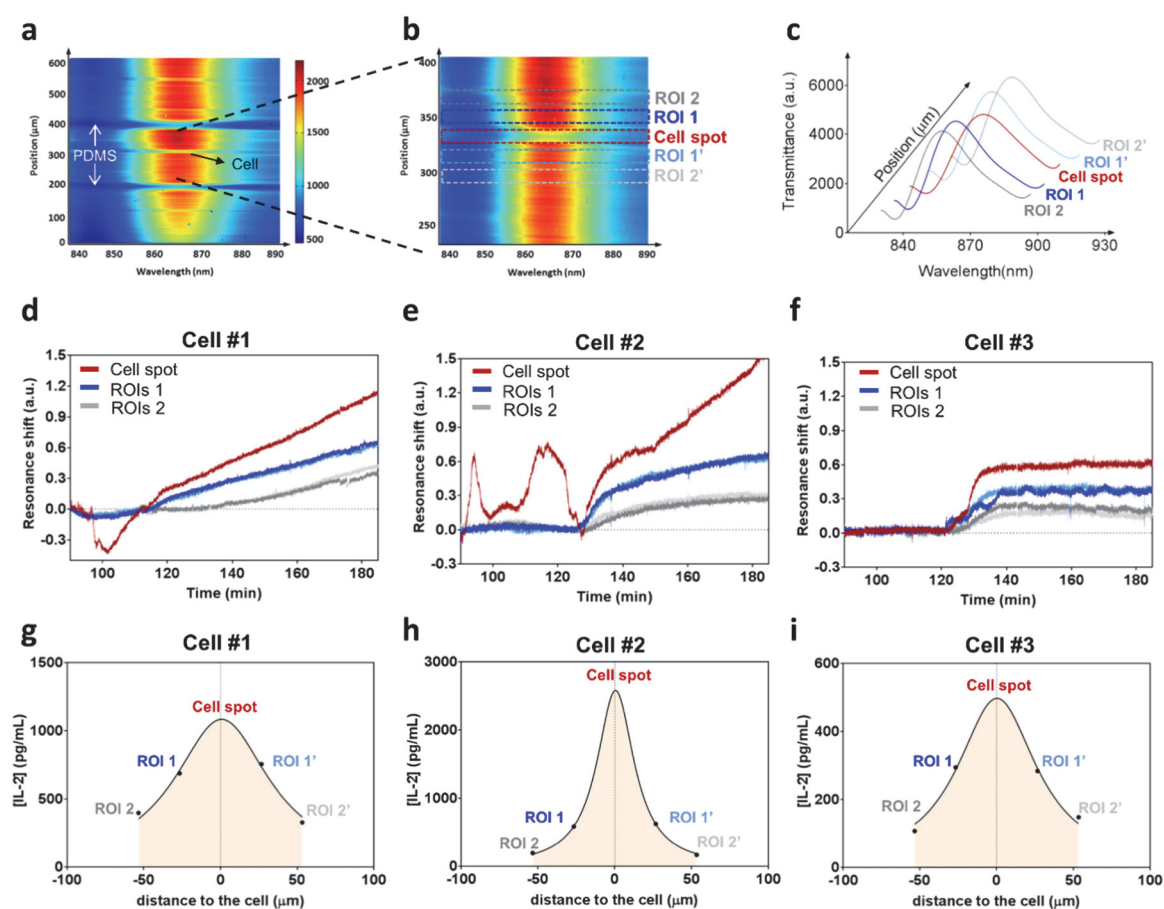
Figure 5.11. Temporal and spatial diffusion analysis of single cells by label-free spectroscopic imaging. (a) Spectral CCD image of the optofluidic system with three isolated cells encapsulated in the microchamber. Strong spectral gaps correspond to the interfacing PDMS of the regulation channel. (b) Zoom-in of the spectral image for the ROIs definition at the center cell spot and surrounding areas. (c) Spectral EOT peaks corresponding to the selected multiple ROIs. The peaks are interrogated simultaneously and independently. (d-f) Independent measurements of IL-2 secretion from 3 different EL4 cells, monitoring the cell spot ROI and surrounding ROIs simultaneously. (g-i) Spatial diffusion analysis of the secreted cytokines: plots correspond to the interpolated concentration of signals acquired for every ROI, fitted to a Gaussian distribution.

ELISA), we would only obtain a single average value for IL-2 secretion at discrete time points. Our single-cell analysis method is promising for accurate observation and precise measurement of protein secretion from individual cells.

It is worth emphasizing that some stochastic noise was observed at the cell spots for Cell 1 and Cell 2 while leaving other ROIs clear of such interference (Figure 5.11d and e). We could attribute this noise to either cell membrane changes or stochastic cellular movement [94]. In order to prove this hypothesis, we performed another experiment where we split the transmitted light beam to simultaneously image the cell with a CCD camera and measure the plasmonic response. We observed the cell movement within an extremely narrow margin (less than 10 μm) before the onset of cytokine secretion (Figure 5.12). This confirms that during the early stage of cell activation, cells undergo certain movements and possible membrane activities. The narrow scope of activity does not influence the detection of cytokines in the surrounding areas. It is important to mention that such phenomena were absent for Cell 3 measurement, while this cell secreted a much lower quantity of cytokines compared to the others. Therefore, the active cell movements could be associated with a higher secretion capacity. Overall, we have demonstrated the superior capabilities of our innovative optofluidic system for the single-cell analysis. This microfluidic-integrated nanoplasmonic biosensor enables a complete analysis of cell activation and secretion from isolated individual cells in a label-free, real-time and user-friendly manner. By expanding the real-time single-cell analysis to a high-throughput configuration with the incorporation of microfluidic cell traps or other strategies [174], we would be able to identify and study cell activation and secretion more efficiently.
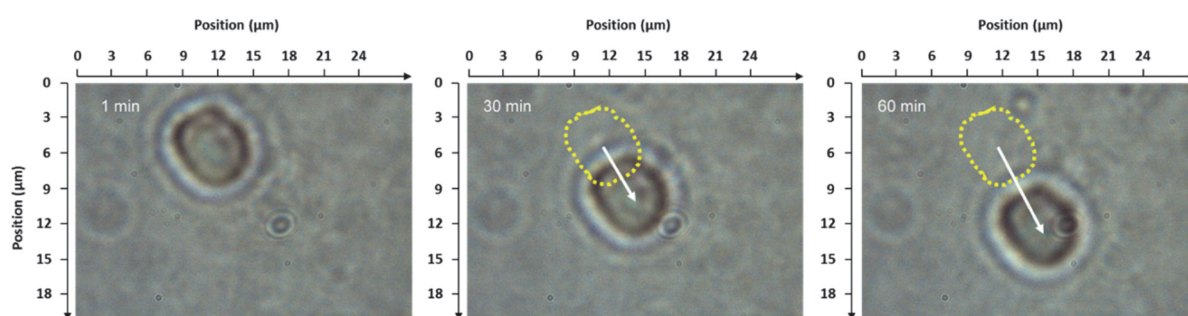
Figure 5.12. Time-lapse images of cell movements. The movement of an individual EL4 cell during the first 60 min of one measurement for IL-2 secretion analysis. The overall movement distance is within 10 μm, which is less than the size of cell spot ROI.

5.3 Conclusion

We introduce a novel design of an optofluidic nanoplasmonic biosensor for single-cell cytokine secretion analysis. This biosensor platform builds upon the ultrasensitive gold nanohole arrays integrated with an easy to fabricate but sophisticated microfluidic system, enabling real-time monitoring of protein secretion from live cultured cells at single-cell resolution in a label-free manner. The integration of pneumatically actuated valve-gates in the microfluidic device generates an isolated chamber with a few nanoliters volume for sensitive cell analysis. In particular, we incorporate for the first time a novel multifunctional microfluidic design involving both regulation and primary microchannels to tackle the common PDMS-mediated evaporation challenge for reliable biodetection. This novel design circumvents the need for conventional oil sealing or providing a rather high ambient relative humidity, achieving a user-friendly and facile biodetection configuration. With this biosensor setup, we achieved an outstanding sensitivity of 39 pg/mL for direct IL-2 detection in complex media. The IL-2 molecules secreted from individual EL4 lymphoma cells can also be directly monitored over several hours without interrupting the cell culture. The uniform arrangement of nanohole arrays over the whole sensor chip surface also allows us to elucidate the spatial distribution of cell secretion. Furthermore, the analysis with different single EL4 cells reveals distinct fingerprints for secretion capacity despite their similar phenotypes. With these capabilities, the proposed nanoplasmonic biosensor system represents a powerful tool to analyze cytokine secretion at the single-cell level in a label-free and real-time manner.

Chapter 6

Label-free affinity analysis of tumor-specific CD8 T cells

6.1 Introduction

Cancer immunotherapies have been identified as a major biomedical breakthrough of the last years and will remain a paramount biomedical landmark in the next decades. This efficient treatment seeks the activation and restoration of the immune system to fight cancer. Most attractive and encouraging advances in cancer immunotherapy have been achieved with the so-called Adoptive Cell Therapy (ACT) [175], [176]. This approach is a highly personalized therapy that involves the identification or genetic engineering of the patient's own tumor-specific immunocytes (i.e. T cells) to provide an enhanced anti-tumor activity. The activation of T cells is essentially triggered by the interaction between the T-cell receptor (TCR) and antigenic peptides presented by the major histocompatibility complex (MHC) in either tumor

cells or antigen-presenting cells (e.g. dendritic cells) [177], [178]. It has been shown that the affinity and binding strength of a TCR to its cognate peptide-MHC (pMHC) correlate with T cell effector functions, and thus the cell-mediated immunity [126], [179]. Therefore, there is a need for robust technology that enables rapid identification of autologous or engineered T cells expressing TCRs specific for tumor-associated antigens (TAAs).

Conventional means for assessing TCR-pMHC binding affinity are based on molecular kinetic studies employing Surface Plasmon Resonance (SPR) technology [180]–[182]. It has become a benchmark technology for label-free and real-time analysis of molecular interaction in research and pharmaceutical laboratories. However, the SPR affinity studies are commonly performed by flowing recombinant TCR molecules over a sensor chip coated with pMHC monomers, namely, three-dimensional (3D) analysis. Apart from requiring expensive molecular synthesis, 3D analysis does not take into account the intrinsic cell membrane physiology (e.g. co-receptors, membrane fluidity). There is strong evidence that binding between soluble monomeric TCR and pMHC cannot reproduce the immunological synapse occurring in cells, as it can only predict high-affinity interactions for T cell activation in clear contrast. Nonetheless, the low affinity-bindings are offen observed in naturally occurring TCRs [183], [184]. Alternatively, the use of reversible fluorescent pMHC multimers (so called NTAmers) has been proposed to study monomeric TCR-pMHC dissociation rates by directly staining the T cell surface [126], [179], [185]. Although this approach accounts for the co-receptor contributions on T cell membranes (e.g. CD8) and has been shown to accurately correlate with CD8+ T cell responsiveness, it is limited to determining only the dissociation rates and cannot evaluate the complete TCR-pMHC binding affinity [185], [186]. Furthermore, the use of expensive fluorescent dyes and the need of high amount of cell clones for flow cytometry truly hampers the throughput of this technique.

Two-dimensional (2D) analysis has been proposed to overcome these limitations. This format measures the TCR-pMHC interaction kinetics at the interface between a live T cell and a surrogate antigen-presenting cell. Compared to 3D analysis, the 2D format has shown an exceptional sensitivity in detecting antigen-specific T cells and dramatically different kinetic parameters when compared to 3D measurements [185]. However, 2D technologies mostly rely on complicated manipulation of individual cells with sophisticated equipment or they require

fluorescent labelling of TCR and pMHC molecules, which could interfere with the native behavior of cells and considerably hamper their application for rapid and efficient screening of T cells.

In this work, we harness the exceptional properties of plasmonic SPR biosensors for label-free 2D TCR-pMHC affinity analysis to develop a multifunctional and biomimetic methodology. We create an artificial cell membrane scaffold on the sensing surface and anchor tumor-associated pMHC monomers as specific probes to capture the target T cells. Artificial membranes formed by planar lipid bilayers have been widely employed for the study of cell biology (e.g. protein-membrane interactions, ion channel regulation) and drug discovery research [187]–[189]. In the field of immunotherapies, planar lipid bilayers have been used to visualize the formation of pMHC clusters during the immunological synapse with live T cells and its direct influence in T cell activation and cytokine secretion [153], [190]. Mooney et al. proved that lipid bilayer scaffolds can mimic antigen-presenting cell membranes and could drastically increase the efficiency of ex vivo immune cell proliferation [191]. We have developed an innovative procedure combining a functional lipid bilayer interface with a multi-parametric label-free plasmonic biosensor for real-time T cell affinity interrogation. Our multi-parametric SPR biosensor can scan the full angular spectrum of the reflected light, enabling the online correction of possible bulk refractive index interferences caused by the whole cell entity. Furthermore, the instrument is equipped with three lasers of different wavelengths for simultaneous analysis, which allows precise structural characterization and validation of the functionalization procedures. We analyze the capture efficiency and structural affinity of CD8+ T cells expressing engineered TCR of incremental affinities for the melanoma antigen NY-ESO-I.21. Our 2D biomimetic sensor enables the identification of tumor-specific CD8+ T cells in a rapid, efficient and accurate manner. We anticipate the implementation of this technique as a valuable step forward in the development of cost-effective personalized therapies against cancer.

6.2 Results and discussion

6.2.1 Multi-parametric surface plasmon resonance (MP-SPR)

Our biosensor is based on a surface plasmon resonance (MP-SPR) system combined with a biomimetic scaffold for enabling live T cell affinity analysis (Figure 6.1). By analyzing the SPR sensorgrams, it is straightforward to extract the kinetic parameters for association and dissociation processes (k_{on} and k_{off}, respectively) and the corresponding affinity constant (K_D) (Figure 6.2c). However, SPR kinetic analyses are generally performed using biomolecules in solution or, in certain occasions, employing immobilized cells to study the interaction of their receptors with target proteins or drugs [192]–[194]. So far, to our knowledge, no studies have attempted the direct affinity analysis of cell membrane receptors employing live cells as analytes.

There remain two main challenges for SPR analysis using live cells: the complexity of capturing the whole cell in flow and the bulk refractive index change occurring simultaneously to the molecular binding. In conventional SPR analysis using soluble biomolecules, bulk artifacts are mostly due to different buffer compositions and can be subtracted from a reference channel. In our case, the target analyte (TCR) is not free in solution but embedded into the
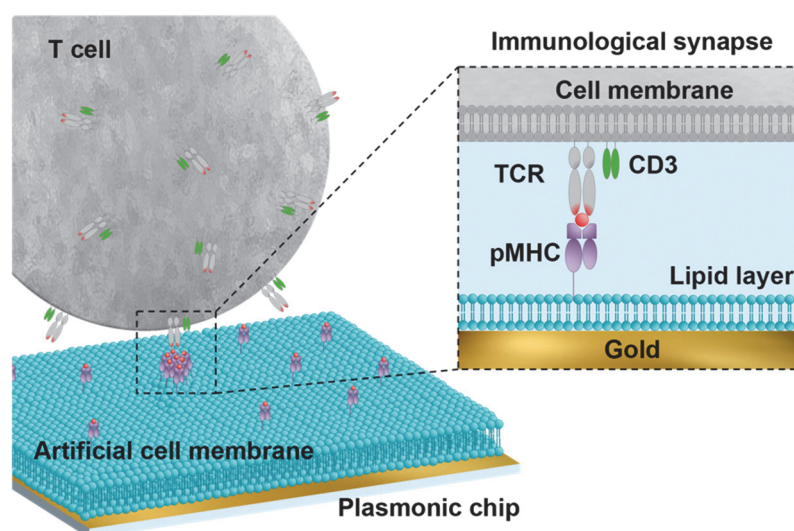
Figure 6.1. Illustration of the biomimetic assay design on a plasmonic chip. A planar lipid bilayer simulates an artificial cell mem-brane with tumor-specific pMHC tethered on the surface; T cells in flow interact with the biosensor interface through their T-cell receptor (TCR).

whole cell entity that inherently produces a change of the dielectric refractive. For subtracting this bulk effect, an intrinsic reference must be considered.

We employ a multi-parametric SPR (MP-SPR) approach based on the full angular scan of light incidence (50°–80°, Figure 6.2a). The main advantage of this technique is the real-time monitoring of not only the SPR angular dip displacements – probing the molecular binding on the surface – but also the total internal reflection (TIR) region (Figure 6.2b). The TIR spectral
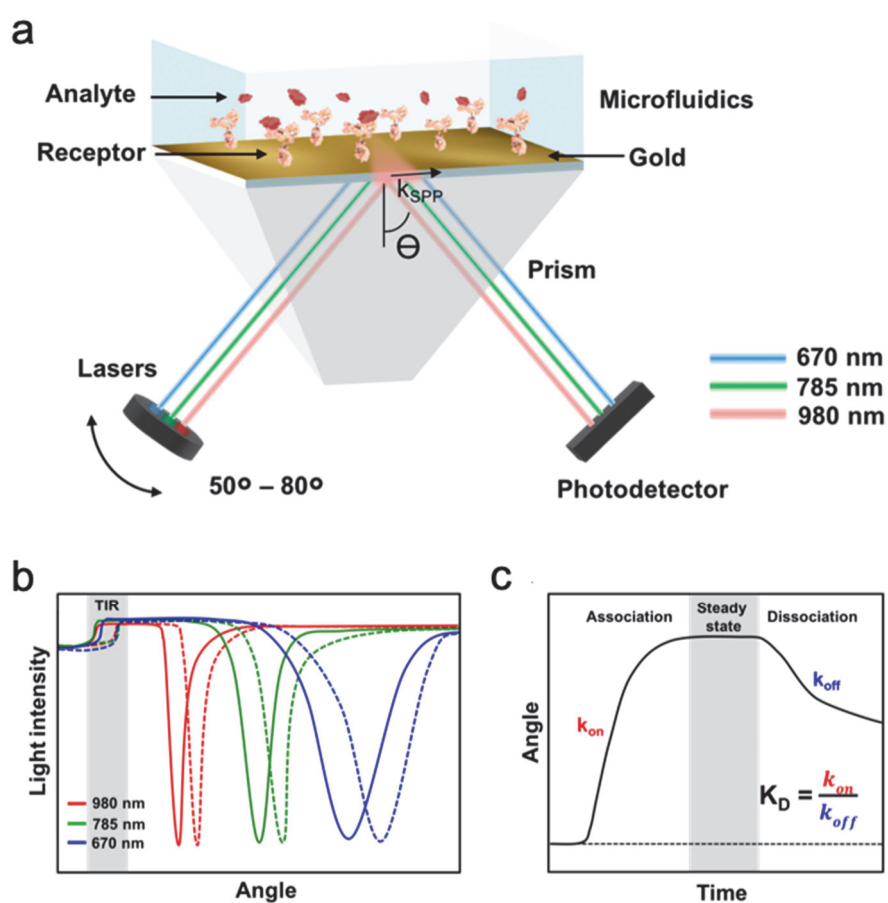
Figure 6.2. Illustration of the MP-SPR analysis principle. (a) Schematics of a prism-coupling SPR system with three-wavelength lasers and angular scanning mechanism. (b) Example of a three-wavelength MP-SPR curve with the total internal reflection (TIR) angle (shaded area) and the SPR dip displacement before and after analyte capture (solid and dashed lines, respectively). (c) Example of an MP-SPR sensorgram with association (capture of analyte), steady state (equilibrium-shaded area) and dissociation (release of analyte).

shape changes with the bulk refractive index, so that it provides an accurate reference for extracting the intrinsic interferences produced by the whole cell entity [195]. With this method, we can obtain real-time sensorgrams revealing solely the kinetic information of the biomolecular interaction. Additionally, our MP-SPR instrument was equipped with three laser sources (wavelengths: 670 nm, 785 nm, 980 nm) to enable a comprehensive and parallel structural characterization of the metal-dielectric interface properties, such as the layer thickness and the refractive index of the materials deposited on the sensor. These measurements are performed by analyzing the full MP-SPR angular spectra (TIR and SPR dip) before and after each binding step (Figure 6.2b). Fitting the curves to corresponding models, it is possible to calculate by numerical iteration the approximate values for the thickness and refractive index or each biochemical layer.

6.2.2 Formation of functional lipid scaffolds on plasmonic surfaces

PEGylated alkanethiol SAMs are considered a standard methodology for gold surface modification, providing a hydrophilic chemical matrix with excellent surface coverage and composition flexibility for incorporating different functional groups ($-COOH$, $-NH_2$, $-biotin$, etc.). This strategy is robust, simple and highly reproducible [196], [197]. However, the immobilization of bioreceptors on a SAM renders static attachment and thus provides no mobility, hampering the formation of molecular clusters or specific receptor-ligand assemblies when contacting the T cell membrane [198]. Such mobility can be accomplished with planar supported lipid bilayers, which are known to present high fluidity and allow natural rearrangements within the surface [153].

In order to measure T cell affinities in a 2D format, the plasmonic sensors were functionalized with different biochemical scaffolds mimicking artificial cell membranes. We have studied three interfaces tethered with different bioreceptors: (i) a functional polyethylene glycol (PEG) chemical matrix in the form of alkanethiol self-assembled monolayer (SAM) as a reference; (ii) a functional supported lipid bilayer (SLB); and (iii) a functional hybrid bilayer membrane (HBM) (Figure 6.3).
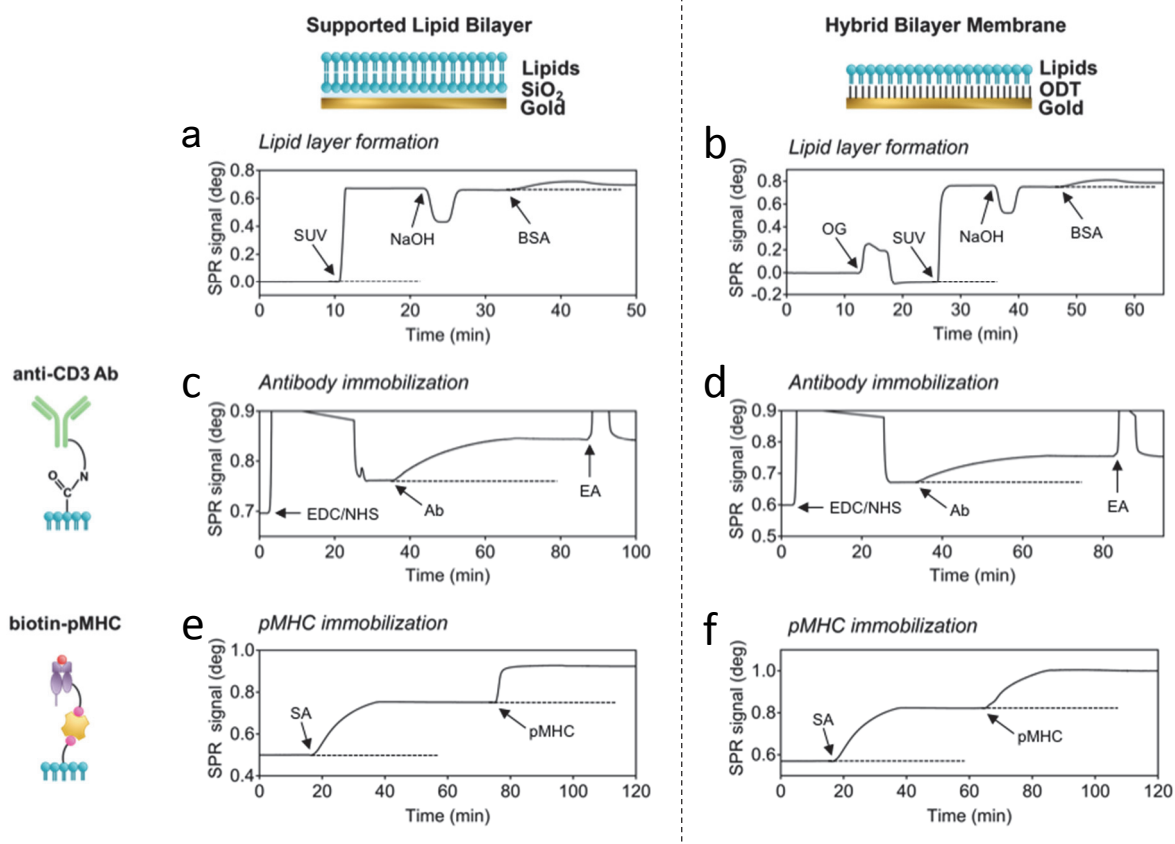
Figure 6.3. Formation and functionalization of supported lipid bilayer (SLB) and hybrid bilayer membrane (HBM). (a) Formation of SLB by disruption of small unilamellar vesicles (SUVs), rinsing with NaOH and blocking with BSA. (b) Formation of HBM by disruption of SUVs on a previously formed alkanethiol SAM and primed with a detergent (octyl β-D-glucopyranoside, OG), rinsing with NaOH and blocking with BSA. (c-d) Antibody immobilization by carbodiimide activation of COOH (i.e. EDC/NHS) and blocking with ethanolamine (EA). (Ee-f) Peptide-MHC immobilization through biotin-streptavidin interaction. Dashed lines illustrate the equilibrium signal reached for relevant functionalization steps.

SLB can be formed on planar substrates by disruption of small unilamellar vesicles (SUV) upon contact with hydrophilic surfaces, like SiO$_2$ [199]. Hence, the common strategy to prepare SLB on plasmonic sensors is pre-coating the gold surface with a thin layer of SiO$_2$ (10-15 nm). Although this technique is effective and relatively simple for SPR sensors, transferring to more sophisticated plasmonic nanostructured surfaces could be problematic (e.g. reducing sensitivity) [189]. The formation of hybrid lipid bilayers could be an alternative solution [200], [201]. HBM is built by modifying the gold surface with a hydrophobic alkanethiol SAM (e.g. octadecanethiol, ODT), which mimics the hydrophobic carbon chains of lipids. When vesicles

are introduced, they disrupt to form the complementary lipid layer on the hydrophobic SAM. A priming step in HBM formation is necessary to assure a well-ordered and clean hydrophobic monolayer in aqueous solution conditions [202]. Two different SUV compositions were employed. With phosphatidylcholine (POPC) as the main lipid component (90% molar ratio), it was combined with either a COOH-functioned lipid (10% DOPS) or a biotin-functioned lipid (10% biotin-DOPE). On these scaffolds we selectively attached two bioreceptors for cell detection and study: CD3 antibodies (anti-CD3 Ab) were chosen as polyclonal capturing elements and immobilized by covalent amide binding to COOH-ended lipid layer; specific peptide-MHC complex (pMHC) monomers for tumor-specific detection were immobilized via biotin-streptavidin interaction. All the functionalization procedures were monitored and characterized with the MP-SPR biosensor as shown in Figure 6.3.

The analysis of the sensorgrams and angular spectra obtained for both SLB and HBM procedures (Figure 6.3a and b) confirmed and validated the formation of stable, uniform, and planar lipid layers on the sensor surface. It can be observed that the SUV disruption occurs as a cooperative binding event (sharp signal increase), revealing that all lipid vesicles rapidly break down and reassemble in the form of a flat layer upon contact with the surface. The rinsing step with sodium hydroxide and subsequent blocking step with bovine serum albumin (BSA) resulted in negligible responses, proving that neither vesicles nor empty spaces remained on the functionalized sensor surface. To further characterize the formation of both membranes, the layer thickness and refractive index of the interface were determined by the MP-SPR instrument. This measurement was carried out by fitting the angular scans obtained from the three wavelengths (670 nm, 785 nm, 980 nm) to their corresponding models (Au-SiO$_2$ layers and Au layer, respectively), and resolving the unknown values (layer thickness and refractive index) by numerical iteration (section 3.6.2). For the SLB, we measured a thickness of approximately 5-6 nm (Table 6.1), while for the HBM, the alkanethiol ODT was measured to be around 2 nm and the lipid monolayer 3 nm (Table 6.2). These values agree well with expected and reported values for the lengths of the biomolecules forming planar bilayers [203], [204].

Table 6.1. Layer thickness for the Supported Lipid Bilayer (SLB).

Layer		Support	Au	SiO₂	Lipid	Buffer
Refractive index (**n**)	670 nm	1.5202	0.17268	1.43378	1.45089	1.33056
	785 nm	1.5162	0.19308	1.45439	1.4502	1.32967
	980 nm	1.5129	0.26648	1.418376	1.4513	1.32513
Attenuation coefficient (**k**)	670 nm	0	3.85987	0.00209	0.00588	0.00169
	785 nm	0	4.78496	0.00628	0.00178	0.00009
	980 nm	0	6.22046	0	0	0
Thickness (**d**, nm)		∞	52.10	**10.99**	**5.86**	∞

Table 6.2. Layer thickness calculated for the Hybrid Lipid Bilayer (HLB).

Layer		Support	Au	ODT	Lipid	Buffer
Refractive index (**n**)	670 nm	1.5202	0.17207	1.4503	1.4496	1.33086
	785 nm	1.5162	0.19278	1.46258	1.45037	1.32897
	980 nm	1.5129	0.26646	1.44698	1.4508	1.3251
Attenuation coefficient (**k**)	670 nm	0	3.86206	0.00227	0.00603	0.00175
	785 nm	0	4.78498	0.00646	0.00687	0.0001
	980 nm	0	6.22043	0	0	0
Thickness (**d**, nm)		∞	54.29	**1.95**	**2.88**	∞

6.2.3 Polyclonal detection of human T cells in real time

To demonstrate the feasibility of our biochemical matrices for the capture and detection of T cells, we functionalized the three different scaffolds (PEGylated alkanethiol SAM, SLB, and HBM) with anti-CD3 antibodies (Figure 6.4). Human SupT1 cells transduced with wild-type TCR specific for the HLA-A0201/NY-ESO-I157-165 pMHC complex were used. The antibodies target a membrane cell receptor complex (cluster of differentiation 3, CD3) expressed in T cells that serves as a co-receptor with TCR for T cell activation. Anti-CD3 antibodies are widely employed as markers and biorecognition elements for the identification of polyclonal T cells with high efficiency and reliability [191]. Antibody immobilization was carried out by covalent binding of their amine terminal groups (e.g. Lysine residues) to the –COOH groups exposed on the SAM, SLB, and HBM. This well-known procedure requires the activation of carboxylic groups via carbodiimide intermediate (EDC/NHS) to form a highly

stable amide link with the biomolecule (Figures 6.3c and d). Later, the unreacted active groups can be deactivated with ethanolamine.

In order to optimize the interface and assay conditions for the cell capture, several factors were considered. Due to the large size of mammalian cells (10-15 μm), we employed a low molar ratio of COOH functional groups for all the biochemical matrices (10%). It has been shown that the relatively low density of antibodies on the surface greatly facilitates the detection of large analytes, such as cells or pathogens [121]. Flow conditions, temperature, and dilution buffers were also thoroughly defined for the analysis. Cell samples were collected from culture media and resuspended in ice-cold Krebs buffer containing 3 mM EDTA. This buffer guarantees a sufficient cell dispersion in solution, avoiding possible cell aggregations while ensuring sufficient ionic strength and glucose content. Low buffer temperature prevents the internalization of membrane receptors [205]. For cell measurements, 250 μL samples were introduced and flowed over the sensor surface at 10 μL/min, followed by subsequent rinsing with the same buffer at the same flow rate. The sensorgrams obtained for cell capture at different cell densities with the three different scaffolds are shown in Figure 6.4 (b-d). In all three cases, we obtained a limit of detection of approximately 500 cells/mL. This high sensitivity already demonstrates that the designed sensing interfaces could be extremely valuable for direct cell detection, isolation, and analysis. Compared to the state-of-the-art, it is worth mentioning that very few works have reported the real-time detection of mammalian
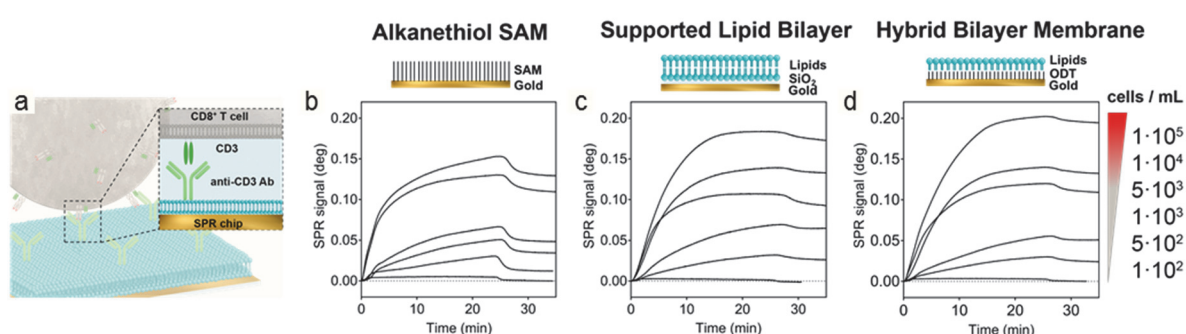
Figure 6.4. Polyclonal cell capturing and detection on the different functionalized surfaces. (a) Illustrative scheme of a lipid membrane functionalized with anti-CD3 antibodies capturing a CD8+ T cell. Wild-type CD8+ T cell attachment to anti-CD3 antibodies immobilized on (b) an alkanethiol SAM, (c) a SLB, and (d) a HBM. All sensorgrams show sequential injections of cell samples at different densities: 10^2-10^5 cells/mL.

cells with plasmonic biosensors, which exposes the evident difficulty and challenges of such process mainly related to mass transport and the complexity and delicacy of live cells [206]. To our knowledge, most recent SPR biosensors using cells as analytes do not show detection limits below 10^4 cells/mL [205], [207]–[209]. With our strategy, we can detect up to 2 orders of magnitude lower concentrations.

Differences in the MP-SPR sensorgrams revealed contrasting behaviors of cell capturing when employing a conventional static SAM or the planar membrane scaffolds. It can be noticed that both SLB and HBM provided significantly higher sensitivity for cell detection, resulting in larger SPR responses for high cell densities especially. This might be attributed to the preference of cells for attaching to biomimetic matrices and also to antibodies immobilized on fluidic membranes with better ability to rearrange on the surface and accommodate a higher number of cells. Interestingly, distinct sensorgram shapes were observed during the dissociation phase. For SAM measurements, the signal decrease after reaching the steady state was qualitatively higher than for SLB or HBM. This effect could reflect the dissociation and washing of non-immobilized cells on the sensor surface, confirming that more cells are captured by functional artificial membranes and the attachment is more efficient.

6.2.4   Tumor-specific detection of human T cells in real time

An attractive and extremely relevant biomedical application for our interface biosensor design is the detection and analysis of tumor-specific CD8+ T cells. The real-time capture of specific T cells in a label-free plasmonic sensor would enable to analyze the kinetics and affinity of intact T cells for tumor-associated antigens, without any chemical or mechanical interference. To accomplish this, instead of functionalizing the biochemical matrices with anti-CD3 antibodies, which target the majority of T cells, we immobilized synthetic biotinylated HLA-A0201 major histocompatibility complex (MHC) monomers loaded with the NY-ESO-I157-165 antigen (Figure 6.5a). Besides, the CD8+ SupT1 cells were genetically transduced with the wild-type TCR isolated from a melanoma patient and recognizing this specific HLA-A0201/NY-ESO-I157-165 complex [125]. Note that the previous measurements with anti-CD3 antibodies were performed with these same cells. To facilitate pMHC immobilization, the

monomers were enzymatically biotinylated on the heavy chain in such a way that the tag does not interfere with the peptide recognition site and enables a simple attachment via biotin-streptavidin interaction. In our case, the procedure generally consisted in forming a biotin-functional layer – either with biotinylated PEG alkanethiols for the conventional SAM matrix or by using biotin-DOPE lipid in the SUV composition of the lipid membranes. Then, streptavidin molecules were attached to the scaffolds and the remaining available sites were used to incorporate the biotinylated pMHC monomers (see Figure 6.3e-f). The biotin density of the three different biochemical matrices was also adjusted to minimize steric hindrance issues for cell capturing, employing only 10% molar ratio of the biotinylated reagents.

Adopting the conditions previously optimized for anti-CD3 detection (e.g. flow conditions, temperature, and buffer), CD8+ SupT1 cell samples at different densities were measured with the MP-SPR biosensor (Figure 6.5b-d). The first and more significant difference observed when comparing to CD3 targeted assays is the relatively lower signals obtained for tumor-specific capturing (4-6 times lower). This result is not surprising as the affinities between TCR and pMHC are indeed weaker in nature (i.e. in the μM range). To confirm cell binding to pMHC, we also acquired optical microscope images of gold chips selectively modified with pMHC after incubation with SupT1 cell samples (Figure 6.6). The images revealed that the cells effectively contact and bind to the pMHC functionalized spots while no cells attached to the regions without the specific pMHC. It is important to notice though that the dissociation phase
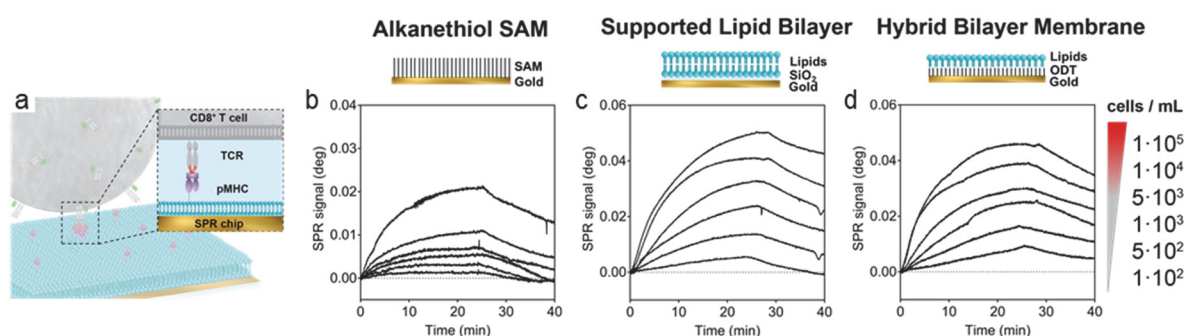
**Figure 6.5. Tumor-specific cell capturing and detection on the different functionalized surfaces**. (a) Illustrative scheme of a lipid membrane functionalized with pMHC monomers capturing a CD8+ T cell. Wild-type CD8+ T cell attachment to specific pMHC immobilized on (b) an alkanethiol SAM, (c) a SLB, and (d) a HBM. All sensorgrams show sequential injections of cell samples at different densities: 10^2-10^5 cells/mL.

in these sensorgrams is clearly different to the polyclonal capturing signals. The interaction between T cells and pMHC-functional layers is reversible, indicating that after association and equilibrium, the immune cells are being released steadily with the continuous flow. This observation agrees with the biological analysis reported in the literature, stating that a relatively quick contact between wild-type TCR and specific peptides expressed in antigen-presenting cells is sufficient for triggering T cell signaling [126]. Yet, both the study of association and dissociation kinetics are crucial to determine T cell responsiveness.
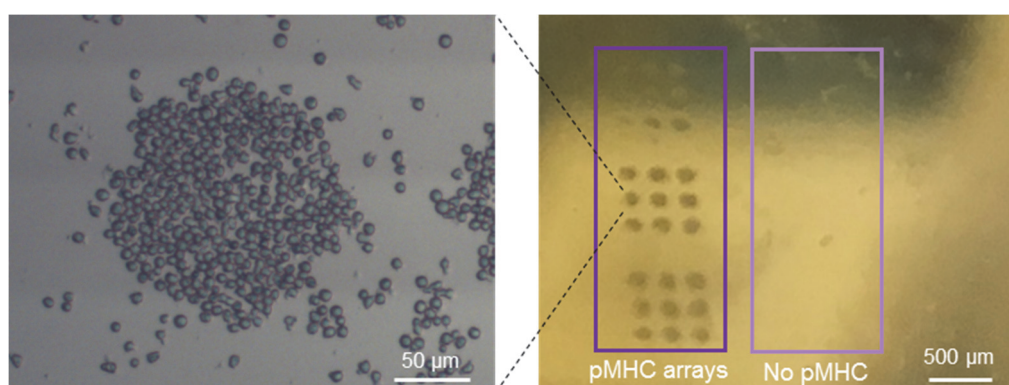
Figure 6.6. Optical image of SupT1 cells attached to the pMHC-patterned gold substrate.

6.2.5 Structural affinity analysis of tumor-specific T cells expressing NY-ESO-I-specific TCR of incremental affinity

After optimizing and evaluating the sensitivity for in-flow cell capturing with our biomimetic scaffolds, we carried out the label-free affinity analysis of tumor-specific human CD8+ T cells in real time and 2D configuration using a plasmonic biosensor. We characterized the kinetics of several genetically engineered T cell variants expressing HLA-A0201/NY-ESO-I-specific TCRs with different affinities, namely CD8+ SupT1 cells transduced with the wild-type TCR (WT) isolated from a melanoma patient, a high-affinity (DMβ) and a low-affinity receptor (V49l) designed in silico and validated by SPR, and untransduced SupT1 cells (T1ϕ) as negative control [125], [126]. The four cell variants were measured with both biomimetic matrices, the SLB and HBM functionalized with the corresponding pMHC (Figure 6.7).

At first glance, the sensorgrams already showed clear differences in the cell affinity for the functionalized surfaces. Compared to the WT cells (Figure 6.7 c-d), the signals obtained for the DMβ variant reached higher values for all cell concentrations (Figure 6.7 a-b), which can be attributed to a higher number of cells attaching to the sensor. Besides, it can be observed that cell dissociation in DMβ sensorgrams occurs at a much slower rate. On the other hand, T1ϕ cells, which do not express any TCR, did not attach to the surface and therefore MP-SPR signals were negligible (Figure 6.7g-h). These negative-control sensorgrams also demonstrate the excellent specificity and selectivity of our interface design, avoiding undesired cell sedimentation and non-specific binding. Special focus worth to be placed on the V49l experiments (Figure 6.7e-f). This engineered TCR has very low affinity for the HLA-A0201/NY-ESO-I complex and therefore represents a critical challenge for the detection and interrogation of very low affinity T cells, like CD4 T cells. Indeed, 3D affinity analyses of such receptor by conventional SPR usually fail, lacking enough sensitivity for the detection [125]. Our results show that the combined use of MP-SPR, the biomimetic interfaces and the whole T cell as analyte enable the detection of the low-affinity lymphocytes and subsequent 2D kinetic analysis. Finally, it should be mentioned that no significant differences were observed between the SLB and the HBM strategies. These results indicate that our hybrid bilayer membrane acts alike the conventional supported bilayers, probably with similar fluidity and providing the cells with a microenvironment that simulates the contact with another cell surface. Our experiments are introducing a novel methodology that can be readily applied to more sophisticated nanoplasmonic sensors, with higher sensitivities, and compatibilities for integration in lab-on-a-chip devices and multiplexing.

To ultimately demonstrate the important capabilities of our technique for 2D structural affinity analysis of tumor-specific immune cells, we determined the kinetic parameters of the interactions occurring between pMHC-functionalized membranes and the different T cell variants. The MP-SPR sensorgrams were fitted to a Langmuir-based function, assuming a 1:1 specific interaction. In order to confirm and validate our results with standard technologies, we extracted the k_{off} parameter for each set of measurements and compared with previous results obtained with reversible fluorescent pMHC multimer (NTAmer technology using flow cytometry) [126] and 3D molecular SPR analysis [125] (Table 6.3). As expected, our kinetic

analysis significantly differs from the 3D measurements. Instead, the values are comparable to the ones obtained by more novel and reliable methodologies (i.e. NTAmers) that take into account the cell membrane organization and contribution. By analyzing the strength of the interaction between molecular complexes (i.e. TCR and pMHC clusters) rather than isolated molecules, we include avidity factors in the measurement, which increases the accuracy of the study [210]. Due to conceptual restrictions in the numerical analysis, the values extracted for the k_{on} and K_D parameters in our case should not be quantitatively compared with other SPR measurements. These parameters highly depend on the exact molar concentration of the target analyte, which we could not determine accurately in our laboratory since we employed the whole live cell as analyte. However, the qualitative study of the sensorgrams agrees with the TCR designs and affinities expected for the different cell variants. The remarkable sensitivity of our device enables the binding parameter analysis of very low affinity T cells that seem to play an important role in immune mediated responses [211]. In this regard, further investigation and evaluation would be necessary to exploit the plasmonic sensing capabilities not only for simple molecular analysis but also for the interrogation and screening of live cells.
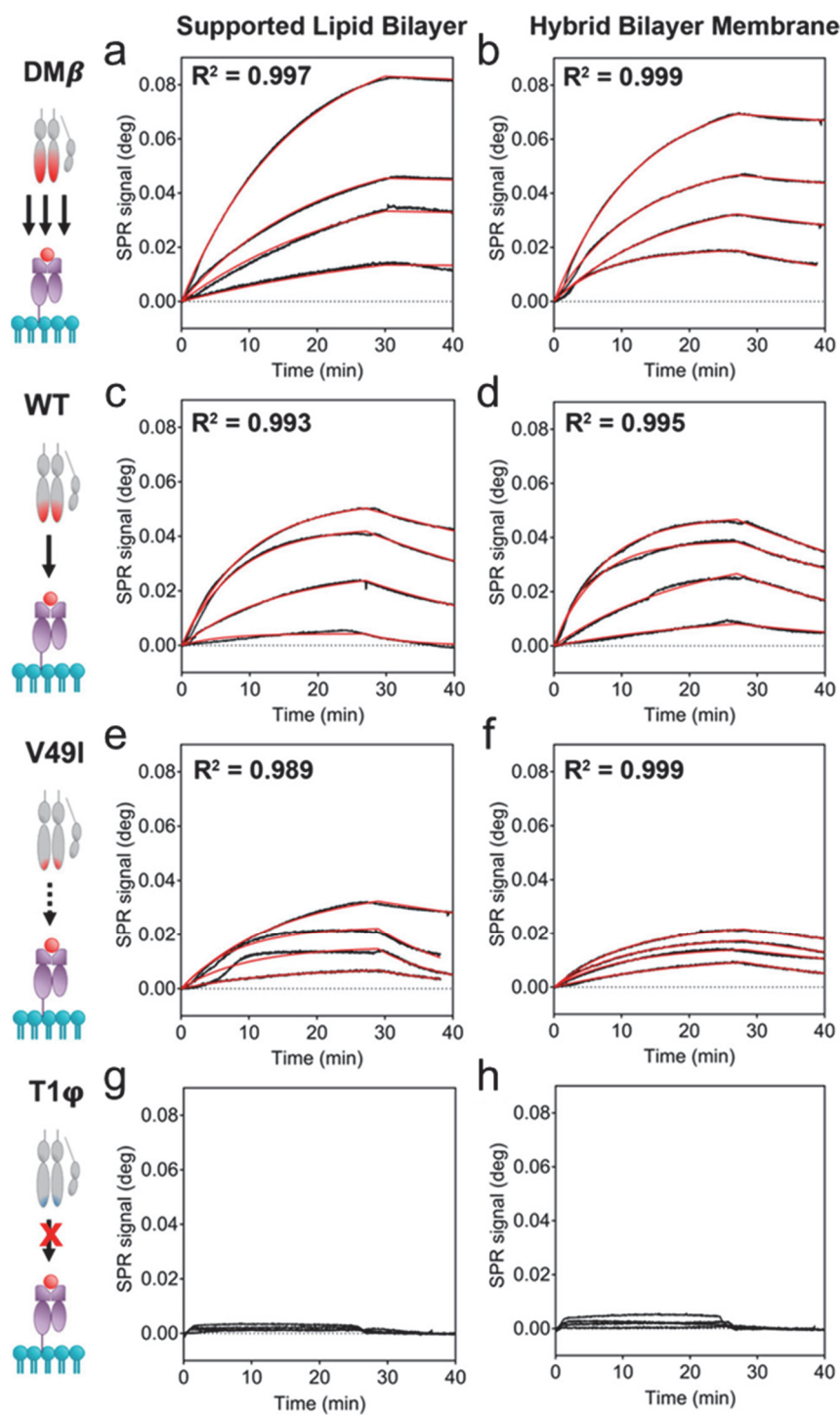
Figure 6.7. Two-dimensional structural affinity analysis of tumor-specific CD8+ T cells. Cell capture and analysis on pMHC-functionalized SLB and HBM with (a-b) DMβ T cells, (c-d) Wild-type (WT) T cells, (e-f) V49l T cells, and (g-h) Negative control tests with T1φ T cells. All sensorgrams show the response of different samples with densities: 10^2, 10^3, 10^4, 10^5 cells/mL (bottom to top). Graphs are plotted with the same axes scale for easier comparison. Red lines correspond to the model fitting for kinetic parameters determination.

114

Table 6.3. Kinetic parameters for NY-ESO-1 specific TCR variants.

TCR variants	3D SPR analysis[a]	Fluorescent NTAmers[b]	2D MP-SPR analysis	
			SLB	HBM
	k_{off} (x10^{-2} s^{-1})	k_{off} (x10^{-2} s^{-1})	k_{off} (x10^{-2} s^{-1})	k_{off} (x10^{-2} s^{-1})
DMβ	4.5	0.78	0.57	0.63
WT	23.0	4.08	3.65	3.81
V49l	n.a.	21.21	17.83	19.54

n.a.: not applicable
[a]SPR measurements reported in [125]
[b]Fluorescent NTAmer measurements reported in [126]

6.3 Conclusions

We have introduced a simple but highly efficient strategy for creating functional artificial cell membranes on plasmonic surfaces that enable tumor-specific cell detection, screening, and affinity analysis with an excellent sensitivity and reliability. We have demonstrated the direct and label-free interrogation of whole and intact cells for determining the TCR structural affinity for a relevant melanoma antigen. The multi-parametric SPR biosensor enables the determination and evaluation of the 2D kinetic parameters of TCR-pMHC interactions employing whole intact cells as analytes. By functionalizing the plasmonic surface with planar lipid layers tethered with specific pMHCs, we enhanced the sensitivity for cell capturing, providing in turn an appropriate microenvironment for reliable analysis. This method with its ability to study TCR-pMHC affinities can be a valuable tool in cell therapy design and manufacturing processes.

Chapter 7

Conclusion and outlook

This thesis demonstrates, for the first time to our knowledge, the potential of plasmonic nanohole arrays as label-free biosensor for real-time cell secretion analysis. Plasmonic nanohole arrays hold exceptional capability for label-free biodetection due to the enhanced optical transmission and straightforward implementation into both optical microscopes and point-of-care devices. However, numerous label-free biosensors including the nanoholes have rarely reported their detection applications involving live cells due to the rigorous conditions required to maintain cell viability across the entire monitoring and minute quantity of molecules secreted by cells.

7.1 Summary

7.1.1 Advantage of plasmonic nanohole arrays for cell secretion analysis

Thanks to the straightforward implementation for nanohole array sensors in commercial microscopes, cell culture conditions can be readily supplied by on-stage cell incubator. In chapter 4, an initial proof-of-concept study was accomplished by incorporating microfluidic modules for cell culture and biosensor. Microfluidic techniques have been widely employed in biochemistry assays, such as cell culture, mass transport, and optofluidic measurements. In this study, cancer cells grow in a typical serpentine microchannel design as the cell module, and the biosensor chip is assembled with microfluidics as the detection module. By connecting these two modules, the cell-conditioned media can be continuously transported over the biosensor surface. The

selectivity and specificity are guaranteed by functionalizing the surface with specific surface chemistry. We are able to reach an outstanding sensitivity of 145 pg/mL for VEGF detection in cell media. Additionally, results obtained from the nanoplasmonic biosensor agreed well with those measured by the gold-standard ELISA assay, which verify the reliability of this novel label-free methodology. Furthermore, the pattern of nanohole microarrays fabricated on free-standing membranes generates distinct sensor units and enables a promising multiplexed format where versatile surface chemistry can be realized on individual units. With these capabilities, this label-free plasmonic nanohole array biosensor represents a powerful analytical tool to monitor protein secretion from live cells in a real-time manner.

7.1.2 Analysis from multiple cells to a single cell

Taking into account of the single-cell heterogeneity in multiple cellular properties, we have upgraded the format of nanohole arrays from individual sensor units on free-standing membranes to nanoholes over the whole wafer. The large-scale arrangement of the nanostructures eliminates the spatial restraint for surface chemistry and cell positioning, which enables facile analysis using single-cells. In addition, we have introduced a novel design of an optofluidic biosensor integrating a multifunctional microfluidic system for reliable single-cell cytokine secretion analysis.

The microfluidics contains pneumatically actuated valve-gates in the cell-loading channel, generating an isolated microchamber with a volume of few nanoliters for sensitive single-cell analysis. In particular, we incorporate a regulation channel layer over the principle cell channel to tackle the intractable issue of PDMS-mediated liquid evaporation. This is particularly critical as the vast water evaporation from the subnanoliter cell chamber is fatal for cell survival and especially reliable optical readout. This novel microfluidics design circumvents the need of anti-evaporation oil sealing or providing a rather high ambient relative humidity, creating a neat and user-friendly optofluidic configuration. With this biosensor setup, the secretion of IL-2 molecules from single EL4 lymphoma cells can be directly monitored without interrupting the cell culture. Spatial mapping of the secretion event is also realized by analyzing the IL-2 binding at different locations around the individual cell due to the uniform distribution of

nanoholes. Therefore, the real-time single-cell secretion analysis has been realized in both temporal and spatial manner.

7.1.3 Analysis within mimicking cellular environment

Despite exploring the biosensor's detection potential incorporating live cells, one key factor should not be ignored, which is the cellular microenvironment, or the so-called cell niche. It is now widely acknowledged that recreating a biomimicking cell niche is essential for *in vitro* studies. Theoretically, all types of cell-cell interactions occur at lipid membrane interface, especially in adoptive immunity (i.e., antigen recognition) and adoptive cell transfer-based tumor immunotherapy. Therefore, we have introduced a straightforward strategy by creating artificial cell membranes on the plasmonic surface. The supplementary lipid layer can resemble the membrane of antigen-presenting cells for TCR-pMHC recognition studies. Thus we applied this biomimicking sensor surface for tumor-specific T cell affinity analysis with an excellent sensitivity and reliability.

The intact live cells were employed as analytes for determining the TCR affinity to a relevant melanoma antigen in a direct and label-free manner. A multi-parametric SPR biosensor was used to evaluate the 2D kinetic parameters of TCR-pMHC interactions. This method with its ability to study TCR-pMHC affinities can be a valuable tool in cell therapy design and manufacturing processes. For instance, it can be used to evaluate newly engineered TCR designs with selected cell lines. By selecting suitable membrane receptors, the complete profiling of cell functionality, specificity, and activity can be obtained. In this regard, it would be powerful to eventually extend the method for operation in more complex matrices such as blood. This would for example enable the direct capture and isolation of tumor-specific primary T cells from peripheral blood samples, which could be readily employed for immunotherapy development.

Additionally, incorporating single-cell measurement capabilities could enable more accurate analysis and identification of anti-tumor activity and the possibility to decipher the underlying mechanisms of immunological functions. For such future directions, it will be necessary to carefully optimize surface chemistry, microfluidics, and assay conditions to mitigate non-

specific binding as well as introduce new plasmonic sensing schemes to improve the overall device sensitivity. The upcoming synergy between nanotechnologies and bioengineering methods has the potential to revolutionize the field of personalized therapies for cancer, auto-immune disorders, or other critical diseases.

7.2 Challenges and perspectives

7.2.1 Enlarge the analysis scale for single cells

The excellent ability of plasmonic nanohole arrays to decode dynamic protein secretion (cytokine or growth factor) from live cultured cells has been demonstrated in this thesis. By minimizing the detection volume with microfluidics, the real-time analysis resolution has been enhanced up to single-cell level, leveraging the applicability of this plasmonic biosensor. Single-cell analysis has shown remarkable potential for understanding fundamental biology, adoptive cell therapy and developing personalized medicine. Nonetheless, a sufficient and vast throughput to analyze hundreds to tens of thousands of single cells is indispensable to distinguish the candidate cells. Such enormous scale requires both a large-scale arrangement of individual cells and a multiplexed high-throughput readout for label-free biodetection.

How to individually separate the cells

Numerous techniques have emerged to enable efficient generation and arraying of single cells for downstream assays[212]. Most of the reported techniques have exploited microfluidics-based systems, such as droplet microfluidics [213], [214] and physical cell traps [215] embedded in channel-based microfluidics. These systems are often designed as sophisticated network of fluidic conduits which require fine tuning of geometrical and hydraulic factors to maximize the yield of single-cell units. Another widely-employed and more user-friendly method exploits gravity-facilitated single-cell deposition in subnanoliter structures (e.g., microwells, microgrids) [150], [153]. In this configuration, the tedious fluidic manipulation is replaced by simply dispensing cell suspension on top of the cell-trapping structures followed by gravity-driven cell deposition into the trap. However, due to the limitation of manufacturing and handling, the geometrical feature of one single trap is a few times bigger than the size of a single cell. In addition, considering the various waiting duration for cell deposition, the yield

of structures containing a single cell mostly follows a Poisson distribution. In the work described in chapter 4, single cells were obtained by high dilution of cell suspensions and placing a small number of cells across a relatively large area. The randomness as well as the complicated multilayered microfluidics impede further enlargement of the analysis scale and easy handling of the entire device.

The liquid dispensing technique (described in section 3.5.3), however, has opened up an alternative methodology to separate the cells. By integrating high-resolution real-time imaging algorithm, the camera responsible for monitoring droplet formation can be employed for single-cell distinction. As shown in Figure 7.1a, the algorithm segments the tip of liquid dispensing nozzle into two zones: zone 1 for single cell ejection and zone 2 for cell sedimentation. The ejection zone contains the volume of only a single droplet, while the sedimentation zone acts as a buffer region to prevent extra cells from sedimenting into the ejection zone during the nozzle movement. A single cell will be dispensed at the user-defined locations only when **zone 1 contains one cell** and **zone 2 contains no cell** (Figure 7.2b). In this way, the yield of single
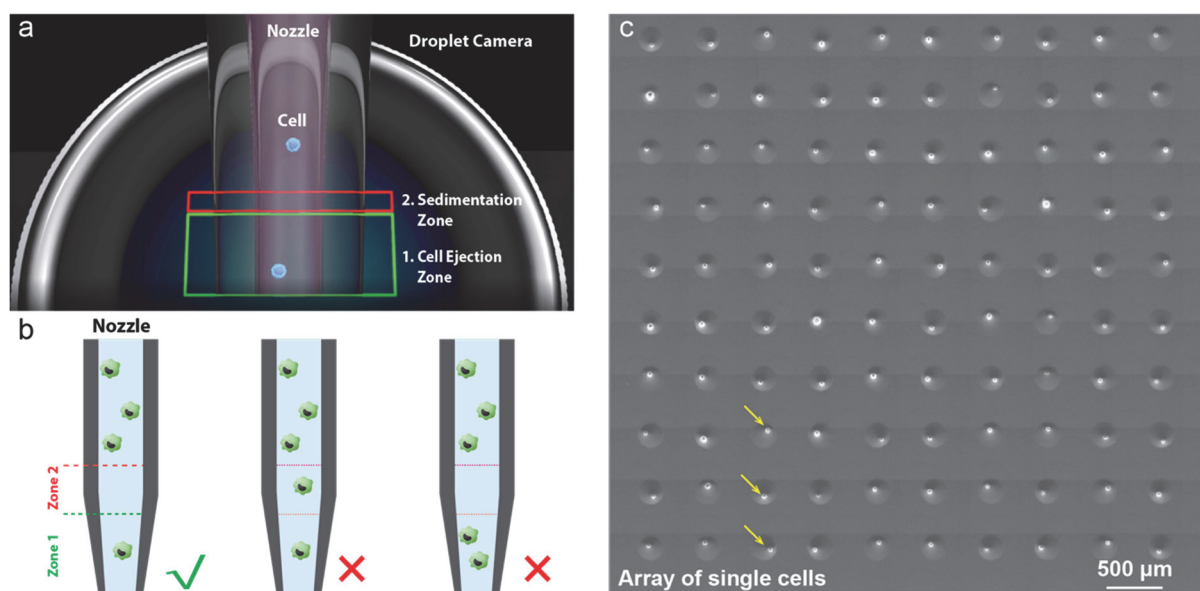
Figure 7.1. Single-cell dispensing technique with liquid dispensing tool. (a) The new technique, CellenONE®, has been developed by Cellenion, France. (b) Mechanism of single-cell dispensing. (c) Single lung cancer cells were successfully isolated and positioned on individual spots.

cell arrays can reach almost 100% in a straightforward manner (Figure 7.1c). This novel technique paves a promising alternative avenue towards single-cell studies.

How to monitor a large number of single cells

Following the generation of single cell arrays, the format of label-free detection readouts should also be expanded for high-throughput analysis. The real-time collection of optical signals described in this thesis are carried out by spectroscopic imaging. This imaging setup enables excellent spectral sensitivity for nanoplasmonic sensing. Nevertheless, the spatial imaging throughput is in turn greatly comprised, with only one single image can be analyzed during the entire real-time monitoring process. The two-dimensional image is inevitably cropped to one-dimension by the linear entrance slit (Figure 3.1) in order to guarantee that the spectrum derives from an accurate sensor area without spectral contamination from surrounding areas. A possible solution requires precise synergy between the spectra acquisition and spatial scanning of all the single cells. Such evolved setup can be fulfilled by further software programming incorporating the microscope mechanics and image analysis.

Alternatively, a conversion from spectral interrogation to quantifying image intensity will fulfill the high throughput without immensely investing on software synchronization. The binding of target molecules on plasmonic surface induces a spectral shift. By filtering the illumination or transmission spectrum, the spectral shift will additionally induce a
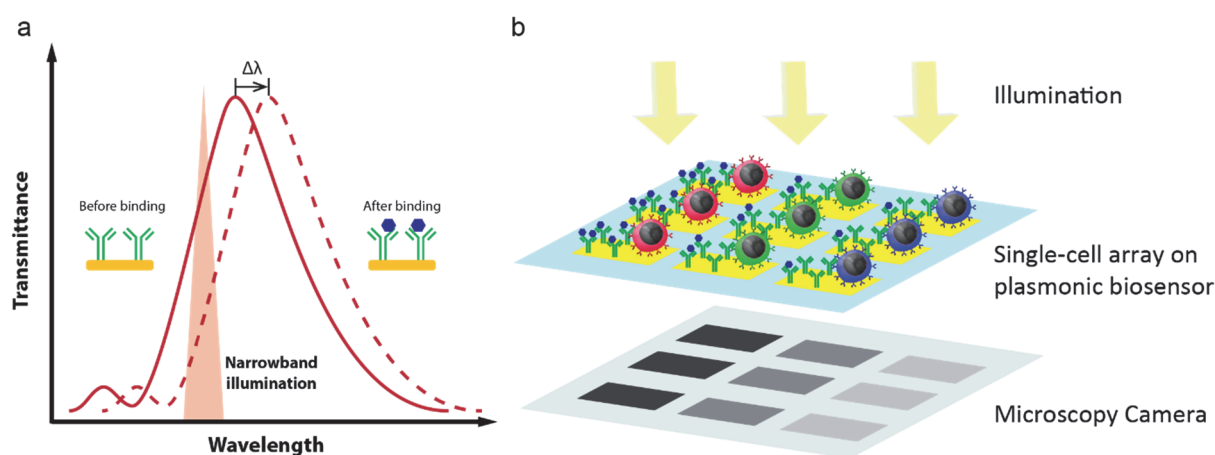
Figure 7.2. Principle for plasmonic intensity imaging analysis. (a) With narrowband illumination, the spectral shifts of the resonance peak can be converted to intensity variation. (b) A proposed scenario of high-throughput single-cell secretion analysis with intensity-based imaging technique.

corresponding intensity changes (Figure 7.2a). This signal conversion facilitates spontaneous detection readout across a larger sensor area, enhancing the analysis in enhanced throughput (Figure 7.2b). This alternative strategy has also been adopted in SPRi (SPR imaging) system [216], confirming the promising application for large-scale label-free optical detection. Furthermore, the mechanical control and real-time imaging analysis can be readily performed by established commercial microscope imaging software (e.g., Nikon NIS-Elements). However, more in-depth investigations are necessary regarding the detection sensitivity, namely the limit of molecule detection.

7.2.2 Retrieval of target cell candidates after screening

With the high-throughput analysis format, the plasmonic label-free biosensor can be exploited as a fast screening platform to select chemical candidates for drug discovery and functional cells for adoptive cell therapy. Hence a technical challenge has emerged for the application of cell screening, which is the recovery of the target cells for downstream procedure. Due to microscale feature of one individual cell, it is unrealistic to access the cell with manual pipetting. Different strategies could be designed based on the screening platform employed for the single-cell assays.

For microfluidic-based platforms

Microfluidics offers accessible means to recover single cells. The recent advancement of microfluidic technology has upgraded the systematic sophistication from simple monolayered liquid channels to complex network of multilayered conduits for multiple fluids [215], [217]–[219]. This new configuration of fluidic channels, namely microfluidic circuits, incorporates pneumatic or hydraulic pressure regulation to manipulate the underlying liquid transportation. Sophisticated but precise sequence of reagent administration can be readily applied for single cell capturing, cell culture and biochemical assays (e.g., cell lysis and immunofluorescence imaging). Moreover, the entire process of fluidic regulation and relevant microscopic imaging can be programmed and automated without the need of operator attendance [218]. However, the design and operation of such complex system still require extensive expertise of

microfabrication, software programming and related engineering techniques, encumbering the immediate application for laboratorial and industrial purposes.
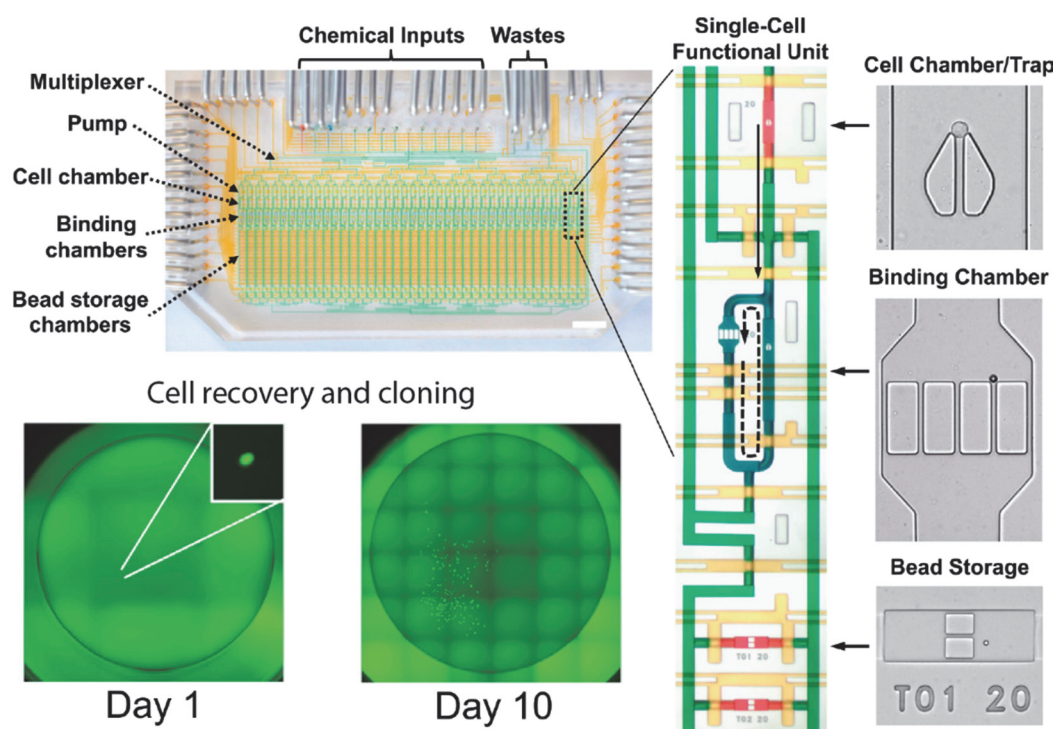
Figure 7.3. Microfluidic circuit for on-chip single-cell analysis and cell recovery. Image reproduced from [218].

For basic microscale single-cell platforms

Some user-friendly platforms have been accessible to biological researchers for single-cell studies, such as solid-based arrays of microscale open structures (e.g., microwells). The end users can simply deposit suspended cells on the structures by using liquid dispensing tools to generate large-scale single-cell arrays [150]. With such open screening configurations where one side of the microstructure is accessible (e.g., top surface of microwells), cells can be retrieved through the open surface by precise mechanical techniques, typically a micromanipulator [220]. The mechanical device applies gentle suction force at the end of a microscale nozzle to grab the cell-of-interest, transports the cells transiently and places them in user-desired environment. Micromanipulators have established wide applications in single-

cell screening studies due to the good compatibility with microscopes for cell imaging. Furthermore, automation of such mechanical single cell selection has also been realized (e.g. ALS CellCelector™ in Figure 7.4) [221], [222], as well as the integration with the upstream functional detections, distinguishing the candidate cells and isolating them individually for subsequent assays (e.g., PCR analysis). Due to the excellent compatibility with common biological microscopes, the micromaniputor-based cell retrieval technique offers a facile solution for our plasmonic nanobiosensor to analysis automation and clinical application.
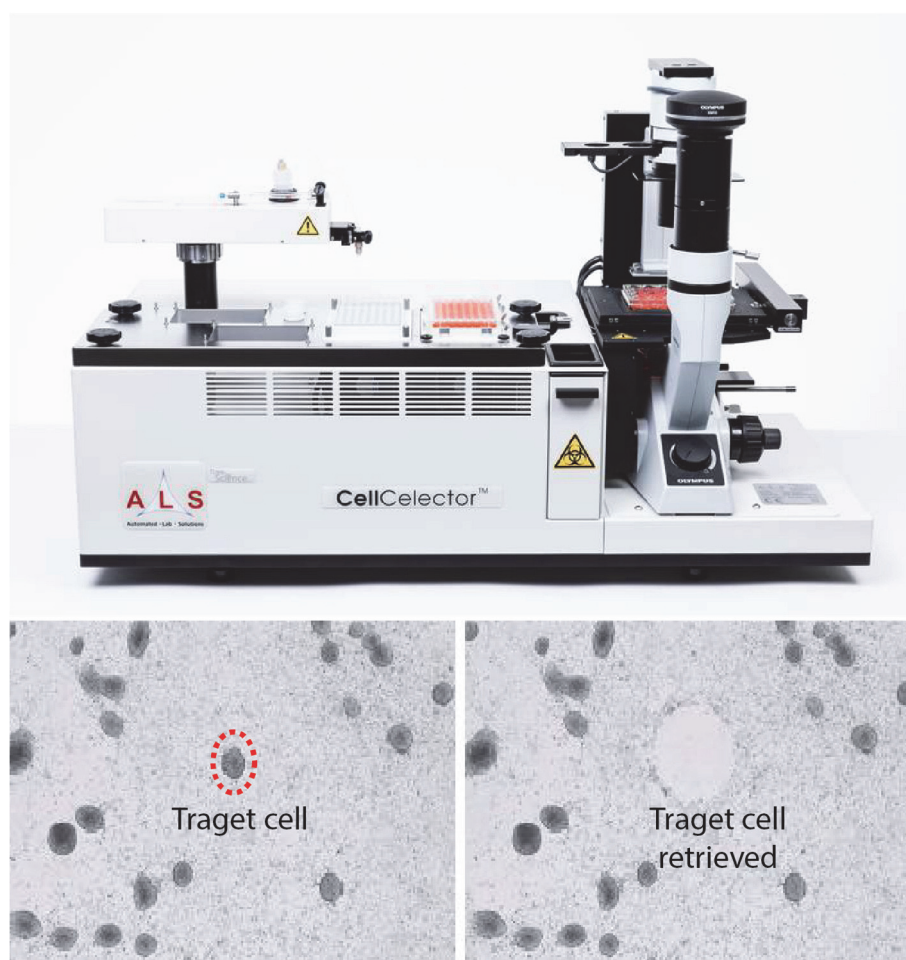
Figure 7.4. Mechanical system for single-cell retrieval. ALS CellCelector™ system is shown here, which has been developed by ALS Automated Lab Solutions GmbH, Germany.

7.2.3 Biomimicking cell niche on plasmonic nanobiosensor

Besides the technical issues for cell analysis, another essential factor should not be overlooked, which is the growth environment of cells. There are two main interactions ongoing in cellular microenvironment: cell-matrix interaction and cell-cell interaction.

The majority of *in vitro* label-free cell studies has still been employing two-dimensional cell cultures on planar surfaces. However, not all types of cells grow on planar surfaces in their original environment. Most of human somatic cells are surrounded by a complex network of scaffold biomatrices (e.g., collagen, polysaccharide) and neighboring cells, with which cells interact 360°. By plating cells on planar surfaces *in vitro*, artificial cellular polarization is inevitably generated and thus distorts the relevance of analysis outcome to in vivo situation (Figure 7.5) [223]. Different strategies have been explored to tackle this challenge. Apart from constructing artificial lipid membranes (described in chapter 6), cell encapsulation in biocompatible scaffold materials has shown remarkable potential for biomimicking *in vitro* studies [224]–[229]. For instance, hydrogels can effectively contain cells and support long-term cell survival by providing efficient nutrient supply with high material porosity and a three-dimensional niche with cell-material interaction in all directions. The choice of materials and chemical modifications are readily available for different kinds of cells. By incorporating the single-cell dispensing technique, the high-throughput single-cell array can be generated in a three-dimensional cell culture format. This will open a new avenue for label-free single-cell analysis and accelerate the translation to pharmaceutical and clinical applications.

Cell-cell interaction is another indispensable player that is involved in cellular microenvironment. Indeed, adoptive cell immunity is primarily mediated by interactions between antigen-presenting cells (e.g., dendritic cells or macrophages) and T cells. These intercellular communications involve numerous molecular binding, recognition and signaling events on cell membranes, most of which will trigger the secretion of cytokines, chemokines and other effectors [230]. Due to the dynamic nature of these activities, it will be of great interest to investigate them with label-free technologies, such as the proposed plasmonic biosensors in the thesis.
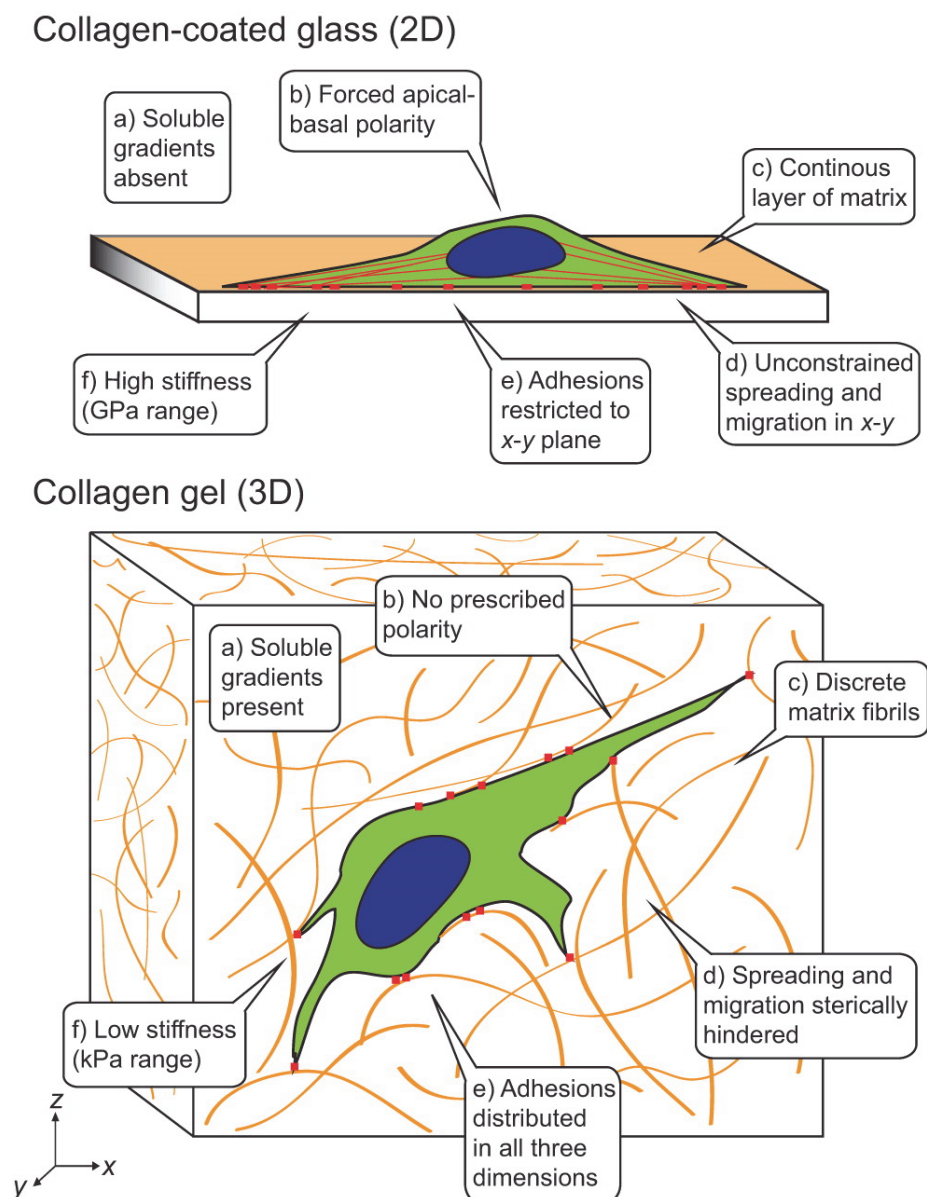
Figure 7.5. The comparison of biological cues between 2D and 3D cell culture scenarios. The adhesive, topographical, mechanical, and soluble cues encountered by a cell are extremely different between a collagen-coated planar surface (2D) and a typical collagen scaffold. Image reprinted from [223].

127

Bibliography

[1]   M. W. Gonzalez and M. G. Kann, "Chapter 4: Protein Interactions and Disease," *PLOS Computational Biology*, vol. 8, no. 12, p. e1002819, Dec. 2012.

[2]   J. N. Adkins *et al.*, "Toward a Human Blood Serum Proteome: Analysis By Multidimensional Separation Coupled With Mass Spectrometry," *Molecular & Cellular Proteomics*, vol. 1, no. 12, pp. 947–955, Dec. 2002.

[3]   L. M. Smith *et al.*, "Proteoform: a single term describing protein complexity," *Nature Methods*, vol. 10, no. 3, pp. 186–187, Mar. 2013.

[4]   N. I. of H. National Human Genome Research Institute, "'Talking Glossary of Genetic Terms.'" [Online]. Available: https://www.genome.gov/glossary/. [Accessed: 11-Feb-2019].

[5]   C. Soto, "Protein misfolding and disease; protein refolding and therapy," *FEBS Letters*, vol. 498, no. 2, pp. 204–207, Jun. 2001.

[6]   C. A. K. Borrebaeck, "Precision diagnostics: moving towards protein biomarker signatures of clinical utility in cancer," *Nature Reviews Cancer*, vol. 17, no. 3, pp. 199–204, Mar. 2017.

[7]   S. T. Sanjay *et al.*, "Biomarker detection for disease diagnosis using cost-effective microfluidic platforms," *Analyst*, vol. 140, no. 21, pp. 7062–7081, Oct. 2015.

[8]   G. Dranoff, "Cytokines in cancer pathogenesis and cancer therapy," *Nat Rev Cancer*, vol. 4, no. 1, pp. 11–22, Jan. 2004.

[9]   M. Uhlén *et al.*, "Tissue-based map of the human proteome," *Science*, vol. 347, no. 6220, p. 1260419, Jan. 2015.

[10]   F. H. Crick, "On protein synthesis," *Symp. Soc. Exp. Biol.*, vol. 12, pp. 138–163, 1958.

[11]   The Human Protein Atlas, "Overview of the secretory pathway." [Online]. Available: https://www.proteinatlas.org/humanproteome/cell/secreted+proteins. [Accessed: 26-Mar-2019].

[12]   R. I. Krohn, "The Colorimetric Detection and Quantitation of Total Protein," *Current Protocols in Cell Biology*, vol. 15, no. 1, p. A.3H.1-A.3H.28, 2002.

[13]   Z. Dembic, "Chapter 8 - Cytokines Important for Growth and/or Development of Cells of the Immune System," in *The Cytokines of the Immune System*, Amsterdam: Academic Press, 2015, pp. 263–281.

[14]   M. Bhardwaj, A. Gies, S. Werner, P. Schrotz-King, and H. Brenner, "Blood-Based Protein Signatures for Early Detection of Colorectal Cancer: A Systematic Review," *Clinical and Translational Gastroenterology*, vol. 8, no. 11, Nov. 2017.

Bibliography

[15] E. Boschetti, A. D'Amato, G. Candiano, and P. G. Righetti, "Protein biomarkers for early detection of diseases: The decisive contribution of combinatorial peptide ligand libraries," *Journal of Proteomics*, vol. 188, pp. 1–14, Sep. 2018.

[16] C. Sima *et al.*, "Assessing Combinational Drug Efficacy in Cancer Cells by Using Image-based Dynamic Response Analysis," *Cancer Inform*, vol. 14, no. Suppl 5, pp. 33–43, 2015.

[17] M. S. Wang, Z. Luo, and N. Nitin, "Rapid assessment of drug response in cancer cells using microwell array and molecular imaging," *Anal Bioanal Chem*, vol. 406, no. 17, pp. 4195–4206, Jul. 2014.

[18] J. A. Ludwig and J. N. Weinstein, "Biomarkers in cancer staging, prognosis and treatment selection," *Nat. Rev. Cancer*, vol. 5, no. 11, pp. 845–856, Nov. 2005.

[19] S. Sethi, S. Ali, P. A. Philip, and F. H. Sarkar, "Clinical Advances in Molecular Biomarkers for Cancer Diagnosis and Therapy," *International Journal of Molecular Sciences*, vol. 14, no. 7, pp. 14771–14784, Jul. 2013.

[20] J. R. Heath, A. Ribas, and P. S. Mischel, "Single-cell analysis tools for drug discovery and development," *Nat Rev Drug Discov*, vol. 15, no. 3, pp. 204–216, Mar. 2016.

[21] D. Wang and S. Bodovitz, "Single cell analysis: the new frontier in 'omics,'" *Trends in Biotechnology*, vol. 28, no. 6, pp. 281–290, Jun. 2010.

[22] S. J. Altschuler and L. F. Wu, "Cellular Heterogeneity: Do Differences Make a Difference?," *Cell*, vol. 141, no. 4, pp. 559–563, May 2010.

[23] J. A. Griffiths, A. Scialdone, and J. C. Marioni, "Using single-cell genomics to understand developmental processes and cell fate decisions," *Molecular Systems Biology*, vol. 14, no. 4, p. e8046, Apr. 2018.

[24] A. Koseska and P. I. Bastiaens, "Cell signaling as a cognitive process," *The EMBO Journal*, vol. 36, no. 5, pp. 568–582, Mar. 2017.

[25] G. C. Tsokos and N. R. Rose, "Immune cell signaling in autoimmune diseases," *Clinical Immunology*, vol. 181, no. Supplement C, pp. 1–8, Aug. 2017.

[26] G.-C. Yuan *et al.*, "Challenges and emerging directions in single-cell analysis," *Genome Biology*, vol. 18, p. 84, May 2017.

[27] E. Engvall and P. Perlmann, "Enzyme-linked immunosorbent assay (ELISA) quantitative assay of immunoglobulin G," *Immunochemistry*, vol. 8, no. 9, pp. 871–874, Sep. 1971.

[28] C. C. Czerkinsky, L.-Å. Nilsson, H. Nygren, Ö. Ouchterlony, and A. Tarkowski, "A solid-phase enzyme-linked immunospot (ELISPOT) assay for enumeration of specific antibody-secreting cells," *Journal of Immunological Methods*, vol. 65, no. 1, pp. 109–121, Dec. 1983.

[29] C. Möbs and T. Schmidt, "Research Techniques Made Simple: Monitoring of T-Cell Subsets using the ELISPOT Assay," *Journal of Investigative Dermatology*, vol. 136, no. 6, pp. e55–e59, Jun. 2016.

[30] A. Turner, I. Karube, and G. S. Wilson, *Biosensors : Fundamentals and Applications*. Oxford University Press, 1987.

[31] Y. Wang and E. C. Alocilja, "Gold nanoparticle-labeled biosensor for rapid and sensitive detection of bacterial pathogens," *Journal of Biological Engineering*, vol. 9, no. 1, p. 16, Oct. 2015.

Bibliography

[32]   D. Grieshaber, R. MacKenzie, J. Vörös, and E. Reimhult, "Electrochemical Biosensors - Sensor Principles and Architectures," *Sensors (Basel)*, vol. 8, no. 3, pp. 1400–1458, Mar. 2008.

[33]   T. Terse-Thakoor, S. Badhulika, and A. Mulchandani, "Graphene based biosensors for healthcare," *Journal of Materials Research*, vol. 32, no. 15, pp. 2905–2929, Aug. 2017.

[34]   L. C. Clark and C. Lyons, "ELECTRODE SYSTEMS FOR CONTINUOUS MONITORING IN CARDIOVASCULAR SURGERY," *Annals of the New York Academy of Sciences*, vol. 102, no. 1, pp. 29–45, Dec. 2006.

[35]   A. Thomas, L. Heinemann, A. Ramírez, and A. Zehe, "Options for the Development of Noninvasive Glucose Monitoring: Is Nanotechnology an Option to Break the Boundaries?," *J Diabetes Sci Technol*, vol. 10, no. 3, pp. 782–789, May 2016.

[36]   E. P. Randviir and C. E. Banks, "Electrochemical impedance spectroscopy: an overview of bioanalytical applications," *Analytical Methods*, vol. 5, no. 5, pp. 1098–1115, 2013.

[37]   *Electrochemical Sensors, Biosensors and their Biomedical Applications*. Elsevier, 2008.

[38]   J. L. Arlett, E. B. Myers, and M. L. Roukes, "Comparative advantages of mechanical biosensors," *Nature Nanotechnology*, vol. 6, no. 4, pp. 203–215, Apr. 2011.

[39]   X. Qiao, X. Zhang, Y. Tian, and Y. Meng, "Progresses on the theory and application of quartz crystal microbalance," *Applied Physics Reviews*, vol. 3, no. 3, p. 031106, Sep. 2016.

[40]   C. LU and A. W. CZANDERNA, Eds., "Applications of Piezoelectric Quartz Crystal Microbalances," in *Methods and Phenomena*, vol. 7, Elsevier, 1984, pp. 1–393.

[41]   A. S. Yuwono and P. S. Lammers, "Odor Pollution in the Environment and the Detection Instrumentation," *Agricultural Engineering International: CIGR Journal*, vol. VI, pp. 1–33, Jul. 2004.

[42]   A. M. Hutchinson, "Evanescent wave biosensors," *Mol Biotechnol*, vol. 3, no. 1, pp. 47–54, Feb. 1995.

[43]   M. c. Estevez, M. Alvarez, and L. m. Lechuga, "Integrated optical devices for lab-on-a-chip biosensing applications," *Laser & Photon. Rev.*, vol. 6, no. 4, pp. 463–487, Jul. 2012.

[44]   K. Okamoto, *Fundamentals of Optical Waveguides*, 2nd ed. Elsevier, 2006.

[45]   G. A. Lopez, M.-C. Estevez, M. Soler, and L. M. Lechuga, "Recent advances in nanoplasmonic biosensors: applications and lab-on-a-chip integration," *Nanophotonics*, vol. 6, no. 1, Jan. 2017.

[46]   B. Špačková, P. Wrobel, M. Bocková, and J. Homola, "Optical Biosensors Based on Plasmonic Nanostructures: A Review," *Proceedings of the IEEE*, vol. 104, no. 12, pp. 2380–2408, Dec. 2016.

[47]   D. Duval *et al.*, "Nanophotonic lab-on-a-chip platforms including novel bimodal interferometers, microfluidics and grating couplers," *Lab on a Chip*, vol. 12, no. 11, pp. 1987–1994, 2012.

[48]   E. Kim, M. D. Baaske, and F. Vollmer, "Towards next-generation label-free biosensors: recent advances in whispering gallery mode sensors," *Lab on a Chip*, vol. 17, no. 7, pp. 1190–1205, 2017.

[49]   J. Wang, Z. Yao, T. Lei, and A. W. Poon, "Silicon coupled-resonator optical-waveguide-based biosensors using light-scattering pattern recognition with pixelized mode-field-intensity distributions," *Scientific Reports*, vol. 4, p. 7528, Dec. 2014.

[50]   M. Soler, C. S. Huertas, and L. M. Lechuga, "Label-free plasmonic biosensors for point-of-care diagnostics: a review," *Expert Review of Molecular Diagnostics*, vol. 19, no. 1, pp. 71–81, Jan. 2019.

[51]   T. Kilic, A. T. D. S. Valinhas, I. Wall, P. Renaud, and S. Carrara, "Label-free detection of hypoxia-induced extracellular vesicle secretion from MCF-7 cells," *Scientific Reports*, vol. 8, no. 1, p. 9402, Jun. 2018.

[52]   Y.-G. Zhou, L. Kermansha, L. Zhang, and R. M. Mohamadi, "Miniaturized Electrochemical Sensors to Facilitate Liquid Biopsy for Detection of Circulating Tumor Markers," in *Applications of Microfluidic Systems in Biology and Medicine*, M. Tokeshi, Ed. Singapore: Springer Singapore, 2019, pp. 71–98.

[53]   Y. S. Zhang *et al.*, "Multisensor-integrated organs-on-chips platform for automated and continual in situ monitoring of organoid behaviors," *PNAS*, vol. 114, no. 12, pp. E2293–E2302, Mar. 2017.

[54]   J. P. Wikswo *et al.*, "Engineering Challenges for Instrumenting and Controlling Integrated Organ-on-Chip Systems," *IEEE Trans Biomed Eng*, vol. 60, no. 3, pp. 682–690, Mar. 2013.

[55]   D. Bavli *et al.*, "Real-time monitoring of metabolic function in liver-on-chip microdevices tracks the dynamics of mitochondrial dysfunction," *PNAS*, vol. 113, no. 16, pp. E2231–E2240, Apr. 2016.

[56]   Q. Zhou *et al.*, "Liver injury-on-a-chip: microfluidic co-cultures with integrated biosensors for monitoring liver cell signaling during injury," *Lab Chip*, vol. 15, no. 23, pp. 4467–4478, Nov. 2015.

[57]   T. Kilic, F. Navaee, F. Stradolini, P. Renaud, and S. Carrara, "Organs-on-chip monitoring: sensors and other strategies," *Microphysiol Syst*, vol. 1, pp. 1–1, 2018.

[58]   A. Calzado-Martín, M. Encinar, J. Tamayo, M. Calleja, and A. San Paulo, "Effect of Actin Organization on the Stiffness of Living Breast Cancer Cells Revealed by Peak-Force Modulation Atomic Force Microscopy," *ACS Nano*, vol. 10, no. 3, pp. 3365–3374, Mar. 2016.

[59]   T. Kwon, S. Gunasekaran, and K. Eom, "Atomic force microscopy-based cancer diagnosis by detecting cancer-specific biomolecules and cells," *Biochimica et Biophysica Acta (BBA) - Reviews on Cancer*, vol. 1871, no. 2, pp. 367–378, Apr. 2019.

[60]   S. Sang, Y. Wang, Q. Feng, Y. Wei, J. Ji, and W. Zhang, "Progress of new label-free techniques for biosensors: a review," *Crit. Rev. Biotechnol.*, vol. 36, no. 3, pp. 465–481, 2016.

[61]   A. Otto, "Excitation of nonradiative surface plasma waves in silver by the method of frustrated total reflection," *Z. Physik*, vol. 216, no. 4, pp. 398–410, Aug. 1968.

[62]   Kretschmann E. and Raether H., "Notizen: Radiative Decay of Non Radiative Surface Plasmons Excited by Light," *zna*, vol. 23, no. 12, pp. 2135–2136, 1968.

[63]   B. Liedberg, C. Nylander, and I. Lunström, "Surface plasmon resonance for gas detection and biosensing," *Sensors and Actuators*, vol. 4, pp. 299–304, Jan. 1983.

[64]   I. Abdulhalim, M. Zourob, and A. Lakhtakia, "Surface Plasmon Resonance for Biosensing: A Mini-Review," *Electromagnetics*, vol. 28, no. 3, pp. 214–242, Mar. 2008.

[65]   G. Kumar and P. K. Sarswat, "Interaction of Surface Plasmon Polaritons with Nanomaterials," in *Reviews in Plasmonics 2015*, C. D. Geddes, Ed. Cham: Springer International Publishing, 2016, pp. 103–129.

Bibliography

[66] R. L. Olmon *et al.*, "Optical dielectric function of gold," *Phys. Rev. B*, vol. 86, no. 23, p. 235147, Dec. 2012.

[67] J. Homola, "Electromagnetic Theory of Surface Plasmons," in *Surface Plasmon Resonance Based Sensors*, vol. 4, 17 vols., J. Homola, Ed. Berlin, Heidelberg: Springer Berlin Heidelberg, 2006, pp. 3–44.

[68] NTU biomolecular interactions platform, "SPR Technology." [Online]. Available: http://www.sbs.ntu.edu.sg/interactions/Pages/Surface-Plasmon-Resonance.aspx. [Accessed: 12-Feb-2019].

[69] D. Sevenler, N. L. Ünlü, and M. S. Ünlü, "Nanoparticle Biosensing with Interferometric Reflectance Imaging," in *Nanobiosensors and Nanobioanalyses*, M. C. Vestergaard, K. Kerman, I.-M. Hsing, and E. Tamiya, Eds. Tokyo: Springer Japan, 2015, pp. 81–95.

[70] "Particles Small Compared with the Wavelength," in *Absorption and Scattering of Light by Small Particles*, Weinheim, Germany: Wiley-VCH Verlag GmbH, 2007, pp. 130–157.

[71] C. Genet and T. W. Ebbesen, "Light in tiny holes," *Nature*, vol. 445, no. 7123, pp. 39–46, Jan. 2007.

[72] H. Gao *et al.*, "Rayleigh anomaly-surface plasmon polariton resonances in palladium and gold subwavelength hole arrays," *Opt. Express, OE*, vol. 17, no. 4, pp. 2334–2340, Feb. 2009.

[73] A. E. Cetin *et al.*, "Handheld high-throughput plasmonic biosensor using computational on-chip imaging," *Light: Science & Applications*, vol. 3, no. 1, p. e122, Jan. 2014.

[74] A. G. Brolo, R. Gordon, B. Leathem, and K. L. Kavanagh, "Surface Plasmon Sensor Based on the Enhanced Light Transmission through Arrays of Nanoholes in Gold Films," *Langmuir*, vol. 20, no. 12, pp. 4813–4815, Jun. 2004.

[75] H. Im, N. C. Lindquist, A. Lesuffleur, and S.-H. Oh, "Atomic Layer Deposition of Dielectric Overlayers for Enhancing the Optical Properties and Chemical Stability of Plasmonic Nanoholes," *ACS Nano*, vol. 4, no. 2, pp. 947–954, Feb. 2010.

[76] T. W. Ebbesen, H. J. Lezec, H. F. Ghaemi, T. Thio, and P. A. Wolff, "Extraordinary optical transmission through sub-wavelength hole arrays," *Nature*, vol. 391, no. 6668, p. 667, Feb. 1998.

[77] A. Degiron and T. W. Ebbesen, "The role of localized surface plasmon modes in the enhanced transmission of periodic subwavelength apertures," *J. Opt. A: Pure Appl. Opt.*, vol. 7, no. 2, pp. S90–S96, Feb. 2005.

[78] M. Tabatabaei *et al.*, "Tunable 3D Plasmonic Cavity Nanosensors for Surface-Enhanced Raman Spectroscopy with Sub-femtomolar Limit of Detection," *ACS Photonics*, vol. 2, no. 6, pp. 752–759, Jun. 2015.

[79] M. Najiminaini, F. Vasefi, B. Kaminska, and J. J. L. Carson, "Experimental and numerical analysis on the optical resonance transmission properties of nano-hole arrays," *Opt. Express, OE*, vol. 18, no. 21, pp. 22255–22270, Oct. 2010.

[80] A. Hajiaboli, M. Kahrizi, and V.-V. Truong, "Optical behaviour of thick gold and silver films with periodic circular nanohole arrays," *J. Phys. D: Appl. Phys.*, vol. 45, no. 48, p. 485105, Dec. 2012.

[81] J. Braun, B. Gompf, G. Kobiela, and M. Dressel, "How Holes Can Obscure the View: Suppressed Transmission through an Ultrathin Metal Film by a Subwavelength Hole Array," *Phys. Rev. Lett.*, vol. 103, no. 20, p. 203901, Nov. 2009.

Bibliography

[82] M.-P. Murray-Methot, N. Menegazzo, and J.-F. Masson, "Analytical and physical optimization of nanohole-array sensors prepared by modified nanosphere lithography," *Analyst*, vol. 133, no. 12, pp. 1714–1721, Dec. 2008.

[83] A. E. Cetin and S. N. Topkaya, "Photonic crystal and plasmonic nanohole based label-free biodetection," *Biosensors and Bioelectronics*, vol. 132, pp. 196–202, May 2019.

[84] M. Najiminaini, F. Vasefi, B. Kaminska, and J. J. L. Carson, "Optical resonance transmission properties of nano-hole arrays in a gold film: effect of adhesion layer," *Opt. Express, OE*, vol. 19, no. 27, pp. 26186–26197, Dec. 2011.

[85] A. E. Cetin, D. Etezadi, B. C. Galarreta, M. P. Busson, Y. Eksioglu, and H. Altug, "Plasmonic Nanohole Arrays on a Robust Hybrid Substrate for Highly Sensitive Label-Free Biosensing," *ACS Photonics*, vol. 2, no. 8, pp. 1167–1174, Aug. 2015.

[86] F. Colas, D. Barchiesi, S. Kessentini, T. Toury, and M. L. de la Chapelle, "Comparison of adhesion layers of gold on silicate glasses for SERS detection," *J. Opt.*, vol. 17, no. 11, p. 114010, Oct. 2015.

[87] M. Bocková, J. Slabý, T. Špringer, and J. Homola, "Advances in Surface Plasmon Resonance Imaging and Microscopy and Their Biological Applications," *Annual Review of Analytical Chemistry*, vol. 12, no. 1, p. null, 2019.

[88] Biosensing Instrument, "Technical Note 102: SPR Sensitivity and Detection Limit," 11-Mar-2010. .

[89] G. Stybayeva, M. Kairova, E. Ramanculov, A. L. Simonian, and A. Revzin, "Detecting interferon-gamma release from human CD4 T-cells using surface plasmon resonance," *Colloids and Surfaces B: Biointerfaces*, vol. 80, no. 2, pp. 251–255, Oct. 2010.

[90] C. Liu, T. Lei, K. Ino, T. Matsue, N. Tao, and C.-Z. Li, "Real-time monitoring biomarker expression of carcinoma cells by surface plasmon resonance biosensors," *Chemical Communications*, vol. 48, no. 84, p. 10389, 2012.

[91] S. Milgram *et al.*, "On chip real time monitoring of B-cells hybridoma secretion of immunoglobulin," *Biosensors and Bioelectronics*, vol. 26, no. 5, pp. 2728–2732, Jan. 2011.

[92] H. H. Nguyen, J. Park, S. Kang, and M. Kim, "Surface Plasmon Resonance: A Versatile Technique for Biosensor Applications," *Sensors*, vol. 15, no. 5, pp. 10481–10510, May 2015.

[93] P. N. Abadian, C. P. Kelley, and E. D. Goluch, "Cellular Analysis and Detection Using Surface Plasmon Resonance Techniques," *Anal. Chem.*, vol. 86, no. 6, pp. 2799–2812, Mar. 2014.

[94] M. P. Raphael, J. A. Christodoulides, J. B. Delehanty, J. P. Long, and J. M. Byers, "Quantitative Imaging of Protein Secretions from Single Cells in Real Time," *Biophysical Journal*, vol. 105, no. 3, pp. 602–608, Aug. 2013.

[95] B.-R. Oh *et al.*, "Integrated Nanoplasmonic Sensing for Cellular Functional Immunoanalysis Using Human Blood," *ACS Nano*, vol. 8, no. 3, pp. 2667–2676, Mar. 2014.

[96] A.-P. Blanchard-Dionne and M. Meunier, "Sensing with periodic nanohole arrays," *Adv. Opt. Photon., AOP*, vol. 9, no. 4, pp. 891–940, Dec. 2017.

[97] L. Tu *et al.*, "Label-free and real-time monitoring of single cell attachment on template-stripped plasmonic nano-holes," *Sci Rep*, vol. 7, Sep. 2017.

[98] S. F. Romanuik *et al.*, "Detecting Antibodies Secreted by Trapped Cells Using Extraordinary Optical Transmission," *IEEE Sensors Journal*, vol. 11, no. 11, pp. 2732–2739, Nov. 2011.

Bibliography

[99] K. A. Tetz, L. Pang, and Y. Fainman, "High-resolution surface plasmon resonance sensor based on linewidth-optimized nanohole array transmittance," *Opt. Lett., OL*, vol. 31, no. 10, pp. 1528–1530, May 2006.

[100] A. De Leebeeck, L. K. S. Kumar, V. de Lange, D. Sinton, R. Gordon, and A. G. Brolo, "On-Chip Surface-Based Detection with Nanohole Arrays," *Anal. Chem.*, vol. 79, no. 11, pp. 4094–4100, Jun. 2007.

[101] G. M. Hwang, L. Pang, E. H. Mullen, and Y. Fainman, "Plasmonic Sensing of Biological Analytes Through Nanoholes," *IEEE Sensors Journal*, vol. 8, no. 12, pp. 2074–2079, Dec. 2008.

[102] A. Lesuffleur, H. Im, N. C. Lindquist, K. S. Lim, and S.-H. Oh, "Laser-illuminated nanohole arrays for multiplex plasmonic microarray sensing," *Opt. Express, OE*, vol. 16, no. 1, pp. 219–224, Jan. 2008.

[103] J. Ji, J. G. O'Connell, D. J. D. Carter, and D. N. Larson, "High-Throughput Nanohole Array Based System To Monitor Multiple Binding Events in Real Time," *Anal. Chem.*, vol. 80, no. 7, pp. 2491–2498, Apr. 2008.

[104] J.-C. Yang, J. Ji, J. M. Hogle, and D. N. Larson, "Metallic Nanohole Arrays on Fluoropolymer Substrates as Small Label-Free Real-Time Bioprobes," *Nano Lett.*, vol. 8, no. 9, pp. 2718–2724, Sep. 2008.

[105] J. C. Sharpe, J. S. Mitchell, L. Lin, N. Sedoglavich, and R. J. Blaikie, "Gold Nanohole Array Substrates as Immunobiosensors," *Anal. Chem.*, vol. 80, no. 6, pp. 2244–2249, Mar. 2008.

[106] H. Im, A. Lesuffleur, N. C. Lindquist, and S.-H. Oh, "Plasmonic Nanoholes in a Multichannel Microarray Format for Parallel Kinetic Assays and Differential Sensing," *Anal. Chem.*, vol. 81, no. 8, pp. 2854–2859, Apr. 2009.

[107] K.-L. Lee, S.-H. Wu, and P.-K. Wei, "Intensity sensitivity of gold nanostructures and its application for high-throughput biosensing," *Opt. Express, OE*, vol. 17, no. 25, pp. 23104–23113, Dec. 2009.

[108] F. Eftekhari *et al.*, "Nanoholes As Nanochannels: Flow-through Plasmonic Sensing," *Anal. Chem.*, vol. 81, no. 11, pp. 4308–4311, Jun. 2009.

[109] A. A. Yanik, M. Huang, A. Artar, T.-Y. Chang, and H. Altug, "Integrated nanoplasmonic-nanofluidic biosensors with targeted delivery of analytes," *Applied Physics Letters*, vol. 96, no. 2, p. 021101, 2010.

[110] H. Im *et al.*, "Template-Stripped Smooth Ag Nanohole Arrays with Silica Shells for Surface Plasmon Resonance Biosensing," *ACS Nano*, vol. 5, no. 8, pp. 6244–6253, Aug. 2011.

[111] A.-P. Blanchard-Dionne, L. Guyot, S. Patskovsky, R. Gordon, and M. Meunier, "Intensity based surface plasmon resonance sensor using a nanohole rectangular array," *Opt. Express, OE*, vol. 19, no. 16, pp. 15041–15046, Aug. 2011.

[112] C. Escobedo *et al.*, "Integrated nanohole array surface plasmon resonance sensing device using a dual-wavelength source," *J. Micromech. Microeng.*, vol. 21, no. 11, p. 115001, Oct. 2011.

[113] T.-Y. Chang *et al.*, "Large-scale plasmonic microarrays for label-free high-throughput screening," *Lab on a Chip*, vol. 11, no. 21, p. 3596, 2011.

[114] P. Jia, H. Jiang, J. Sabarinathan, and J. Yang, "Plasmonic nanohole array sensors fabricated by template transfer with improved optical performance," *Nanotechnology*, vol. 24, no. 19, p. 195501, Apr. 2013.

Bibliography

[115] G. A. C. Tellez, S. Hassan, R. N. Tait, P. Berini, and R. Gordon, "Atomically flat symmetric elliptical nanohole arrays in a gold film for ultrasensitive refractive index sensing," *Lab Chip*, vol. 13, no. 13, pp. 2541–2546, Jun. 2013.

[116] A. Barik, L. M. Otto, D. Yoo, J. Jose, T. W. Johnson, and S.-H. Oh, "Dielectrophoresis-Enhanced Plasmonic Sensing with Gold Nanohole Arrays," *Nano Lett.*, vol. 14, no. 4, pp. 2006–2012, Apr. 2014.

[117] H. Im *et al.*, "Label-free detection and molecular profiling of exosomes with a nano-plasmonic sensor," *Nature Biotechnology*, vol. 32, no. 5, pp. 490–495, Apr. 2014.

[118] J. W. de Menezes, A. Thesing, C. Valsecchi, L. E. G. Armas, and A. G. Brolo, "Improving the performance of gold nanohole array biosensors by controlling the optical collimation conditions," *Appl. Opt., AO*, vol. 54, no. 21, pp. 6502–6507, Jul. 2015.

[119] J. P. Monteiro, J. H. de Oliveira, E. Radovanovic, A. G. Brolo, and E. M. Girotto, "Microfluidic Plasmonic Biosensor for Breast Cancer Antigen Detection," *Plasmonics*, vol. 11, no. 1, pp. 45–51, Feb. 2016.

[120] S. T. Seiler, I. S. Rich, and N. C. Lindquist, "Direct spectral imaging of plasmonic nanohole arrays for real-time sensing," *Nanotechnology*, vol. 27, no. 18, p. 184001, Mar. 2016.

[121] M. Soler, A. Belushkin, A. Cavallini, C. Kebbi-Beghdadi, G. Greub, and H. Altug, "Multiplexed nanoplasmonic biosensor for one-step simultaneous detection of Chlamydia trachomatis and Neisseria gonorrhoeae in urine," *Biosensors and Bioelectronics*, vol. 94, no. Supplement C, pp. 560–567, Aug. 2017.

[122] X. Li, M. Soler, C. I. Özdemir, A. Belushkin, F. Yesilköy, and H. Altug, "Plasmonic nanohole array biosensor for label-free and real-time analysis of live cell secretion," *Lab Chip*, vol. 17, no. 13, pp. 2208–2217, Jun. 2017.

[123] X. Li *et al.*, "Label-Free Optofluidic Nanobiosensor Enables Real-Time Analysis of Single-Cell Cytokine Secretion," *Small*, vol. 14, no. 26, p. 1800698, Jun. 2018.

[124] C. Szydzik *et al.*, "Fabrication of complex PDMS microfluidic structures and embedded functional substrates by one-step injection moulding," *RSC Adv.*, vol. 6, no. 91, pp. 87988–87994, Sep. 2016.

[125] M. Irving *et al.*, "Interplay between T cell receptor binding kinetics and the level of cognate peptide presented by major histocompatibility complexes governs CD8+ T cell responsiveness," *J. Biol. Chem.*, vol. 287, no. 27, pp. 23068–23078, Jun. 2012.

[126] M. Hebeisen *et al.*, "Identification of Rare High-Avidity, Tumor-Reactive CD8+ T Cells by Monomeric TCR-Ligand Off-Rates Measurements on Living Cells," *Cancer Res.*, vol. 75, no. 10, pp. 1983–1991, May 2015.

[127] J. W. Sadowski, I. K. J. Korhonen, and J. P. K. Peltonen, "Characterization of thin films and their structures in surface plasmon resonance measurements," *OE*, vol. 34, no. 9, pp. 2581–2587, Sep. 1995.

[128] W. M. Albers and I. Vikholm-Lundin, "Surface Plasmon Resonance on Nanoscale Organic Films," *Nano-Bio-Sensing*, pp. 83–125, 2011.

[129] S. C. George and S. Thomas, "Transport phenomena through polymeric systems," *Progress in Polymer Science*, vol. 26, no. 6, pp. 985–1017, Aug. 2001.

[130] W. L. Robb, "Thin silicone membranes--their permeation properties and some applications," *Ann. N. Y. Acad. Sci.*, vol. 146, no. 1, pp. 119–137, Jan. 1968.

[131] C. Borgnakke and R. E. Sonntag, *Fundamentals of Thermodynamics*. Wiley, 2013.

[132] A. B. González-Guerrero, S. Dante, D. Duval, J. Osmond, and L. M. Lechuga, "Advanced photonic biosensors for point-of-care diagnostics," *Procedia Engineering*, vol. 25, no. Supplement C, pp. 71–75, Jan. 2011.

[133] J. N. Anker, W. P. Hall, O. Lyandres, N. C. Shah, J. Zhao, and R. P. V. Duyne, "Biosensing with plasmonic nanosensors," *Nature Materials*, vol. 7, no. 6, p. nmat2162, Jun. 2008.

[134] A. G. Brolo, "Plasmonics for future biosensors," *Nature Photonics*, vol. 6, no. 11, pp. 709–713, 2012.

[135] D. R. Shankaran, K. V. Gobi, and N. Miura, "Recent advancements in surface plasmon resonance immunosensors for detection of small molecules of biomedical, food and environmental interest," *Sensors and Actuators B: Chemical*, vol. 121, no. 1, pp. 158–177, Jan. 2007.

[136] M.-C. Estevez, M. A. Otte, B. Sepulveda, and L. M. Lechuga, "Trends and challenges of refractometric nanoplasmonic biosensors: A review," *Analytica Chimica Acta*, vol. 806, pp. 55–73, Jan. 2014.

[137] C. Escobedo, "On-chip nanohole array based sensing: a review," *Lab Chip*, vol. 13, no. 13, pp. 2445–2463, Jun. 2013.

[138] S. Hoon Lee, N. C. Lindquist, N. J. Wittenberg, L. R. Jordan, and S.-H. Oh, "Real-time full-spectral imaging and affinity measurements from 50 microfluidic channels using nanohole surface plasmon resonance," *Lab on a Chip*, vol. 12, no. 20, pp. 3882–3890, 2012.

[139] A. A. Yanik *et al.*, "An Optofluidic Nanoplasmonic Biosensor for Direct Detection of Live Viruses from Biological Media," *Nano Letters*, vol. 10, no. 12, pp. 4962–4969, Dec. 2010.

[140] A. F. Coskun, A. E. Cetin, B. C. Galarreta, D. A. Alvarez, H. Altug, and A. Ozcan, "Lensfree optofluidic plasmonic sensor for real-time and label-free monitoring of molecular binding events over a wide field-of-view," *Scientific Reports*, vol. 4, p. 6789, Oct. 2014.

[141] U. Y. Lau, S. S. Saxer, J. Lee, E. Bat, and H. D. Maynard, "Direct Write Protein Patterns for Multiplexed Cytokine Detection from Live Cells Using Electron Beam Lithography," *ACS Nano*, vol. 10, no. 1, pp. 723–729, Jan. 2016.

[142] S. S. Aćimović *et al.*, "LSPR Chip for Parallel, Rapid, and Sensitive Detection of Cancer Markers in Serum," *Nano Lett.*, vol. 14, no. 5, pp. 2636–2641, May 2014.

[143] S. Zhan, X. Wang, and Y. Liu, "Fast centroid algorithm for determining the surface plasmon resonance angle using the fixed-boundary method," *Meas. Sci. Technol.*, vol. 22, no. 2, p. 025201, 2011.

[144] T. McPherson, A. Kidane, I. Szleifer, and K. Park, "Prevention of Protein Adsorption by Tethered Poly(ethylene oxide) Layers: Experiments and Single-Chain Mean-Field Analysis," *Langmuir*, vol. 14, no. 1, pp. 176–186, Jan. 1998.

[145] D. MacDougall and W. B. Crummett, "Guidelines for data acquisition and data quality evaluation in environmental chemistry," *Anal. Chem.*, vol. 52, no. 14, pp. 2242–2249, Dec. 1980.

[146] G. Delfino, L. Di Costanzo, A. Paulis, G. Fabbrocini, and G. Monfrecola, "In vitro ultraviolet A irradiation decreases both release ability and gene-expression of vascular endothelial growth factor-A from mast cells," *Photodermatology, photoimmunology & photomedicine*, vol. 28, no. 3, pp. 165–168, 2012.

---

[147] S. F. Abcouwer, P. L. Marjon, R. K. Loper, and D. L. Vander Jagt, "Response of VEGF expression to amino acid deprivation and inducers of endoplasmic reticulum stress," *Investigative ophthalmology & visual science*, vol. 43, no. 8, pp. 2791–2798, 2002.

[148] P. Page, J. DeJong, A. Bandstra, and R. A. Boomsma, "Effect of Serum and Oxygen Concentration on Gene Expression and Secretion of Paracrine Factors by Mesenchymal Stem Cells," *International Journal of Cell Biology*, vol. 2014, p. e601063, Dec. 2014.

[149] S. Dai, A. Gocher, L. Euscher, and A. Edelman, "Serum Starvation Induces a Rapid Increase of Akt Phosphorylation in Ovarian Cancer Cells," *FASEB J*, vol. 30, no. 1 Supplement, pp. 714.9-714.9, Apr. 2016.

[150] J. C. Love, J. L. Ronan, G. M. Grotenbreg, A. G. van der Veen, and H. L. Ploegh, "A microengraving method for rapid selection of single cells producing antigen-specific antibodies," *Nat Biotech*, vol. 24, no. 6, pp. 703–707, Jun. 2006.

[151] Y. Shirasaki *et al.*, "Real-time single-cell imaging of protein secretion," *Scientific Reports*, vol. 4, Apr. 2014.

[152] "Nanowell-Based Immunoassays for Measuring Single-Cell Secretion: Characterization of Transport and Surface Binding," *Anal. Chem.*, vol. 86, no. 23, pp. 11562–11569, Dec. 2014.

[153] A. J. Torres, R. L. Contento, S. Gordo, K. W. Wucherpfennig, and J. C. Love, "Functional single-cell analysis of T-cell activation by supported lipid bilayer-tethered ligands on arrays of nanowells," *Lab on a Chip*, vol. 13, no. 1, p. 90, 2013.

[154] V. Chokkalingam *et al.*, "Probing cellular heterogeneity in cytokine-secreting immune cells using droplet-based microfluidics," *Lab on a Chip*, vol. 13, no. 24, p. 4740, 2013.

[155] Y. F. S. Seah, H. Hu, and C. A. Merten, "Microfluidic single-cell technology in immunology and antibody screening," *Molecular Aspects of Medicine*, Sep. 2017.

[156] Y. Lu, L. Yang, W. Wei, and Q. Shi, "Microchip-based single-cell functional proteomics for biomedical applications," *Lab on a Chip*, vol. 17, no. 7, pp. 1250–1263, 2017.

[157] S.-H. Wu, K.-L. Lee, A. Chiou, X. Cheng, and P.-K. Wei, "Optofluidic Platform for Real-Time Monitoring of Live Cell Secretory Activities Using Fano Resonance in Gold Nanoslits," *Small*, vol. 9, no. 20, pp. 3532–3540, Oct. 2013.

[158] J. Park, H. Im, S. Hong, C. M. Castro, R. Weissleder, and H. Lee, "Analyses of Intravesicular Exosomal Proteins Using a Nano-Plasmonic System," *ACS Photonics*, vol. 5, no. 2, pp. 487–494, Feb. 2018.

[159] He Jiacheng, Brimmo Ayoola T., Qasaimeh Mohammad A., Chen Pengyu, and Chen Weiqiang, "Recent Advances and Perspectives in Microfluidics-Based Single-Cell Biosensing Techniques," *Small Methods*, vol. 1, no. 10, p. 1700192, Sep. 2017.

[160] S. Halldorsson, E. Lucumi, R. Gómez-Sjöberg, and R. M. T. Fleming, "Advantages and challenges of microfluidic cell culture in polydimethylsiloxane devices," *Biosensors and Bioelectronics*, vol. 63, no. Supplement C, pp. 218–231, Jan. 2015.

[161] Y. S. Heo *et al.*, "Characterization and Resolution of Evaporation-Mediated Osmolality Shifts That Constrain Microfluidic Cell Culture in Poly(dimethylsiloxane) Devices," *Anal. Chem.*, vol. 79, no. 3, pp. 1126–1134, Feb. 2007.

[162] E. Berthier, J. Warrick, H. Yu, and D. J. Beebe, "Managing evaporation for more robust microscale assays," *Lab Chip*, vol. 8, no. 6, pp. 852–859, May 2008.

Bibliography

[163] P. C. Thomas, S. R. Raghavan, and S. P. Forry, "Regulating Oxygen Levels in a Microfluidic Device," *Anal. Chem.*, vol. 83, no. 22, pp. 8821–8824, Nov. 2011.

[164] F. Yesilkoy *et al.*, "Phase-sensitive plasmonic biosensor using a portable and large field-of-view interferometric microarray imager," *Light: Science &Amp; Applications*, vol. 7, p. 17152, Feb. 2018.

[165] L. Martín-Moreno *et al.*, "Theory of Extraordinary Optical Transmission through Subwavelength Hole Arrays," *Phys. Rev. Lett.*, vol. 86, no. 6, pp. 1114–1117, Feb. 2001.

[166] S. G. Rodrigo, L. Martín-Moreno, A. Y. Nikitin, A. V. Kats, I. S. Spevak, and F. J. García-Vidal, "Extraordinary optical transmission through hole arrays in optically thin metal films," *Opt. Lett., OL*, vol. 34, no. 1, pp. 4–6, Jan. 2009.

[167] L. Feuz, M. P. Jonsson, and F. Höök, "Material-Selective Surface Chemistry for Nanoplasmonic Sensors: Optimizing Sensitivity and Controlling Binding to Local Hot Spots," *Nano Lett.*, vol. 12, no. 2, pp. 873–879, Feb. 2012.

[168] M. Bahramipanah, S. Dutta-Gupta, B. Abasahl, and O. J. F. Martin, "Cavity-Coupled Plasmonic Device with Enhanced Sensitivity and Figure-of-Merit," *ACS Nano*, vol. 9, no. 7, pp. 7621–7633, Jul. 2015.

[169] T. McPherson, A. Kidane, I. Szleifer, and K. Park, "Prevention of Protein Adsorption by Tethered Poly(ethylene oxide) Layers: Experiments and Single-Chain Mean-Field Analysis," *Langmuir*, vol. 14, no. 1, pp. 176–186, Jan. 1998.

[170] D. Mazia, G. Schatten, and W. Sale, "Adhesion of cells to surfaces coated with polylysine. Applications to electron microscopy," *J. Cell Biol.*, vol. 66, no. 1, pp. 198–200, Jul. 1975.

[171] B. Magnusson and U. Örnemark, *Eurachem Guide: The Fitness for Purpose of Analytical Methods – A Laboratory Guide to Method Validation and Related Topics*, Second. Olomouc: Eurachem, 2014.

[172] S. L. Gaffen and K. D. Liu, "Overview of interleukin-2 function, production and clinical applications," *Cytokine*, vol. 28, no. 3, pp. 109–123, Nov. 2004.

[173] J. J. Farrar, J. Fuller-Farrar, P. L. Simon, M. L. Hilfiker, B. M. Stadler, and W. L. Farrar, "Thymoma production of T cell growth factor (Interleukin 2).," *The Journal of Immunology*, vol. 125, no. 6, pp. 2555–2558, Dec. 1980.

[174] T. W. Murphy, Q. Zhang, L. B. Naler, S. Ma, and C. Lu, "Recent advances in the use of microfluidic technologies for single cell analysis," *The Analyst*, vol. 143, no. 1, pp. 60–80, 2018.

[175] S. A. Rosenberg, N. P. Restifo, J. C. Yang, R. A. Morgan, and M. E. Dudley, "Adoptive cell transfer: a clinical path to effective cancer immunotherapy," *Nat. Rev. Cancer*, vol. 8, no. 4, pp. 299–308, Apr. 2008.

[176] K. Newick, S. O'Brien, E. Moon, and S. M. Albelda, "CAR T Cell Therapy for Solid Tumors," *Annu. Rev. Med.*, vol. 68, pp. 139–152, 14 2017.

[177] D. J. Irvine, M. A. Purbhoo, M. Krogsgaard, and M. M. Davis, "Direct observation of ligand recognition by T cells," *Nature*, vol. 419, no. 6909, pp. 845–849, Oct. 2002.

[178] S. K. Bromley *et al.*, "The immunological synapse," *Annu. Rev. Immunol.*, vol. 19, pp. 375–396, 2001.

[179] M. Allard *et al.*, "TCR-ligand dissociation rate is a robust and stable biomarker of CD8^{+} T cell potency," *JCI Insight*, vol. 2, no. 14, Jul. 2017.

Bibliography

---

[180] D. G. Myszka, "Kinetic analysis of macromolecular interactions using surface plasmon resonance biosensors," *Current Opinion in Biotechnology*, vol. 8, no. 1, pp. 50–57, Feb. 1997.

[181] M. M. Davis *et al.*, "Ligand recognition by alpha beta T cell receptors," *Annu. Rev. Immunol.*, vol. 16, pp. 523–544, 1998.

[182] M. Corr *et al.*, "T cell receptor-MHC class I peptide interactions: affinity, kinetics, and specificity," *Science*, vol. 265, no. 5174, pp. 946–949, Aug. 1994.

[183] L. J. Edwards, V. I. Zarnitsyna, J. D. Hood, B. D. Evavold, and C. Zhu, "Insights into T cell recognition of antigen: significance of two-dimensional kinetic parameters," *Front Immunol*, vol. 3, p. 86, 2012.

[184] J. Huang *et al.*, "The kinetics of two-dimensional TCR and pMHC interactions determine T-cell responsiveness," *Nature*, vol. 464, no. 7290, pp. 932–936, Apr. 2010.

[185] B. Liu *et al.*, "2D TCR-pMHC-CD8 kinetics determines T-cell responses in a self-antigen-specific TCR system," *Eur. J. Immunol.*, vol. 44, no. 1, pp. 239–250, Jan. 2014.

[186] J. Schmidt, D. Dojcinovic, P. Guillaume, and I. Luescher, "Analysis, Isolation, and Activation of Antigen-Specific CD4(+) and CD8(+) T Cells by Soluble MHC-Peptide Complexes," *Front Immunol*, vol. 4, p. 218, 2013.

[187] A. Dahlin, M. Zäch, T. Rindzevicius, M. Käll, D. S. Sutherland, and F. Höök, "Localized Surface Plasmon Resonance Sensing of Lipid-Membrane-Mediated Biorecognition Events," *J. Am. Chem. Soc.*, vol. 127, no. 14, pp. 5043–5048, Apr. 2005.

[188] M. P. Jonsson, A. B. Dahlin, and F. Höök, "Nanoplasmonic Sensing Combined with Artificial Cell Membranes," in *Nanoplasmonic Sensors*, A. Dmitriev, Ed. New York, NY: Springer New York, 2012, pp. 59–82.

[189] O. Limaj *et al.*, "Infrared Plasmonic Biosensor for Real-Time and Label-Free Monitoring of Lipid Membranes," *Nano Lett.*, vol. 16, no. 2, pp. 1502–1508, Feb. 2016.

[190] K. Mossman and J. Groves, "Micropatterned supported membranes as tools for quantitative studies of the immunological synapse," *Chem Soc Rev*, vol. 36, no. 1, pp. 46–54, Jan. 2007.

[191] A. S. Cheung, D. K. Y. Zhang, S. T. Koshy, and D. J. Mooney, "Scaffolds that mimic antigen-presenting cells enable ex vivo expansion of primary T cells," *Nat. Biotechnol.*, vol. 36, no. 2, pp. 160–169, 2018.

[192] A. Olaru, C. Bala, N. Jaffrezic-Renault, and H. Y. Aboul-Enein, "Surface plasmon resonance (SPR) biosensors in pharmaceutical analysis," *Crit Rev Anal Chem*, vol. 45, no. 2, pp. 97–105, 2015.

[193] E. Zeidan, C. L. Kepley, C. Sayes, and M. G. Sandros, "Surface plasmon resonance: a label-free tool for cellular analysis," *Nanomedicine (Lond)*, vol. 10, no. 11, pp. 1833–1846, 2015.

[194] F. Zhang *et al.*, "Quantification of epidermal growth factor receptor expression level and binding kinetics on cell surfaces by surface plasmon resonance imaging," *Anal. Chem.*, vol. 87, no. 19, pp. 9960–9965, Oct. 2015.

[195] J. Mäkinen, "Development of MP-SPR biosensor analysis methology," University of Tampere, Tampere, 2017.

[196] M. Mrksich and G. M. Whitesides, "Using self-assembled monolayers to understand the interactions of man-made surfaces with proteins and cells," *Annu Rev Biophys Biomol Struct*, vol. 25, pp. 55–78, 1996.

[197] L. Li, S. Chen, and S. Jiang, "Protein interactions with oligo(ethylene glycol) (OEG) self-assembled monolayers: OEG stability, surface packing density and protein adsorption," *J Biomater Sci Polym Ed*, vol. 18, no. 11, pp. 1415–1427, 2007.

[198] B. Liu, W. Chen, K. Natarajan, Z. Li, D. H. Margulies, and C. Zhu, "The cellular environment regulates in situ kinetics of T-cell receptor interaction with peptide major histocompatibility complex," *Eur. J. Immunol.*, vol. 45, no. 7, pp. 2099–2110, Jul. 2015.

[199] E. T. Castellana and P. S. Cremer, "Solid supported lipid bilayers: From biophysical studies to sensor design," *Surface Science Reports*, vol. 61, no. 10, pp. 429–444, Nov. 2006.

[200] R. Naumann *et al.*, "Tethered Lipid Bilayers on Ultraflat Gold Surfaces," *Langmuir*, vol. 19, no. 13, pp. 5435–5443, Jun. 2003.

[201] N. A. Anderson, L. J. Richter, J. C. Stephenson, and K. A. Briggman, "Characterization and control of lipid layer fluidity in hybrid bilayer membranes," *J. Am. Chem. Soc.*, vol. 129, no. 7, pp. 2094–2100, Feb. 2007.

[202] H. Mozsolits, H.-J. Wirth, J. Werkmeister, and M.-I. Aguilar, "Analysis of antimicrobial peptide interactions with hybrid bilayer membrane systems using surface plasmon resonance," *Biochimica et Biophysica Acta (BBA) - Biomembranes*, vol. 1512, no. 1, pp. 64–76, May 2001.

[203] C. W. Meuse *et al.*, "Hybrid bilayer membranes in air and water: infrared spectroscopy and neutron reflectivity studies," *Biophys. J.*, vol. 74, no. 3, pp. 1388–1398, Mar. 1998.

[204] M.-P. Mingeot-Leclercq, M. Deleu, R. Brasseur, and Y. F. Dufrêne, "Atomic force microscopy of supported lipid bilayers," *Nat Protoc*, vol. 3, no. 10, pp. 1654–1659, 2008.

[205] E. Mauriz *et al.*, "On-line surface plasmon resonance biosensing of vascular endothelial growth factor signaling in intact-human hepatoma cell lines," *Analyst*, vol. 139, no. 6, pp. 1426–1435, Feb. 2014.

[206] R. Méjard, H. J. Griesser, and B. Thierry, "Optical biosensing for label-free cellular studies," *TrAC Trends in Analytical Chemistry*, vol. 53, pp. 178–186, Jan. 2014.

[207] F. Fathi, A. Rezabakhsh, R. Rahbarghazi, and M.-R. Rashidi, "Early-stage detection of VE-cadherin during endothelial differentiation of human mesenchymal stem cells using SPR biosensor," *Biosensors and Bioelectronics*, vol. 96, pp. 358–366, Oct. 2017.

[208] J. M. Rice, L. J. Stern, E. F. Guignon, D. A. Lawrence, and M. A. Lynes, "Antigen-specific T cell phenotyping microarrays using grating coupled surface plasmon resonance imaging and surface plasmon coupled emission," *Biosensors and Bioelectronics*, vol. 31, no. 1, pp. 264–269, Jan. 2012.

[209] R. Bombera, L. Leroy, T. Livache, and Y. Roupioz, "DNA-directed capture of primary cells from a complex mixture and controlled orthogonal release monitored by SPR imaging," *Biosensors and Bioelectronics*, vol. 33, no. 1, pp. 10–16, Mar. 2012.

[210] N. J. Wittenberg *et al.*, "High-Affinity Binding of Remyelinating Natural Autoantibodies to Myelin-Mimicking Lipid Bilayers Revealed by Nanohole Surface Plasmon Resonance," *Anal. Chem.*, vol. 84, no. 14, pp. 6031–6039, Jul. 2012.

[211] R. J. Martinez and B. D. Evavold, "Lower Affinity T Cells are Critical Components and Active Participants of the Immune Response," *Front Immunol*, vol. 6, Sep. 2015.

[212] L. Armbrecht and P. S. Dittrich, "Recent Advances in the Analysis of Single Cells," *Anal. Chem.*, vol. 89, no. 1, pp. 2–21, Jan. 2017.

Bibliography

[213] S. Mashaghi, A. Abbaspourrad, D. A. Weitz, and A. M. van Oijen, "Droplet microfluidics: A tool for biology, chemistry and nanotechnology," *TrAC Trends in Analytical Chemistry*, vol. 82, pp. 118–125, Sep. 2016.

[214] S. Moon *et al.*, "Drop-on-Demand Single Cell Isolation and Total RNA Analysis," *PLOS ONE*, vol. 6, no. 3, p. e17455, Mar. 2011.

[215] M. Junkin *et al.*, "High-Content Quantification of Single-Cell Immune Dynamics," *Cell Reports*, vol. 15, no. 2, pp. 411–422, Apr. 2016.

[216] C. Liu, F. Hu, W. Yang, J. Xu, and Y. Chen, "A critical review of advances in surface plasmon resonance imaging sensitivity," *TrAC Trends in Analytical Chemistry*, vol. 97, pp. 354–362, Dec. 2017.

[217] T. Frank and S. Tay, "Flow-switching allows independently programmable, extremely stable, high-throughput diffusion-based gradients," *Lab on a Chip*, vol. 13, no. 7, pp. 1273–1281, 2013.

[218] R. A. Kellogg, R. Gómez-Sjöberg, A. A. Leyrat, and S. Tay, "High-throughput microfluidic single-cell analysis pipeline for studies of signaling dynamics," *Nature Protocols*, vol. 9, no. 7, pp. 1713–1726, Jul. 2014.

[219] M. Junkin and S. Tay, "Microfluidic single-cell analysis for systems immunology," *Lab on a Chip*, vol. 14, no. 7, pp. 1246–1260, 2014.

[220] A. O. Ogunniyi, C. M. Story, E. Papa, E. Guillen, and J. C. Love, "Screening individual hybridomas by microengraving to discover monoclonal antibodies," *Nature Protocols*, vol. 4, no. 5, pp. 767–782, Apr. 2009.

[221] C. Nelep and J. Eberhardt, "Automated rare single cell picking with the ALS cellcelector™," *Cytometry Part A*, vol. 93, no. 12, pp. 1267–1270, 2018.

[222] M. Ø. Agerbæk *et al.*, "The VAR2CSA malaria protein efficiently retrieves circulating tumor cells in an EpCAM-independent manner," *Nature Communications*, vol. 9, no. 1, p. 3279, Aug. 2018.

[223] B. M. Baker and C. S. Chen, "Deconstructing the third dimension – how 3D culture microenvironments alter cellular cues," *J Cell Sci*, vol. 125, no. 13, pp. 3015–3024, Jul. 2012.

[224] A. Ranga, S. Gobaa, Y. Okawa, K. Mosiewicz, A. Negro, and M. P. Lutolf, "3D niche microarrays for systems-level analyses of cell fate," *Nature Communications*, vol. 5, p. 4324, Jul. 2014.

[225] M. Caiazzo, Y. Okawa, A. Ranga, A. Piersigilli, Y. Tabata, and M. P. Lutolf, "Defined three-dimensional microenvironments boost induction of pluripotency," *Nature Materials*, vol. 15, no. 3, pp. 344–352, Mar. 2016.

[226] X. Li, C. Wittkowske, R. Yao, and Y. Du, "Hydrogel as Stem Cell Niche for In Vivo Applications in Regenerative Medicine," in *Biomaterials and Stem Cells in Regenerative Medicine*, CRC Press Boca Raton, 2012, pp. 31–54.

[227] C. Fan and D.-A. Wang, "Macroporous Hydrogel Scaffolds for Three-Dimensional Cell Culture and Tissue Engineering," *Tissue Engineering Part B: Reviews*, vol. 23, no. 5, pp. 451–461, Jan. 2017.

[228] M. W. Tibbitt and K. S. Anseth, "Hydrogels as Extracellular Matrix Mimics for 3D Cell Culture," *Biotechnol Bioeng*, vol. 103, no. 4, pp. 655–663, Jul. 2009.

Bibliography

[229] N. Gjorevski *et al.*, "Designer matrices for intestinal stem cell and organoid culture," *Nature*, vol. 539, no. 7630, pp. 560–564, Nov. 2016.

[230] J. B. Huppa and M. M. Davis, "T-cell-antigen recognition and the immunological synapse," *Nature Reviews Immunology*, vol. 3, no. 12, p. 973, Dec. 2003.

Curriculum Vitae

LI Xiaokang

Nationality: Chinese
Birth date: July 28, 1988
peterxkli07@gmail.com
https://www.linkedin.com/in/xiaokangli

Education

2014 – 2019   **École Polytechnique Fédérale de Lausanne**, Ph.D., Lausanne, Switzerland

2011 – 2014   **Tsinghua University**, Master of Engineering, Beijing, China

2007 – 2011   **Tsinghua University**, Bachelor of Engineering, Beijing, China

Core Experience

2014 – 2019   **Doctoral thesis**, Bionanophotonic Systems Laboratory (BIOS), EPFL

Advisor: Prof. H. Altug
 "Engineering of a nanoplasmonic biosensor for label-free cell analysis."

Achievements:

- Initiation of biological research platforms in a newly established laboratory
- Collaborations with clinical labs in a local hospital and an engineering lab in Australia
- 3 full article publications, which are all selected as cover papers on renowned scientific journals
- 5 oral and multiple poster presentations in international conferences
- Cooperation with journalists for magazine and press releases on research activities

Teaching:

- 3 years of teaching assistants in 2 core master student courses at EPFL
- Supervision of several master student projects

2011 – 2014   **Master research assistant**, Dept. of Biomedical Engineering, Tsinghua University

Advisor: Prof. Y. Du
"Development of a novel cell culture platform for pharmaceutical applications."

Achievements:

- 3 full article publications, with one selected as the cover paper on a renowned scientific journal
- 2 book chapters published by CRC Press and John Wiley & Sons, Inc.
- 1 patent authorized and transferred in China

Summer 2010   **Visiting student**, Department of Biomedical Engineering, Johns Hopkins University

Advisor: Prof. W. Grayson
"Development of bioreactors for orthopedic tissue engineering applications."

2009 – 2010   **Undergraduate research training**, Dept. of Biomedical Engineering,
Tsinghua University

Advisor: Prof. J. Liu
"Whole-body hyperthermia therapy for mouse breast cancer."

Awards & Honors

2018   SPIE-MKS Research Excellence Award, SPIE Photonics West, San Francisco, USA
2016   Best Poster Prize, 51st Winter Seminar for Biophysical Chemistry,
            Molecular Biology and Cybernetics of Cell Functions, Klosters, Switzerland
2013   Scholarship: Xinjiang Economic and Technological Development Zone of Urumqi,
            Beijing, China
2012   Scholarship: The Guanghua Educational Scholarship, Beijing, China
2010   Scholarship: The Widjaya Scholarship for Tsinghua University, Beijing, China

Languages

- Chinese Mandarin (Native)
- English (Full professional proficiency)
- French (CEFR B1 level)

Skills

Engineering & Experimental

- Ultralow volume liquid dispensing
- Visible and near-infrared spectroscopy
- Bright-field and fluorescence microscopy
- Surface chemistry on metals and dielectric materials
- Biochemical molecular assays (e.g., ELISA, immunofluorescence staining)
- Preparation of synthetic and natural biomaterials (e.g., PDMS, collagen, Matrigel)
- Mammalian cell culture (e.g., stem cells, cell lines) and new cell culture models (e.g., 3D culture)

Graphic

- Adobe Photoshop, Adobe Illustrator, CorelDraw

Data analysis and Management

- Origin, Matlab, GraphpadPrism, Zotero, EndNote, Microsoft Office

Scientific writing and reporting

- Author of multiple scientific journal artiles, book chapters, and conference proceedings

Organizational

- 2 years of experience in organizing activities and planning the budget for the Chinese Scholars
  and Students Association at EPFL

Extracurricular activities

- Volunteer: 2-month service in the media village during the 2008 Beijing Olympic games
- Mountain hiking: 2-day trekking of 52 km around the Mount Kailash in Tibet, from 4678 m to 5648 m.
- Road cycling: day trips on road bike along several Swiss national cycling routes (e.g., along Lake Geneva)
- Bakery: good at the brownie, chocolate cake, and cheesecake.

Publications

Peer-reviewed Journal Articles

1. Soler, M., **Li, X**., John-Herpin, A., Schmidt, J., Coukos, G., and Altug, H. (2018). Two-Dimensional Label-Free Affinity Analysis of Tumor-Specific CD8 T Cells with a Biomimetic Plasmonic Sensor. ACS Sens. 3, 2286–2295. (Highlighted as the Front Cover Paper)

2. **Li, X.**, Soler, M., Szydzik, C., Khoshmanesh, K., Schmidt, J., Coukos, G., Mitchell, A., and Altug, H. (2018). Label-Free Optofluidic Nanobiosensor Enables Real-Time Analysis of Single-Cell Cytokine Secretion. Small 14, 1800698. (Highlighted as the Front Cover Paper)

3. **Li, X**., Soler, M., Özdemir, C.I., Belushkin, A., Yesilköy, F., and Altug, H. (2017). Plasmonic nanohole array biosensor for label-free and real-time analysis of live cell secretion. Lab Chip 17, 2208–2217. (Highlighted as the Back Cover Paper)

4. **Li, X.**, Zhao, H., Qi, C., Zeng, Y., Xu, F., and Du, Y. (2015). Direct intercellular communications dominate the interaction between adipose-derived MSCs and myofibroblasts against cardiac fibrosis. Protein Cell 6, 735–745.

5. Zeng, Y., Chen, C., Liu, W., Fu, Q., Han, Z., Li, Y., Feng, S., **Li, X.**, Qi, C., Wu, J., et al. (2015). Injectable microcryogels reinforced alginate encapsulation of mesenchymal stromal cells for leak-proof delivery and alleviation of canine disc degeneration. Biomaterials 59, 53–65.

6. Zhao, H., **Li, X.**, Zhao, S., Zeng, Y., Zhao, L., Ding, H., Sun, W., and Du, Y. (2014). Microengineered in vitro model of cardiac fibrosis through modulating myofibroblast mechanotransduction. Biofabrication 6, 045009.

7. Liu, W., Li, Y., Zeng, Y., Zhang, X., Wang, J., Xie, L., **Li, X**., and Du, Y. (2014). Microcryogels as injectable 3-D cellular microniches for site-directed and augmented cell delivery. Acta Biomaterialia 10, 1864–1875.

8. Yao, R., Wang, J., **Li, X**., Jung Jung, D., Qi, H., Kee, K.K., and Du, Y. (2014). Hepatic Differentiation of Human Embryonic Stem Cells as Microscaled Multilayered Colonies Leading to Enhanced Homogeneity and Maturation. Small 10, 4311–4323.

9. Zhao, S., Shen, Z., Wang, J., **Li, X.**, Zeng, Y., Wang, B., He, Y., and Du, Y. (2014). Glycerol-Mediated Nanostructure Modification Leading to Improved Transparency of Porous Polymeric Scaffolds for High Performance 3D Cell Imaging. Biomacromolecules 15, 2521–2531.

10. **Li, X.**, Zhang, X., Zhao, S., Wang, J., Liu, G., and Du, Y. (2014). Micro-scaffold array chip for upgrading cell-based high-throughput drug testing to 3D using benchtop equipment. Lab Chip 14, 471–481. (Highlighted as the Inside Front Cover Paper)

11. Jin, C., Zhang, J., **Li, X.**, Yang, X., Li, J., and Liu, J. (2013). Injectable 3-D Fabrication of Medical Electronics at the Target Biological Tissues. Scientific Reports 3, srep03442.

Patent

1. Du, Y., **Li, X.**, Zhang, X., (2013) Preparation and application of a bioreactor device, Chinese patent authorization, ZL 201310359407.9

Conference Papers

1. H. Altug, F. Yesilkoy, **X. Li**, M. Soler, A. Belushkin, Y. Jahani, R. Terborg, J. Pello, V. Pruneri. (2018) Photonic Metasurfaces for Next-Generation Biosensors. in Advanced Photonics 2018 (BGPP, IPR, NP, NOMA, Sensors, Networks, SPPCom, SOF), Paper ITh3J.5, Optical Society Of America, 2018, p. ITh3J.5.

2. **Li, X.**, Soler, M., Belushkin, A., Yesilköy, F., and Altug, H. (2018). Optofluidic nanoplasmonic biosensor for label-free live cell analysis in real time. In Plasmonics in Biology and Medicine XV, (International Society for Optics and Photonics), p. 105090E.

3. Soler, M., **Li, X.**, Belushkin, A., Yesilkoy, F., and Altug, H. (2018). Towards a point-of-care nanoplasmonic biosensor for rapid and multiplexed detection of pathogenic infections. In Plasmonics in Biology and Medicine XV, (International Society for Optics and Photonics), p. 105090I.

Book Chapters

1. Chen, H., **Li, X.** and Du, Y. (2012) 1D~3D Nano-engineered Biomaterials for Biomedical Applications, in Integrated Biomaterials for Biomedical Technology (eds M. Ramalingam, A. Tiwari, S. Ramakrishna, and H. Kobayashi), John Wiley & Sons, Inc., Hoboken, NJ, USA. doi: 10.1002/9781118482513.ch1

2. **Li, X.**, Wittkowske C., Yao R., Du, Y. (2012). Hydrogel as Stem Cell Niche for In Vivo Applications in Regenerative Medicine. In Biomaterials and Stem Cells in Regenerative Medicine, M. Ramalingam, S. Ramakrishna, and S. Best, eds. (CRC Press.), ISBN: 978-1439879252